

AD-A084 271

MASSACHUSETTS INST OF TECH LEXINGTON LINCOLN LAB
SOLID STATE RESEARCH, 1979:4.(U)
NOV 79 A L MCWHORTER

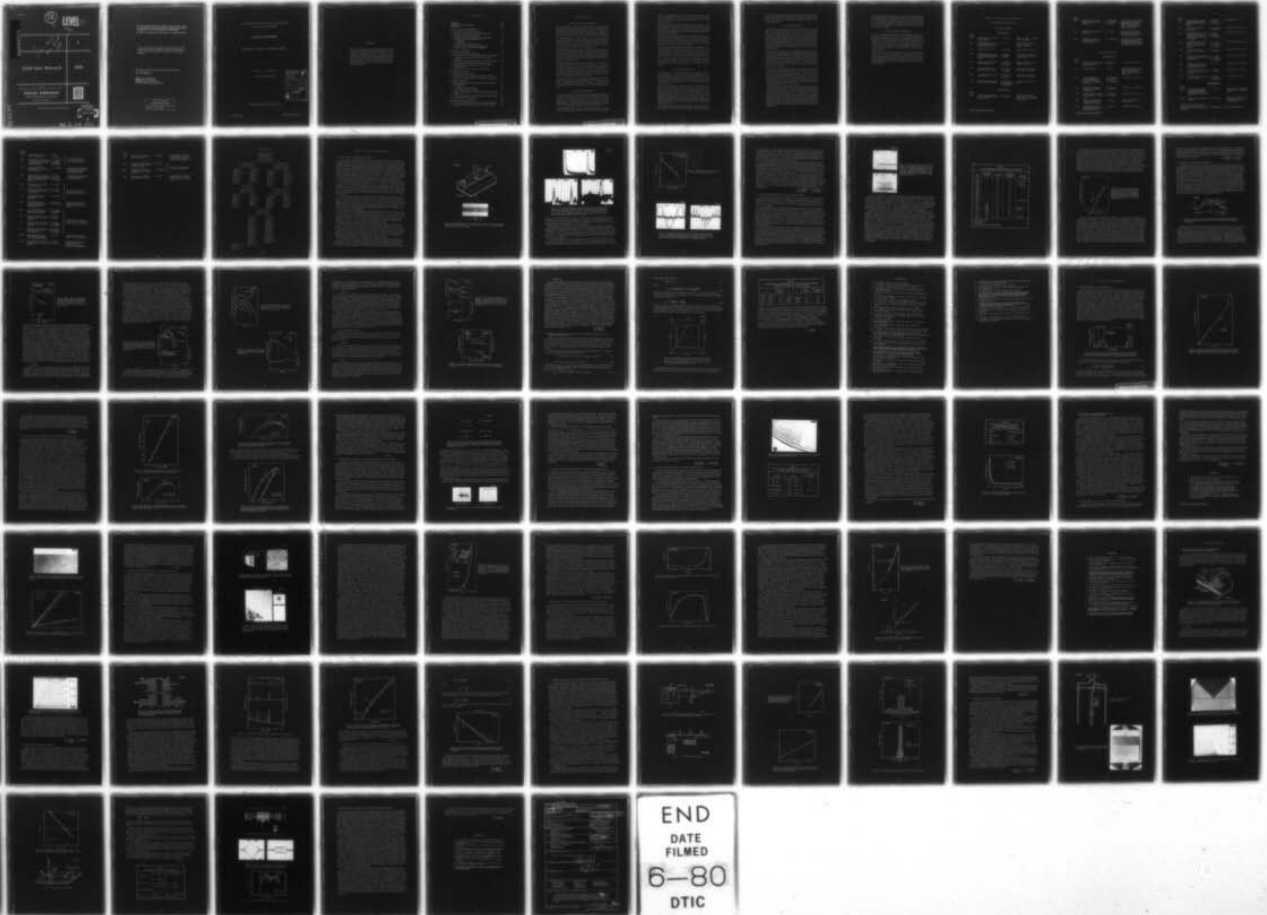
F/6 20/12

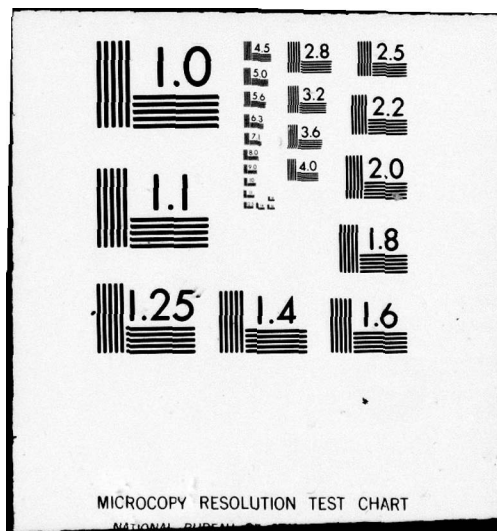
UNCLASSIFIED

ESD-TR-79-274

F19628-80-C-0002
NL

| OF |
AD A
084271





12

LEVEL

A084270

ADA084271

See 1473
on back
page

4

Solid State Research

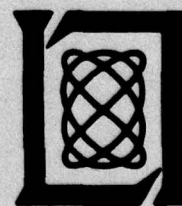
1979

Prepared
under Electronic Systems Division Contract F19628-80-C-0002 by

Lincoln Laboratory

MASSACHUSETTS INSTITUTE OF TECHNOLOGY

LEXINGTON, MASSACHUSETTS



Approved for public release; distribution unlimited.

DTIC
ELECTE
MAY 20 1980

E

80 5 19 221

DTIC FILE COPY

The work reported in this document was performed at Lincoln Laboratory, a center for research operated by Massachusetts Institute of Technology, with the support of the Department of the Air Force under Contract F19628-80-C-0002.

This report may be reproduced to satisfy needs of U.S. Government agencies.

The views and conclusions contained in this document are those of the contractor and should not be interpreted as necessarily representing the official policies, either expressed or implied, of the United States Government.

This technical report has been reviewed and is approved for publication.

FOR THE COMMANDER

Raymond L. Loiselle
Raymond L. Loiselle, Lt. Col., USAF
Chief, ESD Lincoln Laboratory Project Office

Non-Lincoln Recipients

PLEASE DO NOT RETURN

Permission is given to destroy this document
when it is no longer needed.

MASSACHUSETTS INSTITUTE OF TECHNOLOGY
LINCOLN LABORATORY

SOLID STATE RESEARCH

QUARTERLY TECHNICAL SUMMARY REPORT

1 AUGUST - 31 OCTOBER 1979

ISSUED 26 FEBRUARY 1980

Accession For	
NTIS GMA&I	<input checked="checked" type="checkbox"/>
DDC TAB	<input type="checkbox"/>
Unannounced	<input type="checkbox"/>
Justification	
By _____	
Distribution/	
Security Codes	
Dist	Available and/or special
A	

Approved for public release; distribution unlimited.

LEXINGTON

MASSACHUSETTS

ABSTRACT

This report covers in detail the solid state research work of the Solid State Division at Lincoln Laboratory for the period 1 August 1979 through 31 October 1979. The topics covered are Solid State Device Research, Quantum Electronics, Materials Research, Microelectronics, and Analog Device Technology. Funding is primarily provided by the Air Force, with additional support provided by the Army, DARPA, Navy, NASA, NSF, and DOE.

CONTENTS

Abstract	iii
Introduction	vii
Reports on Solid State Research	xi
Organization	xviii
 I. SOLID STATE DEVICE RESEARCH	 1
A. High-Speed InP Optoelectronic Switch	1
B. Self-Sustained Pulsations in GaInAsP Diode Lasers	5
C. GaInAsP/InP Avalanche Photodiodes	9
D. The Effect of Implant Temperature on the Electrical Characteristics of Ion-Implanted InP	11
1. Introduction	11
2. Heavy Ions	11
3. Light and Intermediate-Mass Ions	15
E. Changes in Lattice Parameter and Composition of $\text{Ga}_x\text{In}_{1-x}\text{As}_y\text{P}_{1-y}$: A Vector Formulation	17
 II. QUANTUM ELECTRONICS	 23
A. Remote Sensing of Atmospheric NO	23
B. Limitations on the Frequency-Doubling Efficiency in CdGeAs_2	27
C. Laser-Driven Acoustic and Thermal-Diffusion Modes in Liquids	30
D. Application of Photodissociation Lasers to Chemical Analysis	32
E. Laser-Induced Microscopic Etching of GaAs and InP	33
F. Formation of Ohmic Contacts on p-InP by UV-Laser Photodeposition	37
G. Submillimeter Mixers at Cryogenic Temperatures	37
 III. MATERIALS RESEARCH	 41
A. Diffusion of Zn and Cd in InP	41
B. Scanned Laser Crystallization of Amorphous Ge Films	43
C. Preparation of GaAs Solar Cells by Molecular-Beam Epitaxy	47
 IV. MICROELECTRONICS	 53
A. Fabrication and Microwave Performance of the Permeable Base Transistor	53
1. Theory	53
2. Fabrication and Performance	55
B. Charge-Coupled Devices: Imagers	56
C. Charge-Coupled Devices: CCD Programmable SAW Matched Filter	59
D. Charge-Coupled Devices: Programmable Transversal Filter	61
E. Monolithic GaAs FET Amplifier	65
 V. ANALOG DEVICE TECHNOLOGY	 69
A. A New Cut of Quartz for a Temperature-Compensated RAC	69
B. Wideband LiNbO_3 Elastic Convolver with Parabolic Horns	73

INTRODUCTION

I. SOLID STATE DEVICE RESEARCH

An InP optoelectronic switch, which may be better suited for high-speed analog-signal-processing applications than previously reported Si and GaAs switches, has been fabricated and demonstrated. In experiments using CW mode-locked Nd:YAG lasers, the switches have exhibited an on-state impedance of $\sim 45 \Omega$ for 40 pJ/pulse of incident laser energy. Self-sustained pulsations in light outputs, which are similar to those occurring in AlGaAs, have been observed for several GaInAsP double-heterostructure lasers. The rate of incidence of pulsations in GaInAsP lasers is much lower and their occurrence does not appear to be increased by aging, in marked contrast to AlGaAs lasers.

Low-frequency gains of up to 700 and reduced dark currents have been achieved at 1.15- μm wavelength with a modified version of the inverted-mesa GaInAsP/InP avalanche photodiode structure described previously. In the new structure, carriers are photogenerated in the GaInAsP but are swept into the InP, where they are multiplied in the high-field region of the n-p⁺ junction of the InP.

The effect of implant temperature on the electrical characteristics of InP implanted with various ions has been investigated. For the heavy impurities, Cd and Se, and for the intermediate-mass n-type impurity Si, the highest activation was achieved for implant temperatures $>150^\circ\text{C}$; for the light-impurity Be, the activation was slightly higher for room-temperature than for heated implants; for the intermediate-mass p-type impurity Mg, the effects were dependent on dose.

A vector formulation has been used to obtain the relationship between the change of $\text{Ga}_x\text{In}_{1-x}\text{As}_y\text{P}_{1-y}$ lattice parameter and the change in composition. It is believed that this technique is potentially useful in the development of lattice-matched $\text{Ga}_x\text{In}_{1-x}\text{As}_y\text{P}_{1-y}$ /InP double-heterostructure lasers.

II. QUANTUM ELECTRONICS

Preliminary single-ended remote sensing measurements of atmospheric NO concentrations have been carried out with a differential absorption LIDAR system. Observations were made out to a range of 1.4 km despite high water-vapor absorption interference effects, and average NO concentrations of 100 to 200 ppb were observed using a target at a range of 480 m that was located adjacent to a major traffic roadway.

The doubling efficiency in CdGeAs_2 was found to be limited by a saturation mechanism with a response time faster than 8 nsec, and the

maximum doubling efficiency was found to increase linearly with crystal length for crystals up to 15 mm. A maximum second-harmonic energy of 340 mJ has been observed at 5.3 μm from an 11- \times 13- \times 21-mm AR-coated crystal.

An experimental and theoretical investigation of the coupling of laser radiation to acoustic waves and thermal diffusion modes of liquids has been carried out. Electrostrictive coupling sets the geometry-dependent lower limit on the absorptivities that may be detected using acoustic and thermal lensing techniques.

Photodissociately pumped atomic resonance-line lasers have been shown to be effective sources in quantitative chemical analysis for detection of trace concentrations of metal atoms. Measurements with a modified analytical flame spectrometer have yielded detection limits of 1 and 10 ppb, respectively, for Na and Tl in aqueous solutions.

UV laser-induced etching of GaAs and InP has been demonstrated, using a gas-phase photolysis of halogenated methanes. A resolution of $\sim 1 \mu\text{m}$ has been achieved. A pulsed ArF UV laser has also been used to produce ohmic contacts on p-InP; the process involves a combination of deposition by photolysis of $\text{Cd}(\text{CH}_3)_2$ gas and laser heating of the substrate.

The previously developed Schottky-diode corner-reflector heterodyne mixers have been studied at low temperatures. Total system noise temperature of 3800 K (DSB), or an NEP of 5.3×10^{-20} W/Hz, has been achieved.

III. MATERIALS RESEARCH

The diffusion of Zn and Cd into InP has been investigated in order to make a comparative evaluation of these elements as acceptor diffusants for the fabrication of GaInAsP/InP electrooptical devices. The use of Zn is found to be advantageous because p-n junctions with comparable characteristics can be obtained with lower diffusion temperatures than those required for Cd.

Scanned laser crystallization of amorphous Ge films on fused-silica substrates without surface-relief structures has produced periodic structural features that include regions of well-aligned grains with lateral dimensions up to 2 to 3 \times 100 μm . The theoretical model of laser crystallization reported previously, which is consistent with the observed dependence of spatial period on substrate temperature, suggests the possibility of preparing even larger grained or perhaps single-crystal semiconductor sheets by scanning amorphous films with energy beams of high aspect ratio.

The feasibility of using molecular-beam epitaxy in the fabrication of efficient GaAs solar cells has been demonstrated. Conversion efficiencies

up to 16 percent at AM1 have been obtained for shallow-homojunction $n^+/p/p^+$ cells, without a GaAlAs window, in which the n^+ , p , and p^+ GaAs layers were all grown by molecular-beam epitaxy on single-crystal p^+ GaAs substrates.

IV. MICROELECTRONICS

The permeable base transistor (PBT) has the potential for delivering gain at frequencies above those achieved by any other three-terminal device. The maximum frequency of oscillation for the first PBTs is 17 GHz, with a maximum gain of 13 dB at 4 GHz. A simulation of an optimized version of this PBT predicts a maximum frequency of oscillation of approximately 300 GHz, and a numerical study of the effects of scaling to smaller dimensions predicts a maximum frequency of oscillation approaching 1000 GHz. Fabrication of these devices combines the emerging technologies of x-ray lithography and crystal overgrowth of metal structures.

Work is in progress to improve the low-light-level performance of the CCD imager under development for the GEODSS (Ground Electro-Optical Deep Space Surveillance) Program. Measurements have been made of the dark-current noise as a function of temperature. The thermally generated charge has been reduced below 10 electrons per well for an integration time of 0.25 sec at a temperature of -60°C . This noise level is below the noise-equivalent signal that has been obtained in the output circuitry of these imagers.

A silicon CCD has been integrated with a SAW delay line to produce a CCD programmable analog matched filter. This device has a spurious response which has been identified and modeled. The response arises from the transducer-like detection of the SAW signal by the coupling finger array on the silicon chip. The output resulting from this detection is the convolution of the SAW signal with the impulse response of the coupling finger array and can be avoided by operating the filter well away from the synchronous frequency of the array.

A simple theoretical model has been developed for calculating the variation of threshold voltage both for CCDs with surface-channel inputs and with buried-channel inputs. The model emphasizes the sensitivity of threshold voltage to inhomogeneities in substrate doping or implant doping for the surface-channel and buried-channel cases, respectively. A smaller variation in threshold voltage for surface-channel inputs is predicted for current CCD processing, and experimental results for the two types of devices are consistent with the model, showing a factor-of-6 reduction in variation for surface-channel inputs compared with buried-channel inputs.

A monolithically integrated GaAs FET amplifier has been developed for ultimate integration into a monolithic millimeter-wave transceiver module. The amplifier has demonstrated a gain in excess of 10 dB from 2.0 to 2.6 GHz without matching at the output of the amplifier. With output matching, the amplifier has a noise figure of 4 dB with an associated gain of 11 dB at 2.5 GHz.

V. ANALOG DEVICE TECHNOLOGY

By examining theoretical calculations of the temperature coefficient of delay, it was discovered that a new cut of crystal quartz would have two orthogonal temperature-compensated SAW propagation directions as required for a temperature-stable reflective-array compressor. The existence of this new cut has been experimentally verified and the parameters of the cut — including cut angle, propagation direction, second-order temperature coefficient, and power-flow angle — have been accurately determined.

A wideband (95-MHz-bandwidth) elastic convolver which makes use of a 10- μ sec-long $\Delta V/V$ channel waveguide has been developed. This SAW device uses parabolically tapered horns to spatially compress the acoustic beamwidth and thus increase the efficiency. This scheme, with its relaxed fabrication tolerances, allows larger bandwidths than previously thought possible.

REPORTS ON SOLID STATE RESEARCH

15 August through 15 November 1979

PUBLISHED REPORTS

Journal Articles

JA No.

4806	Rate Equations in Simulated Light Scattering	P. L. Kelley	Phys. Rev. A <u>20</u> , 372 (1979), DDC AD-A076430
4881	Zn-Diffused, Stripe-Geometry, Double-Heterostructure GaInAsP/InP Diode Lasers	J. J. Hsieh	IEEE J. Quantum Electron. <u>QE-15</u> , 694 (1979), DDC AD-A076459
4929	Tunable Infrared Lasers	A. Mooradian	Rep. Prog. Phys. <u>42</u> , 1533 (1979)
4948	Efficient Conversion of Surface Acoustic Waves in Shallow Gratings to Bulk Plate Modes	J. Melngailis H. A. Haus* A. Lattes*	Appl. Phys. Lett. <u>35</u> , 324 (1979), Erratum published in <u>35</u> , 828 (1979)
4963	Spectroscopy and Lasing in $K_5NdLi_2F_{10}$ (KNLF)	A. Lempicki* B. McCollum* S. R. Chinn	IEEE J. Quantum Electron. <u>QE-15</u> , 896 (1979)
4966	Ionization Coefficients of Electrons and Holes in InP	C. A. Armiento S. H. Groves C. E. Hurwitz	Appl. Phys. Lett. <u>35</u> , 333 (1979), DDC AD-A076467
4981	A SAW/CCD Programmable Matched Filter	R. W. Ralston D. L. Smythe E. Stern	Appl. Phys. Lett. <u>35</u> , 388 (1979), DDC AD-A076468
4999	Magnetic Phase Dependence of the Nickel-CO Reaction	R. S. Mehta* M. S. Dresselhaus* G. Dresselhaus* H. J. Zeiger	Phys. Rev. Lett. <u>43</u> , 970 (1979)

Meeting Speeches

MS No.

4894	High-Efficiency GaAs Solar Cells on Single-Crystal GaAs and Ge Substrates	J. C. C. Fan C. O. Bozler	Proc. 1979 Photovoltaic Solar Energy Conf., Berlin, West Germany, 23-26 April 1979, p. 938
------	---	------------------------------	--

* Author not at Lincoln Laboratory.

MS No.

- | | | | |
|------|---|--|---|
| 5004 | High-Speed Electro-Optic Analog-to-Digital (A/D) Converter | F. J. Leonberger
C. E. Woodward
D. L. Spears | Proc. SPIE Vol. 176: <u>Guided Wave Optical System & Devices II</u> (Society of Photo-Optical Instrumentation Engineers, Bellingham, Washington, 1979), pp. 28-35 |
| 5027 | Shallow-Homojunction GaAs Solar Cells | J. C. C. Fan | Proc. Conf. on Solar Cell High Efficiency and Radiation Damage, Cleveland, Ohio, 13-14 June 1979, p. 227 |
| 5050 | Comparison of Surface Acoustic-Wave and Optical Signal Processing | R. C. Williamson | Proc. SPIE Vol. 185: <u>Optical Processing Systems</u> (Society of Photo-Optical Instrumentation Engineers, Bellingham, Washington, 1979), pp. 74-84 |

* * * * *

UNPUBLISHED REPORTS

Journal Articles

JA No.

- | | | | |
|------|--|---|--|
| 4960 | Efficient Infrared ac Kerr Switches Using Simple Cryogenic Liquids | S. R. J. Brueck
H. Kildal | Accepted by Appl. Phys. Lett. |
| 4972 | Liquid-Phase Epitaxy | J. J. Hsieh | Accepted as Chapter in <u>Handbook on Semiconductors</u> , Vol. 3, S. P. Keller, Ed. (IBM, Yorktown Heights, New York, n.d.) |
| 4973 | Tunable Submillimeter Sources Applied to the Excited State Rotational Spectroscopy and Kinetics of CH ₃ F | W. A. Blumberg
H. R. Fetterman
D. D. Peck
P. F. Goldsmith* | Accepted by Appl. Phys. Lett. |
| 4986 | R-Branch Head of the ν_3 Band of CO ₂ at Elevated Temperatures | A. S. Pine
G. Guelachvili* | Accepted by J. Mol. Spectrosc. |
| 4987 | Broadly Tunable CW Operation of Ni:MgF ₂ and Co:MgF ₂ Lasers | P. F. Moulton
A. Mooradian | Accepted by Appl. Phys. Lett. |
| 4989 | A New Cut of Quartz for Temperature-Stable SAW Dispersive Delay Lines | D. E. Oates | Accepted by IEEE Trans. Sonics Ultrason. |
| 5001 | Effects of Narrow Free-Spectral-Range Etalons on Mode-Locked Lasers | S. R. Chinn | Accepted by Opt. Commun. |

* Author not at Lincoln Laboratory.

JA No.

- | | | | |
|------|---|---|--------------------------------|
| 5004 | Atomic Transition Lasers Based on Two-Photon Dissociation of Metal Triiodide Vapors | T. F. Deutsch
D. J. Ehrlich
R. M. Osgood, Jr. | Accepted by Opt. Lett. |
| 5012 | High-Speed InP Optoelectronic Switch | F. J. Leonberger
P. F. Moulton | Accepted by Appl. Phys. Lett. |
| 5014 | Solid-Phase Growth of Large Aligned Grains During Scanned Laser Crystallization of Amorphous Ge Films on Fused Silica | J. C. C. Fan
H. J. Zeiger
R. P. Gale
R. L. Chapman | Accepted by Appl. Phys. Lett. |
| 5017 | Shallow-Homojunction GaAs Solar Cells with High Resistance to 1-MeV Electron Radiation | J. C. C. Fan
R. L. Chapman
C. O. Bozler
P. J. Drevinsky* | Accepted by Appl. Phys. Lett. |
| 5019 | Doppler-Limited Spectroscopy of the $3\nu_3$ Band of SF_6 | A. S. Pine
A. G. Robiette* | Accepted by J. Mol. Spectrosc. |
| 5023 | Efficient Shallow-Homojunction GaAs Solar Cells by Molecular Beam Epitaxy | J. C. C. Fan
A. R. Calawa
R. L. Chapman
G. W. Turner | Accepted by Appl. Phys. Lett. |
| 5026 | Collisional Narrowing of HF Fundamental Band Spectral Lines by Neon and Argon | A. S. Pine | Accepted by J. Mol. Spectrosc. |
| 5027 | Development of a High Repetition Rate Mini-TEA CO_2 Laser | N. Menyuk
P. F. Moulton | Accepted by Rev. Sci. Instr. |
| 5028 | Interband Magneto-Absorption of $\text{In}_{0.53}\text{Ga}_{0.47}\text{As}$ | K. Alavi*
R. L. Aggarwal*
S. H. Groves | Accepted by Phys. Rev. B |

Meeting Speeches†MS No.

- | | | | |
|-------|--|--------------|---|
| 4530A | Precision High Resolution Molecular Spectroscopy Using a Tunable Difference-Frequency Laser Spectrometer | A. S. Pine | Infrared Symp., Philadelphia, Pennsylvania, 17 September 1979 |
| 4542E | Recent Advances in Tunable Lasers | A. Mooradian | Seminar, Bell Laboratories, Holmdel, New Jersey, 5 September 1979 |

* Author not at Lincoln Laboratory.

† Titles of Meeting Speeches are listed for information only. No copies are available for distribution.

MS No.

4612A	High Sensitivity Photodiode Heterodyne Receivers	D. L. Spears	6th Annual Mtg. of Analytics Chemistry & Spectroscopy Societies, Philadelphia, Pennsylvania, 16-21 September 1979
4740A	A High Speed CCD Digitally Programmable Transversal Filter	A. M. Chiang B. E. Burke D. L. Smythe D. J. Silversmith R. W. Mountain	5th Intl. Conf. on CCD Devices, Edinburgh, Scotland, 12-14 September 1979
4779A,B	Some Recent Developments in Laser Crystallization and Laser Annealing at Lincoln Laboratory	J. C. C. Fan	RCA Seminar Series, Princeton, New Jersey, 13 September 1979; Seminar, IBM, Yorktown Heights, New York, 14 September 1979
4802D	Vibrational Kinetics in Cryogenic Liquids and Applications to Nonlinear Optics	S. R. J. Brueck T. F. Deutsch H. Kildal R. M. Osgood, Jr.	Seminar, Memorial University, St. Johns, Newfoundland, Canada, 25 October 1979
4818A	Development and Applications of a High-Speed Electrooptic Analog-to-Digital Converter	F. J. Leonberger	3rd Rocky Mt. Symp. on Microcomputers, Colorado State University, 22 August 1979
5004A	High-Speed Guided-Wave Electrooptic Analog-to-Digital Converter	F. J. Leonberger	Seminar, Dept. of Electrical Engineering and Computer Science, M.I.T., 23 October 1979
5007	Imaging and RCS Measurements of Submillimeter Modeled Tactical Targets	J. Waldman H. R. Fetterman P. E. Duffy T. G. Bryant	25th Tri-Service Radar Symp., USAF Academy, Colorado Springs, 18-20 September 1979
5008	Surface-Acoustic-Wave Devices for Spread-Spectrum Communication	J. H. Cafarella	1979 Intl. Conf. on Solid State Devices, Tokyo, Japan 27-29 August 1979
5029A	Metal-Atom Photodissociation Lasers	D. J. Ehrlich R. M. Osgood, Jr.	Seminar, Bell Telephone Laboratories, Holmdel, New Jersey, 26 September 1979
5029B	Collisional and Radiative Processes in Photodissociatively Produced Atoms	D. J. Ehrlich R. M. Osgood, Jr.	Seminar, Department of Physics, M.I.T., 6 November 1979
5033A	Tunable UV Solid-State Ce:YLF Laser at 325 and 309 nm	D. J. Ehrlich P. F. Moulton R. M. Osgood, Jr.	Topical Mtg. on Excimer Lasers, Charleston, South Carolina, 11-13 September 1979
5077	Two-Wavelength Optical Excitation Studies of XeBr* and Hg ₂ * Excimers	D. J. Ehrlich R. M. Osgood, Jr.	

MS No.			
5039	High Frequency Calculations of IMPATT and TUNNETT Diodes	M. E. Elta	Seventh Biannual Cornell Electrical Engineering Conf., Ithaca, New York, 14-16 August 1979
5145	Permeable Base Transistor	C. O. Bozler G. D. Alley R. A. Murphy D. C. Flanders W. T. Lindley	
5146	Two Dimensional Numerical Simulation of the Permeable Base Transistor	G. D. Alley C. O. Bozler R. A. Murphy W. T. Lindley	
5042	Efficient Frequency Conversion Techniques for CO ₂ Lasers	H. Kildal S. R. J. Brueck N. Menyuk	Electro-Optics/Laser Conf., Anaheim, California, 23-25 October 1979
5047A,B	Third-Order Nonlinear Coefficients of Cryogenic Liquids	S. R. J. Brueck H. Kildal	Gordon Research Conf., Wolfeboro, New Hampshire, 2-6 July 1979; Annual Mtg. of Optical Society of America, Rochester, New York, 8-12 October 1979
5049	Wideband LiNbO ₃ Elastic Convolver with Parabolic Horns	R. A. Becker D. H. Hurlburt	1979 Ultrasonics Symp., New Orleans, Louisiana, 26-28 September 1979
5056	Moving Target Simulation Utilizing a SAW Variable Delay Line Incorporating Quadratic Phase Correction	D. R. Arsenault V. S. Dolat	
5057	Selective Excitation of Bulk Plate Modes	H. A. Haus* A. Lattes* J. Melngailis	
5058	Temperature Effects in Reflective Array Devices and Temperature Compensated RAC	D. E. Oates R. C. Williamson	
5059	Four-Wave Interactions in Acoustoelectric Integrating Correlators	R. W. Ralston E. Stern	
5060	A SAW Accumulating Correlator with CCD Readout	R. W. Ralston D. L. Smythe E. Stern	
5061	A CCD-Programmable SAW Matched Filter	D. L. Smythe R. W. Ralston E. Stern	

* Author not at Lincoln Laboratory.

MS No.

5062	Wide Bandwidth Acousto-electric Convolvers	I. Yao S. A. Reible	1979 Ultrasonics Symp., New Orleans, Louisiana, 26-28 September 1979
5082	A Satellite-Borne SAW Chirp-Transform System for Uplink Demodulation of FSK Communication Signals	R. C. Williamson V. S. Dolat R. R. Rhodes D. M. Boroson	
5053	Wideband SAW Fourier-Transform Processor Design and Applications	R. C. Williamson	IEE Seminar on Case Studies in Advanced Signal Processing, Peebles, Scotland, 18-21 September 1979
5078	Solid-Phase Growth of Large Aligned Grains During Scanned Laser Crystallization of Amorphous Ge Films on Fused Silica	H. J. Zeiger J. C. C. Fan R. P. Gale R. L. Chapman	The Electrochemical Society, Los Angeles, California, 14-19 October 1979
5081	Integrated SAW/CCD Signal Processing Devices	D. L. Smythe	SPIE Seminar on Optical Signal Processing for C ³ I, Boston, 29-30 October 1979
5106	Comparison of Acoustoelectric and Acoustooptic Signal Processing Devices	R. A. Becker S. A. Reible	
5167	Device Requirements for Spread-Spectrum Communication	J. H. Cafarella	
5082A	A Satellite-Borne SAW Spectrum Analyzer for Demodulation of FSK Communication Signals	R. R. Rhodes R. C. Williamson	IEEE Boston Chapter Mtg., MITRE Corp., Bedford, Massachusetts, 24 October 1979
5085	Density Fluctuations Generated in Simple Liquids by Intense Laser Radiation	S. R. J. Brueck L. J. Belanger H. Kildal	1979 Annual Mtg. of Optical Society of America, Rochester, New York, 8-12 October 1979
5100	Remote Sensing of CO Using Frequency Doubled CO ₂ Laser Radiation	D. Killinger N. Menyuk	
5133	Electronic Material Processing Using UV-Laser Photochemistry	D. J. Ehrlich T. F. Deutsch R. M. Osgood	
5134	Excimer Excitation of Lasers Via Bound-Free and Free-Bound Transitions	R. M. Osgood D. J. Ehrlich T. F. Deutsch	
5107B	Crystallographic and Electrical Properties of Silicon Produced by Graphoepitaxy	M. W. Geis	Texas Instruments Colloq., Dallas, 13-14 September 1979
5120,A	X-Ray Lithography - A Review and Assessment of Future Applications	H. I. Smith D. C. Flanders	SEMICON/EAST, Boston, 20 September 1979; 26th Natl. Vacuum Symp., New York, 2-5 October 1979

MS No.

5135	Narrow-Gap Semiconductor Detectors and Lasers	I. Melngailis	Summer School on Narrow-Gap Semiconductor Physics and Applications, Nimes, France, 13-15 September 1979
5155	The Impact of Submicrometer Structures on Future Integrated Electronics	H. I. Smith	EASCON '79, Washington, D.C., 8-11 October 1979
5181	Analog Signal Processing Techniques: SAW and CCD Devices	R. C. Williamson	
5188	Applications of Artificial Microstructures to Optics	H. I. Smith	Seminar, Dept. of Electrical Engineering and Computer Science, M.I.T., 16 October 1979

ORGANIZATION

SOLID STATE DIVISION

A. L. McWhorter, *Head*
I. Melngailis, *Associate Head*
J. F. Goodwin, *Assistant*

P. E. Tannenwald, *Senior Staff*

QUANTUM ELECTRONICS

A. Mooradian, *Leader*
P. L. Kelley, *Associate Leader*

Barch, W. E.	Fetterman, H. R.
Belanger, L. J.	Fleming, M. W.*
Blumberg, W. A. M.	Hancock, R. C.
Brueck, S. R. J.	Kildal, H.
Burke, J. W.	Killinger, D. K.
Bushec, J. F.	Menyuk, N.
Chinn, S. R.	Moulton, P. F.
DeFeo, W. E.	Osgood, R. M., Jr.
Deutsch, T. F.	Parker, C. D.
Ehrlich, D. J.	Peck, D. D.
Feldman, B.	Pine, A. S.

APPLIED PHYSICS

A. G. Foyt, *Leader*
C. E. Hurwitz, *Associate Leader*
T. C. Harman, *Senior Staff*
R. H. Kingston, *Senior Staff*

Armiento, C. A.*	Liau, Z.-L.
Calawa, A. R.	Lind, T. A.
Carter, F. B.	McBride, W. F.
DeMeo, N. L., Jr.	Paladino, A. E.
Diadiuk, V.	Plonko, M. C.
Donnelly, J. P.	Spears, D. L.
Duffy, P. E.	Tsang, D. Z.*
Ferrante, G. A.	Turner, G. W.
Groves, S. H.	Walpole, J. N.
Leonberger, F. J.	

ELECTRONIC MATERIALS

A. J. Strauss, *Leader*
H. J. Zeiger, *Associate Leader*
J. G. Mavroides, *Senior Staff*

Anderson, C. H., Jr.	Hsieh, J. J.
Button, M. J.	Iseler, G. W.
Chapman, R. L.	Kafalas, J. A.
Davis, F. M.	Kolesar, D. F.
Delaney, E. J.	Krohn, L., Jr.
Fahey, R. E.	Mastromattei, E. L.
Fan, J. C. C.	Owens, E. B.
Finn, M. C.	Palm, B. J.
Flutie, R. E.	Pantano, J. V.
Foley, G. H.	Salerno, J. P.*
Gale, R. P.	Tracy, D. M.
Hong, H. Y.-P.	Vohl, P.

ANALOG DEVICE TECHNOLOGY

E. Stern, *Leader*
R. C. Williamson, *Associate Leader*
J. H. Cafarella, *Assistant Leader*

Anderson, A. C.	Hurlburt, D. H.
Arsenault, D. R.	Kernan, W. C.
Baker, R. P.	Lynch, J. T.
Becker, R. A.	Oates, D. E.
Behrman, G. J.	Ralston, R. W.
Brogan, W. T.	Reible, S. A.
DiPerna, M. S.	Slatery, R. L.
Dolat, V. S.	Withers, R. S.
Holtham, J. H.	Yao, I.

MICROELECTRONICS

W. T. Lindley, *Leader*
F. J. Bachner, *Associate Leader*
H. I. Smith, *Assistant Leader*

Alley, G. D.	Lau, C.-L.*
Baker, E. M.	Lincoln, G. A., Jr.
Bozler, C. O.	Lyszcza, T.
Burke, B. E.	Macropoulos, W.
Chiang, A. M.	Mahoney, L. J.
Chu, A.	McClelland, R. W.
Clifton, B. J.	McGonagle, W. H.
Daniels, P. J.	Melngailis, J.†
DeGraff, P. D.	Mountain, R. W.
Durant, G. L.	Murphy, R. A.
Economou, N. P.	Nichols, K. H.
Efremow, N., Jr.	Piacentini, W. J.
Elta, M. E.	Pichler, H. H.
Felton, B. J.	Rathman, D. D.
Flanders, D. C.	Shaver, D. C.‡
Geis, M. W.	Silversmith, D. J.
Gray, R. V.	Smythe, D. L., Jr.
Hansell, G. L.*	Sotomayor-Diaz, O.†
Hawryluk, A. M.*	Wilde, R. E.
Jacobsen, E. H.	

* Research assistant

† Part time

‡ Staff associate

I. SOLID STATE DEVICE RESEARCH

A. HIGH-SPEED InP OPTOELECTRONIC SWITCH

The use of high-speed optoelectronic devices in analog-signal processing is a subject of continuing interest. One device that has received the most interest is the optoelectronic switch, originally demonstrated in both Si (Refs. 1 and 2) and GaAs (Ref. 3). These switches have been used for a number of signal-generation and processing applications.⁴ To date, most of these switches have had a relatively high on-state impedance and/or their laser drivers had low duty cycle. We report here the successful demonstration of the first InP optoelectronic switch. This switch overcomes the problems of previous devices and, hence, may be better suited for some signal-processing functions than either the Si or GaAs switches. The InP switches have typically a 30-psec rise time and have been used to generate a train of 70-psec-wide pulses at 900 MHz and to accurately sample an RF signal at 275 and 550 MS/sec (megasamples per second).

The InP switch is shown schematically in Fig. I-1(a). It consists of a microstrip transmission line formed on Fe-doped semi-insulating InP ($\rho = 2.5 \times 10^8 \Omega\text{-cm}$, $\mu = 2200 \text{ cm}^2/\text{V-sec}$) with a small gap ($\sim 3 \mu\text{m}$) in the top metallization. When the gap is illuminated with an intense laser pulse that is absorbed near the semiconductor surface, the photogenerated electron-hole plasma forms a conducting path across the gap, turning the switch on. For InP, we have found that the switch turns off rapidly at the end of the optical pulse because of the short effective carrier lifetime ($< 50 \text{ psec}$).

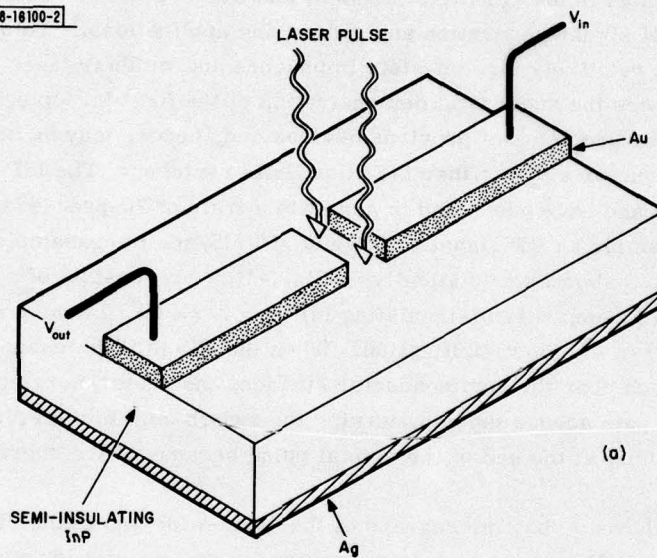
Figure I-1(b) shows a photomicrograph of the $3\text{-}\mu\text{m}$ -wide gap in the InP stripline. For the device shown, the metallization is semitransparent for an $\sim 4\text{-}\mu\text{m}$ -wide region on either side of the gap. This improves the coupling efficiency of the focused laser light, while at the same time maintaining the small gap and thus a relatively low on-state impedance. (The on-state resistance varies as the square of the gap width for a constant optical input power.⁵) For testing, the device was mounted in a package that to a first approximation provided the $50\text{-}\Omega$ impedance necessary for effective high-speed operation.

This InP switch is operationally similar to the referenced Si and GaAs devices but, because of the small-gap design of the InP switches, much less optical power is required. Unlike the Si device, which requires a second laser pulse to turn the switch off, only one laser pulse is needed to operate an InP switch. Also, relative to comparable devices we have fabricated on semi-insulating Cr-doped GaAs, the InP switches have exhibited about an order-of-magnitude lower impedance in the "on" state when illuminated with the same laser power.

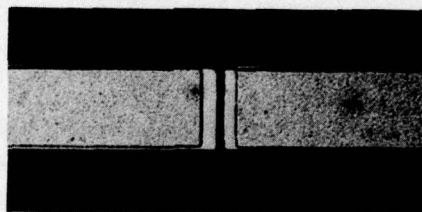
Oscillograms of the sampled response of the switch to three different mode-locked lasers is shown in Fig. I-2(a-c). For these measurements a DC voltage was applied to one side of the stripline and the switch output was monitored on a sampling oscilloscope. Figure I-2(a) shows the switch response to $0.53\text{-}\mu\text{m}$ 150-psec-wide pulses from a frequency-doubled CW mode-locked Nd:YAG laser. The laser pulse repetition rate was 275 MHz. The ability of the switch to fully resolve the laser pulses implies an effective carrier lifetime of $\sim 50 \text{ psec}$. For this $0.53\text{-}\mu\text{m}$ wavelength the switch dynamics are confined to an $\sim 1\text{-}\mu\text{m}$ surface layer.

The response of the InP switch to a mode-locked external-cavity GaAs/GaAlAs diode laser, shown in Fig. I-2(b), was measured to determine the switch performance at a somewhat longer wavelength, and also to demonstrate the potential compactness of the switch and laser driver. The laser was current modulated at 900 MHz and emitted $\sim 1 \text{ mW}$ average power at a wavelength

18-8-18100-2



(a)



(b)

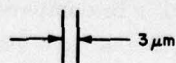


Fig. I-1. (a) Schematic drawing of InP optoelectronic switch; (b) photomicrograph of portion of top metallization of switch stripline showing 4- μm semitransparent regions on either side of 3- μm gap.

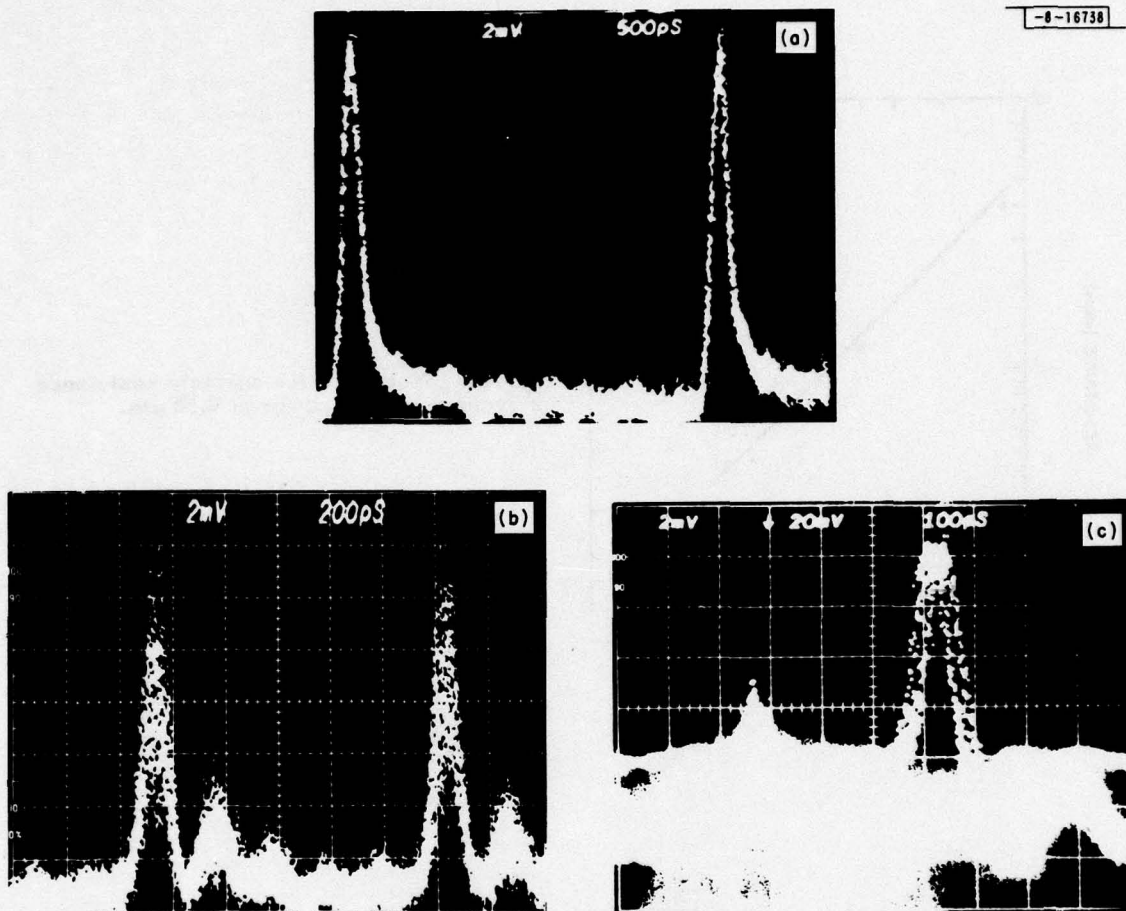


Fig. I-2. Oscilloscope showing response of InP switch to mode-locked laser pulses from (a) frequency-doubled Nd:YAG, (b) GaAs/GaAlAs diode, and (c) frequency-doubled $\text{Nd}_{0.25}\text{La}_{0.75}\text{P}_5\text{O}_{14}$. Upper trace in (c) shows response of an InGaAsP/InP avalanche photodiode to 1.05- μm fundamental pulse from laser and was used to monitor laser performance.

of 0.82 μm . The detected pulses had a FWHM of ~ 70 psec and a rise and fall time each ~ 60 psec. Although there is a small amount of package-related ringing, the response indicates that the switch can be used to generate a pulse train having a bandwidth of at least 6 GHz. For this case the switch dynamics are confined to an ~ 2 - μm surface layer.

The inherent rise time of the switch was deduced from the switch response to a frequency-doubled CW mode-locked $\text{Nd}_{0.25}\text{La}_{0.75}\text{P}_5\text{O}_{14}$ laser, which generated a train of 0.525- μm 10-psec-wide pulses at a 500-MHz rate. From the measured 10- to 90-percent rise time of 40 psec shown in Fig. I-2(c), a sum-of-the-squares approximation was used to estimate an inherent switch rise time of 30 psec. In this experiment the ringing after the pulse was again due to impedance mismatch in the device package.

The switch impedance R for a given laser power can be calculated by comparing the measured peak-height voltage of the DC bias applied to the switch. A measurement of R vs the incident 0.53- μm average power yielded a linear response over the optical power range of 1 to 12 mW

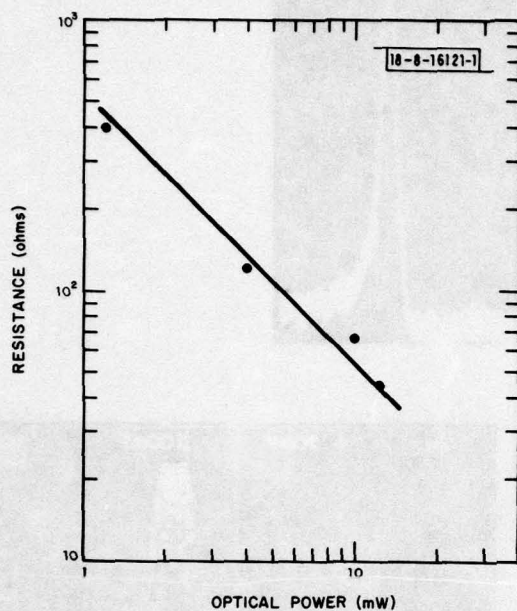


Fig. I-3. Plot of switch on-state resistance vs average optical power at $0.53 \mu\text{m}$.

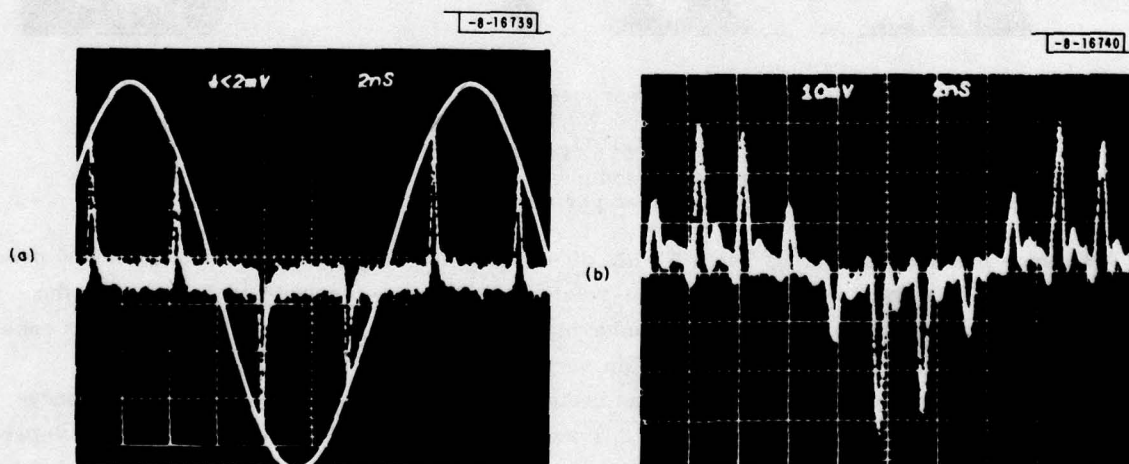


Fig. I-4. Oscilloscopes showing sampling of 68.9-MHz sine wave using InP switch and doubled Nd:YAG laser at (a) 275 MS/sec and (b) 550 MS/sec. In (a), sine wave has been superimposed on sampled signal; in (b), relatively wide pulses and ringing effects are due to output amplifier.

as shown in Fig. I-3. The minimum measured resistance for our devices to date is $\sim 45 \Omega$ at 12 mW (40 pJ/pulse), which should be adequate for a number of signal-processing applications. It should be noted that these impedance values are produced using a relatively low-power CW mode-locked doubled YAG laser. By increasing the CW doubled power or by simultaneously mode-locking and Q-switching the laser, it should be possible to drive the impedance to a negligible value without damaging the semiconductor surface.

As a preliminary demonstration of the application of these InP optoelectronic switches to high-speed analog sampling, a 68.9-MHz sine wave was applied to a switch and sampled using the doubled Nd:YAG laser to excite the switch. Sampling was performed at 275 and 550 MS/sec. An oscillogram of the sampled output at 275 MS/sec is shown in Fig. I-4(a) along with a superposition of the 68.9-MHz test signal. For this case, ~ 1 mW of average optical power was used. The sampling pulses were 150 psec wide [see Fig. I-2(a)]. In the off state, the switch had an impedance corresponding to $R \approx 10^8 \Omega$ and $C \approx 10^{-14}$ F, so that the 70-MHz leakage through the switch was 40 dB down from the sampled signal level. The sampled points are accurate to 98 percent (0.2 dB), indicating the high degree of linearity of the switch. Sampling at 550 MS/sec was achieved by time-multiplexing the laser pulses, and an oscillogram of the sampled signal is shown in Fig. I-4(b). The relatively wide pulse widths and the ringing between pulses evident in the figure are due to the 1.5-GHz bandwidth limitation of the output amplifier used in the measurement.

F. J. Leonberger	S. R. Chinn
P. F. Moulton	M. W. Fleming
G. W. Iseler	F. J. O'Donnell

B. SELF-SUSTAINED PULSATIONS IN GaInAsP DIODE LASERS

We have observed self-sustained pulsations in the light output of CW, room-temperature GaInAsP double-heterostructure lasers. Although this pulsation phenomenon is similar to that reported⁶⁻¹¹ for AlGaAs lasers, the rate of incidence is much lower in the GaInAsP devices. Also, in marked contrast to AlGaAs devices,^{7,11} it does not appear that aging increases the occurrence of self-pulsing.

The lasers for this study were fabricated from wafers prepared by liquid-phase-epitaxial growth of double heterostructures on InP substrates.¹² Tests were made on 156 unaged devices, 10 devices aged at 22°C, and 6 aged at higher temperatures, the aging times ranging from hundreds to many thousands of hours, as will be discussed later. All devices had 13- to 15- μ m-wide stripes defined by proton bombardment,¹³ except for two aged devices with Schottky-barrier-defined (SBD) stripes¹⁴ 7.5 μ m in width. All the lasers operated CW at room temperature with emission wavelengths in the 1.2- to 1.3- μ m region. The two longest-lived devices are still operating with accumulated operating times of 11,100 and 12,600 h, with the former showing no increase in threshold.

Figure I-5(a-b) shows the light output vs time, measured with a Ge photodiode, for two unaged GaInAsP lasers excited with 70-nsec pulses. The upper trace (a) is for a device exhibiting the usual damped relaxation oscillation, while the lower trace (b) is for a device in which the output consists of undamped pulsations. With DC excitation, these pulsations continue indefinitely. The width ($\lesssim 100$ psec in the device shown) and amplitude of the pulsations do not vary significantly with current amplitude, but the repetition rate increases from approximately 100 MHz near threshold up to approximately 1 GHz well above threshold. The pulsations are suppressed for currents near the nonlinear "kinks" in the light-output-vs-current characteristics, as reported⁹ for AlGaAs devices.

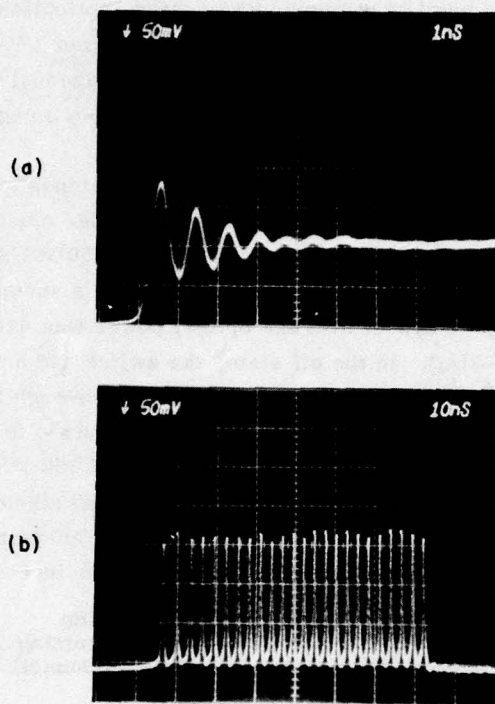


Fig. I-5. Transient response of two GaInAsP lasers for 70-nsec current pulses showing (a) damped relaxation oscillations (1 nsec per div.) and (b) undamped pulsations (10 nsec per div.). Apparent pulsation width is instrument limited here, but is $\lesssim 100$ psec when measured with high-speed detector and sampling oscilloscope.

Of our 156 unaged devices, which were fabricated from 8 different wafers, only 8 exhibited self-sustained pulsations, for an average rate of incidence of 5 percent. Six of these came from a single wafer (wafer 4-4) that provided 58 of the devices tested. For the other 7 wafers, only 2 out of 98 devices exhibited pulsations. For comparison, in a study of proton-bombarded AlGaAs lasers, Paoli⁷ reported initial rates of incidence ranging from 5 to 30 percent for 4 wafers, with an average rate of 20 percent. More recently, Hartman *et al.*¹¹ reported an initial rate of incidence of pulsations of 38 percent for 47 strip-buried-heterostructure AlGaAs lasers.

Experiments on AlGaAs lasers have shown that the occurrence of sustained pulsations is strongly increased by aging. Thus, Paoli⁷ found that an average of 62 percent (48 to 70 percent, depending on the wafer) of 103 initially nonpulsing devices had developed some degree of sustained pulsations after CW operation at 70°C for 50 to 60 h (equivalent to operation at 22°C for 2300 to 4800 h, if the activation energy is assumed to be 0.7 to 0.8 eV). Moreover, Hartman *et al.*¹¹ found that 5 out of 10 lasers which did not initially exhibit pulsations did so after only 15 h of CW operation at 35°C (equivalent to 55 h at 22°C). To investigate the effect of aging on self-sustaining pulsations in GaInAsP lasers, we tested 16 devices that had been subjected to the aging conditions summarized in Table I-1. All but one had been operated CW for more than 2000 h at 22°C (or an equivalent time at higher temperature, assuming an activation energy of 0.7 eV) with approximately 3 mW of output power per facet. The other device had been baked at 90°C without current flow until degradation was evident after 482 h. Four devices are from wafer 4-4, which had the highest initial incidence of lasers with sustained pulsations. All devices were aged in air without facet coatings and, except for the devices from wafer 4-4, operating current densities were quite high.

TABLE I-1
AGING CONDITIONS FOR LASERS TESTED FOR PULSATIONS

Time (h)	Equivalent [†] Time at 22°C (h)	Temperature (°C)	Operating Current Density (kA/cm ²)	Comments (see text)
12,600 [‡]	—	22	11.5	7.5-μm SBD
11,100 [§]	—	22	3.2	Wafer 4-4
11,000	—	22	7.1	7.5-μm SBD
7,800	—	22	5.5	—
5,800	—	22	8.1	—
3,400 [‡]	—	22	7.8	—
3,400 [‡]	—	22	6.4	—
3,000	—	22	7.0	—
2,400	—	22	6.9	Weak pulsations
2,100	—	22	12.3	—
882	4,400	40	9.1	—
1,200	13,000	50	4.2	Wafer 4-4
1,000 [§]	11,000	50	4.0	Wafer 4-4
212	2,300	50	8.1	—
184	2,000	50	8.0	—
482	—	90	0	Wafer 4-4

[†] Assuming $E_g = 0.7$ eV.

[‡] Still operating.

[§] Still operating with no change in threshold.

After aging, only one device (from wafer 8-18, operated at 22°C for 2,400 h) showed pulsations, and these were weak compared with those illustrated in Fig. I-5(b). Even in this case it is not certain that the pulsations were induced by aging, since initial screening for sustained pulsations was not done at the time the device was put on test. For the device still operating unchanged at 50°C, we found no change in the relaxation oscillation transient at 22°C for the same pulsed current when we compared photographs taken before and after aging. Although such a comparison could not be made for the other devices since photographs were not taken before aging, we found no cases of unusually low damping of the oscillations after aging, which might indicate the initial stages of a shift toward undamped pulsations. Overall, the results of the aging experiments strongly suggest that sustained pulsations will not occur to a significant degree in the first 10,000 h or so of room-temperature operation of initially nonpulsing GaInAsP lasers.

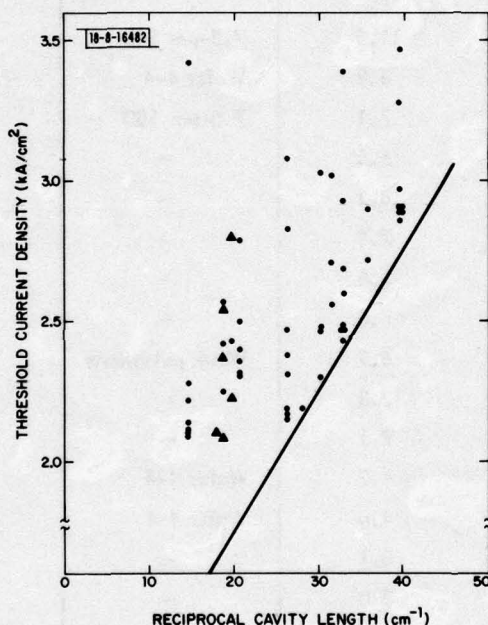


Fig. I-6. Threshold current density vs reciprocal cavity length for 58 unaged lasers from wafer 4-4. Circled points correspond to devices exhibiting sustained pulsations. Solid line represents dependence suggested by overall trend of data which would exist for defect-free devices.

In Fig. I-6 we have plotted threshold current density vs reciprocal device length for all 58 unaged devices from wafer 4-4. For ideal devices with no localized optical or electrical defects, the dependence of threshold on reciprocal length should be essentially linear with a positive slope. In the presence of random localized defects, the observed thresholds should be scattered and lie above the ideal, minimum values. This is apparently the case for the data of Fig. I-6, where the solid line has been drawn to represent the ideal, defect-free relationship suggested by the overall trend of the data. The circled data points represent the 6 devices with sustained pulsations. Since all 6 are approximately 545 μm long, it is likely that they are all from the same cleaved bar. (The wafer is first cleaved into bars before individual devices are cut.) Since several devices of comparable length to these 6 devices (as well as several slightly shorter and several somewhat longer) do not exhibit sustained pulsations, length does not appear to be an important factor. Moreover, since the threshold current densities of the devices with sustained pulsations

vary from the lowest observed to among the highest, defects contributing to increased threshold are not necessarily related to the phenomenon. Instead, it appears that defects peculiar to one particular cleaved bar, and hence one region of the wafer, are responsible for the sustained pulsations in this case. Such localized defects could result from irregularities in the growth process or fabrication procedures.

J. N. Walpole J. J. Hsieh
T. A. Lind A. G. Foyt

C. GaInAsP/InP AVALANCHE PHOTODIODES

Substantial increase in avalanche gain and reduction of dark current have been achieved in a modified version of the inverted-mesa GaInAsP/InP avalanche photodiode structure described previously.^{15,16} The structure, shown in Fig. I-7, differs from the earlier one in that a 1- μm layer of n-InP is interposed between the p⁺-InP substrate and the n-GaInAsP layer. (The n⁺-InP top layer is also omitted for simplicity, with little expected effect other than some increase in contact resistance and a possible decrease in quantum efficiency due to surface recombination of photogenerated carriers.) The p-n junction is now located in the InP, but with sufficient reverse bias the depletion region extends into the GaInAsP. Hence, incident light of appropriate wavelength ($\lambda \lesssim 1.3 \mu\text{m}$) is absorbed in the GaInAsP, generating holes that are swept into the InP, where they are multiplied in the high-field region of the junction. This separation of the generation and multiplication regions and the attendant improvement in avalanche detector characteristics of GaInAsP/InP photodiodes were first demonstrated by Nishida *et al.*^{17,18} in a diffused structure. In the devices described here, the diffusion step is not required and edge breakdown is clearly eliminated by use of the inverted-mesa structure.^{15,16}

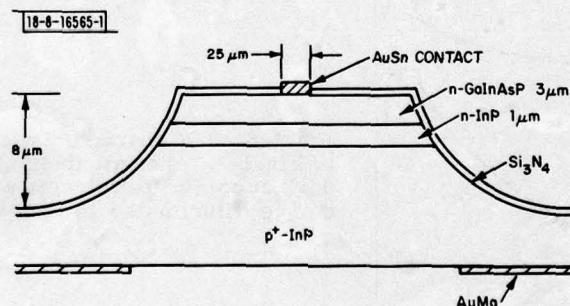


Fig. I-7. Schematic cross section of GaInAsP/InP inverted-mesa avalanche photodiode with p-n junction located in InP. Device diameters ranged from 2.5 to 6 mils.

Details of the structure used in these initial studies are given in Fig. I-7. Layers of n-type InP and GaInAsP with $n \approx 1 \times 10^{16} \text{ cm}^{-3}$ are grown onto a p⁺-InP substrate by liquid-phase epitaxy. The InP and GaInAsP layers have thicknesses of 1 and 3 μm , respectively. The approximate composition of the quaternary alloy was $\text{Ga}_{0.23}\text{In}_{0.77}\text{As}_{0.52}\text{P}_{0.48}$, with the long-wavelength photoresponse cutoff measured to be about 1.25 μm . Mesas, 8 μm in height, were etched using a mask that yields devices of 6 different diameters, ranging from 2.5 mils (64 μm) to 6 mils (152 μm). Plated AuSn top contacts, 1 mil in diameter, and an evaporated AuMg bottom contact were alloyed by heating the sample to $\sim 400^\circ\text{C}$ for 10 sec. The AuMg contact did not cover

the entire back surface, thus leaving windows through which to shine light from the back side. A layer of Si_3N_4 , approximately 900 Å thick, was used as surface passivation and antireflection coating.

Best results were obtained on the smaller devices (2.5 to 3.5 mils in diameter). I-V characteristics, a typical one of which is shown in Fig. I-8, gave dark currents as low as 1.5 nA at $1/2 V_b$. (V_b , the breakdown voltage, was approximately 100 V in these devices.) Scanning the devices with 1.15- μm laser light, incident from both the front and back sides, yielded uniform photoresponse. Taking into account approximately the variation in collection efficiency with bias, maximum low-frequency gains of up to ~ 700 were observed with ~ 2 nA of primary photocurrent induced by light incident on the back side; lower gains (~ 200) were measured when light of the same intensity was incident from the front. The reason for the difference is not presently understood. In both cases the light is predominantly absorbed in the n-GaInAsP layer and, hence, the carriers initiating the multiplication are primarily holes. Although changes in collection efficiency with bias are much more pronounced with light incident from the front, our initial calculations indicate that any reasonable estimate of this variation does not account for the apparent gain difference. The maximum gain from both front and back was observed to decrease with increasing primary photocurrent over the range from 2 nA to 1 μA (at which the maximum gain measured was ~ 10 , from both front and back).

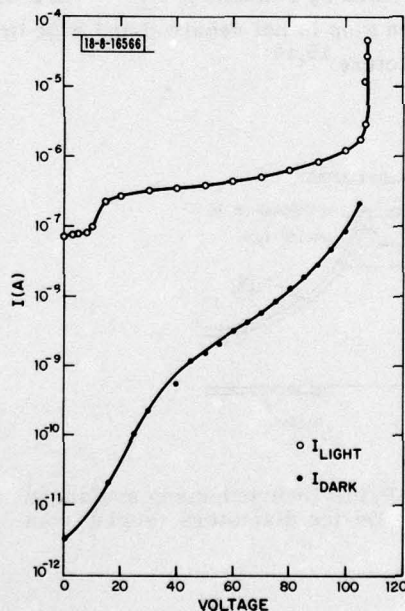


Fig. I-8. I-V characteristics of structure of Fig. I-7. Closed circles correspond to dark current; open circles were taken with device illuminated by microscope lamp.

No photoresponse was observed at biases below 12 V. This value of bias also corresponds to that at which a current step was observed in the I-V characteristics of the devices under illumination with a microscope lamp (see Fig. I-8), and at which a small discontinuity occurred in the concentration profile obtained from C-V measurements. These observations are all consistent with the idea that at this value of applied bias the depletion region punches through the InP/GaInAsP heterojunction. The photogenerated holes, which at low bias had been confined to

the GaInAsP by the valence-band barrier of the heterojunction, are now swept by the junction field over the barrier into the InP where they are collected.^{17,18}

With the 1.06- μm , 200-psec-pulse excitation from a mode-locked Nd:YAG laser incident from the front of a typical device, response times of ~ 400 psec (FWHM) were measured. This relatively long response time is probably due to the fact that, with light incident from the front, carriers generated at the surface must diffuse through a large portion of the quaternary layer before reaching the field region. No such diffusion takes place with light incident from the back, so shorter response times are likely to be obtained.

Work is presently under way to further characterize the devices with respect to spectral response, noise characteristics, and frequency response, as well as to optimize device parameters.

V. Diadiuk
S. H. Groves
C. E. Hurwitz

D. THE EFFECT OF IMPLANT TEMPERATURE ON THE ELECTRICAL CHARACTERISTICS OF ION-IMPLANTED InP

1. Introduction

The expanding interest in InP devices during the last few years has led, in turn, to an increased amount of activity in developing ion-implantation technology in this material.¹⁹⁻³⁰ Many of the results previously published^{19,21,24,29} indicated that the temperature of the InP during implantation can have a pronounced influence on the characteristics of the resulting implanted layers. In this section new and more detailed results are presented of a study of these temperature effects on the electrical characteristics of InP layers implanted with a variety of donor and acceptor ions.

The InP used in these experiments consisted of polished and etched samples cut from (111)-oriented high-resistivity ($\rho \geq 10^7 \Omega\text{-}\mu\text{m}$) Fe-doped crystals. During implantation, the samples were tilted with respect to the ion beam to minimize channeling. Following implantation, they were annealed at 750°C for 10 to 15 min. using a PSG (phosphosilicate glass) encapsulation technique described previously.^{19,24} Contacts were then applied and cloverleaf patterns etched in the implanted layers to facilitate Hall measurements of the van der Pauw type.³¹ Control samples of Fe-doped InP used in these experiments – which were not implanted but which were temperature-cycled in the ion-implantation system, encapsulated, and annealed at temperatures up to 800°C – showed no indication of the formation of surface conducting layers.

2. Heavy Ions

Previous results indicated that higher sheet carrier concentrations are obtained by implanting heavy ions into InP at 200°C rather than at room temperature.¹⁹ Figure I-9 shows the sheet carrier concentration vs implant temperature of InP samples implanted with $1 \times 10^{14} \text{ cm}^{-2}$ of a heavy n-type impurity (Se), a heavy p-type impurity (Cd), and a heavy inert impurity (Kr). All the ions were implanted at an energy of 400 keV.

a. Damage Effects

The Kr implants were performed in an attempt to determine the electrical behavior of residual damage in InP implanted with heavy ions. Assuming that the Kr itself is not electrically active, the data in Fig. I-9 show that residual ion-implantation damage in InP is n-type.^{19,32}

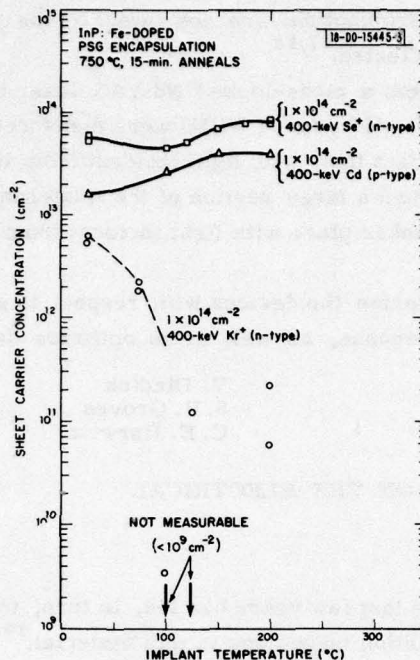


Fig.I-9. Sheet carrier concentration vs implant temperature for InP samples implanted at 400 keV with $1 \times 10^{14} \text{ cm}^{-2}$ of heavy ions, Se^+ (an n-type impurity), Cd^+ (a p-type impurity), and Kr^+ (a neutral species).

For room-temperature Kr implants, the sheet carrier concentration consistently falls in the range of $(5 \text{ to } 6) \times 10^{12} \text{ cm}^{-2}$ with sheet mobilities of several hundred $\text{cm}^2/\text{V-sec}$. The measured sheet carrier concentration due to residual damage decreases with increasing implant temperature. For samples implanted at temperatures of 100°C and above, it is much lower than for those implanted at room temperature, ranging from not measurable ($< 10^9 \text{ cm}^{-2}$) to about $2 \times 10^{11} \text{ cm}^{-2}$. There is, however, considerable scatter in the data in the 100° to 200°C implant temperature range, and only data points indicating the range of sheet concentration have been included in Fig. I-9. The ambiguity of the results above 100°C indicates that other mechanisms contributing to the observed sheet carrier concentrations are coming into play. One possibility is the damage-enhanced outdiffusion of P and/or compensating impurities or defects occurring during the heated implant. Nevertheless, the data clearly indicate that implant temperatures of 100°C or above are necessary to minimize the n-type behavior due to the residual damage induced by the implantation of heavy ions in InP. It is important to note further that, even for heated implants, the post-implantation anneal is necessary to minimize this n-type behavior associated with implant damage. For example, unannealed samples implanted at 200°C with $1 \times 10^{14} \text{ cm}^{-2}$ of Kr had sheet concentrations in the range of $(2 \text{ to } 3) \times 10^{12} \text{ cm}^{-2}$ and very low sheet mobilities of $(5 \text{ to } 10) \text{ cm}^2/\text{V-sec}$. Similar samples annealed at 750°C for 15 min. had sheet concentrations of $(6 \text{ to } 20) \times 10^{10} \text{ cm}^{-2}$ and much higher mobilities of $(420 \text{ to } 1100) \text{ cm}^2/\text{V-sec}$.

b. Selenium

As shown in Fig. I-9, samples implanted with the donor ion Se at temperatures above 150°C had higher sheet carrier concentrations than those implanted at room temperature. The sheet mobilities are also higher for samples implanted above 150°C ($1700 \text{ to } 1800 \text{ cm}^2/\text{V-sec}$) than for samples implanted at room temperature ($1150 \text{ to } 1450 \text{ cm}^2/\text{V-sec}$). The small decrease in the measured sheet carrier concentration for samples implanted between room temperature and

100°C is believed to be due to a decrease in the number of donors resulting from the above-mentioned residual n-type implant damage. Above 100°C, the sheet carrier concentration increases with implant temperature until it saturates at $(7.8 \text{ to } 8.0) \times 10^{13} \text{ cm}^{-2}$. It should also be noted that there is much less scatter in the data obtained on samples implanted at 200°C than on those implanted at room temperature. For ten samples implanted at 200°C, all had sheet carrier concentrations in the range $(7.8 \text{ to } 8.0) \times 10^{13} \text{ cm}^{-2}$ and all but one (which had a sheet mobility of $1900 \text{ cm}^2/\text{V-sec}$) had sheet mobilities in the range $(1700 \text{ to } 1800) \text{ cm}^2/\text{V-sec}$.

To examine the effects of implant temperature on the depth profile of the electrically active implanted Se, a series of Hall measurements combined with step etching³³ was performed on selected samples. Figure I-10 shows the carrier concentrations and mobilities vs depth of two InP samples, one implanted at 200°C and one at room temperature with $1 \times 10^{14} \text{ cm}^{-2}$ 400-keV Se. Also shown is the calculated Se profile obtained using the Johnson and Gibbons formulation³⁴ of LSS theory.³⁵ The sample implanted at 200°C has a peak concentration of about $3.8 \times 10^{18} \text{ cm}^{-3}$ at a depth of 1650 Å. This depth is close to the theoretical range of LSS theory. The distribution of the carrier concentration, however, is wider than expected from LSS theory, indicating that some diffusion of the Se is taking place either during the implant or anneal. For the sample implanted at room temperature, the Se near the surface is either not electrically active or is compensated. The mobility of the sample implanted at room temperature is lower than that of the sample implanted at 200°C at all depths.

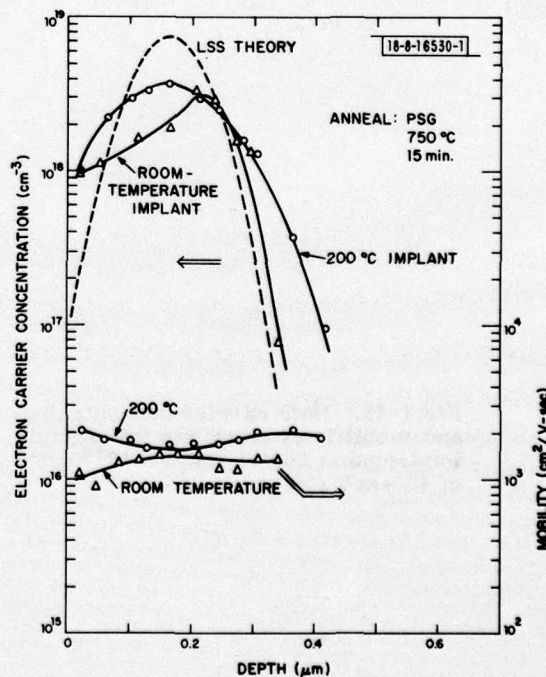


Fig. I-10. Electron carrier concentration and mobility vs depth measured in InP implanted at room temperature and 200°C with $1 \times 10^{14} \text{ cm}^{-2}$ of 400-keV Se ions. Also shown is Se distribution expected from LSS range theory.

Samples implanted with doses of 400-keV Se from 1×10^{13} to $1 \times 10^{15} \text{ cm}^{-2}$ showed similar sheet carrier concentration vs implant temperature behavior as the samples implanted with $1 \times 10^{14} \text{ cm}^{-2}$. Figure I-11 shows the carrier concentration vs depth for samples implanted at 200°C with 3×10^{13} , 1×10^{14} , and $1 \times 10^{15} \text{ cm}^{-2}$ of 400-keV Se. All the samples had peak carrier

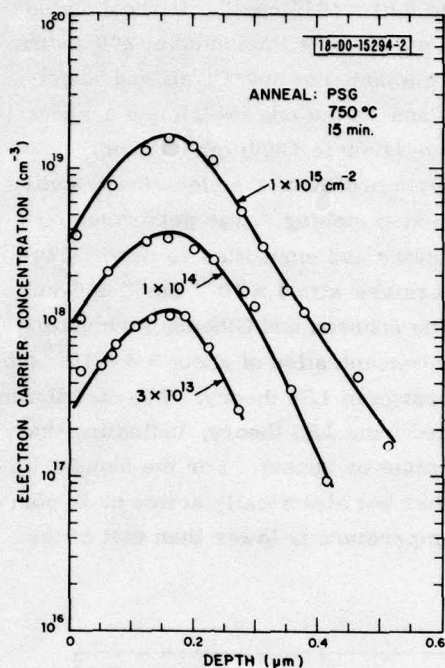
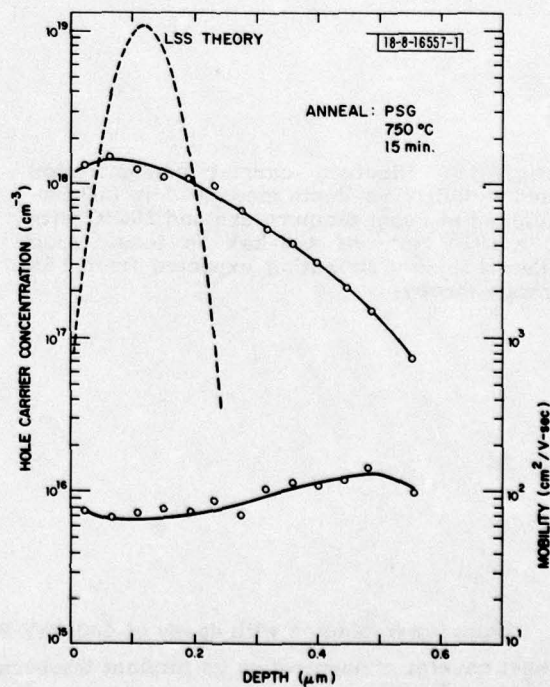


Fig. I-11. Electron carrier concentration vs depth for InP samples implanted at 200°C with 3×10^{13} , 1×10^{14} , and $1 \times 10^{15} \text{ cm}^{-2}$ of 400-keV Se.

Fig. I-12. Hole carrier concentration and mobility vs depth for InP sample implanted at 200°C with $1 \times 10^{14} \text{ cm}^{-2}$ of 400-keV Cd.



concentrations at the depth expected from LSS theory, but the distributions were wider than predicted. The sample implanted with $1 \times 10^{15} \text{ cm}^{-2}$ had a peak carrier concentration of $1.6 \times 10^{19} \text{ cm}^{-3}$, indicating that electron concentrations greater than 10^{19} cm^{-3} can be fairly easily achieved in InP with implanted Se.

c. Cadmium

For the heavy p-type impurity (Cd), Fig. I-9 shows that the sheet carrier concentration increases with implant temperature and that implant temperatures of 150°C or above are required for highest activation. The sheet mobility is not very dependent on implant temperature. For the $1 \times 10^{14} \text{ cm}^{-2}$ implant, the sheet hole concentrations even for implant temperatures above 150°C are only $4.0 \times 10^{13} \text{ cm}^{-2}$, corresponding to an effective activation of 40 percent, which is low compared with the 78- to 80-percent activation achievable with the n-type impurity Se. The highest sheet hole concentration obtained with Cd was $9 \times 10^{13} \text{ cm}^{-2}$ (with a mobility of $100 \text{ cm}^2/\text{V-sec}$) on a sample implanted 150°C with a dose of $1 \times 10^{15} \text{ cm}^{-2}$.

As has been observed in GaAs (Refs. 36 and 37), there appears to be substantial diffusion of the implanted Cd. This is illustrated in Fig. I-12, which shows the hole carrier concentration and mobility vs depth for a sample implanted at 200°C with $1 \times 10^{14} \text{ cm}^{-2}$ of 400-keV Cd. Also shown is the implanted Cd profile expected from LSS range theory. The measured peak hole concentration is only $1.5 \times 10^{18} \text{ cm}^{-3}$, and the profile is much wider than expected. Although more work is required in this area to completely determine the effects of dose and implant temperature on diffusion, it appears that it will be more difficult to obtain high hole concentrations in InP by ion implantation than is the case in GaAs (Refs. 39 and 36).

3. Light and Intermediate-Mass Ions

Results obtained on the implantation of lighter ions are shown in Fig. I-13, where the sheet carrier concentration and mobility of samples implanted with $1 \times 10^{14} \text{ cm}^{-2}$ of a light ion, 400-keV Be, and two ions of intermediate mass, 400-keV Si and 150-keV Mg, are plotted vs implant temperature.

a. Beryllium

The sheet hole concentrations obtained for samples implanted with Be at room temperature are slightly higher than those obtained on samples implanted at 200°C . More detailed results on Be-implanted InP (which can be found in Ref. 24) show that room-temperature Be implants are generally equal to, and in some cases superior to (because of less indiffusion of the implanted Be), heated implants. The maximum activation obtained for this light p-type impurity, approximately 60 percent, is also less than that obtained with n-type impurities.

b. Silicon

For the intermediate-mass n-type impurity (Si), higher sheet carrier concentrations and mobilities were generally obtained on samples implanted at elevated temperatures. As indicated in Fig. I-13, the results obtained on samples implanted at temperatures of 150°C and above have also been found to be much more reproducible than those obtained on samples implanted at room temperature. For samples implanted at 200°C with $1 \times 10^{14} \text{ cm}^{-2}$ of 400-keV Si, the measured sheet carrier concentrations and mobilities all fell in the ranges $(7.6 \text{ to } 7.8) \times 10^{13} \text{ cm}^{-2}$ and $(1800 \text{ to } 2000) \text{ cm}^2/\text{V-sec}$, respectively.

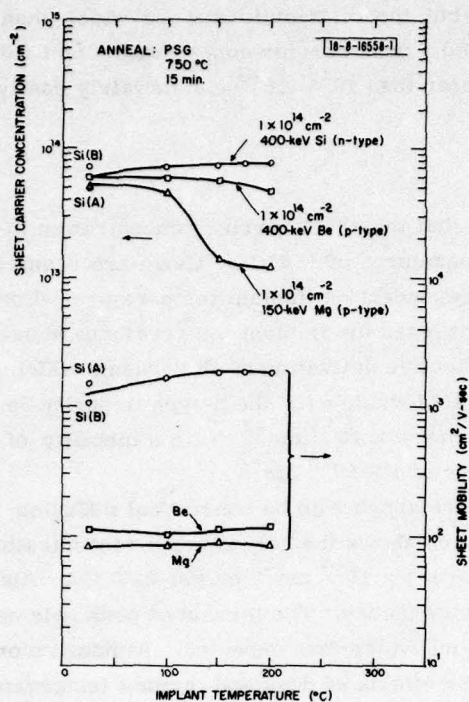


Fig. I-13. Sheet carrier concentration and mobility vs implant temperature for InP samples implanted with $1 \times 10^{14} \text{ cm}^{-2}$ of 400-keV Be (a light ion), and $1 \times 10^{14} \text{ cm}^{-2}$ of 400-keV Si and 150-keV Mg (ions of intermediate mass).

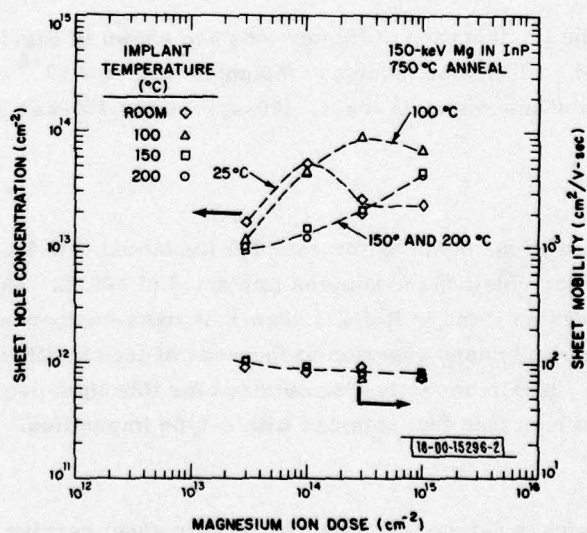


Fig. I-14. Sheet hole concentration and mobility vs dose for InP samples implanted at room temperature, 100 °C, 150 °C, and 200 °C with 150-keV Mg ions.

c. Magnesium

For samples implanted with Mg at 150 keV and a dose of $1 \times 10^{14} \text{ cm}^{-2}$, higher sheet hole concentrations were obtained on those implanted at room temperature than on those implanted at higher temperatures. In contrast to the other ions studied, however, the results obtained with Mg implanted at room temperature exhibit a pronounced anomalous dose dependence. This can be seen in Fig. I-14, where the sheet hole concentration and mobility of InP samples implanted with 150-keV Mg at room temperature, 100°C, 150°C, and 200°C are plotted vs dose. For room-temperature implants, the sheet hole concentration increases with implant dose up to $1 \times 10^{14} \text{ cm}^{-2}$. For doses above this value, the sheet hole concentration actually falls quite drastically. For 100°C implants, a less-abrupt maximum is observed at doses of $3 \times 10^{14} \text{ cm}^{-2}$. For implants performed with the InP at temperatures of 150°C or above, the sheet hole concentration increases monotonically with dose. The sheet mobility does not seem to depend critically on implant temperature. The highest sheet hole concentration obtained by implanting 150-keV Mg was $9 \times 10^{13} \text{ cm}^{-2}$, with a corresponding sheet mobility of $80 \text{ cm}^2/\text{V-sec}$ — results which were obtained on a sample implanted at 100°C with $3 \times 10^{14} \text{ cm}^{-2}$. Preliminary profile measurements on samples implanted at room temperature with $1 \times 10^{14} \text{ cm}^{-2}$ of Mg indicate that significant diffusion of the implanted Mg occurs. Although a great deal more work is needed to sort out the data in Fig. I-14, a plausible explanation may be based on a combination of (1) a damage-enhanced diffusion effect which decreases with increasing implant temperature, and (2) a critical dose, the value of which increases with implant temperature, above which significant residual n-type damage remains after annealing. This critical dose, which could be that at which amorphization occurs, becomes extremely high and, for all practical purposes, infinite³⁷ for implant temperatures greater than or equal to 150°C.

J. P. Donnelly
C. E. Hurwitz
G. A. Ferrante

E. CHANGES IN LATTICE PARAMETER AND COMPOSITION OF $\text{Ga}_x\text{In}_{1-x}\text{As}_y\text{P}_{1-y}$: A VECTOR FORMULATION

There have been extensive studies on the relation between the $\text{Ga}_x\text{In}_{1-x}\text{As}_y\text{P}_{1-y}$ lattice parameter and its composition.³⁹⁻⁴¹ In this work change of the lattice parameter is expressed as the scalar product of a vector \vec{A} and the "composition displacement vector," $\vec{\Delta} \equiv \vec{e}_x \Delta x + \vec{e}_y \Delta y$, where \vec{e}_x and \vec{e}_y are unit vectors in the x- and y-directions, respectively. Based on Vegard's law, the vector \vec{A} is constant to within better than 3 percent over a wide composition range of interest.

It has been reported that the experimentally measured lattice parameter a , as a function of x and y , is in good agreement with Vegard's law,^{39,41} i.e.,

$$a = a_{\text{InP}}(1-x)(1-y) + a_{\text{InAs}}(1-x)y + a_{\text{GaAs}}xy + a_{\text{GaP}}x(1-y) \quad (\text{I-1a})$$

or

$$a(\text{\AA}) = 5.8696 - 0.4184x + 0.1894y + 0.0130xy \quad (\text{I-1b})$$

by substituting values of a_{InP} , a_{InAs} , a_{GaAs} , and a_{GaP} into Eq. (I-1a). For small changes in x and y , the corresponding change in a can be obtained by taking the differential of Eq. (I-1a), which, after some rearranging, becomes

$$\Delta a(\text{\AA}) = (-0.4184 + 0.0130y)\Delta x + (0.1894 + 0.0130x)\Delta y \quad (\text{I-2})$$

This equation can be written as

$$\frac{\Delta a}{a} = \vec{A} \cdot \vec{\Delta} \quad (I-3)$$

where

$$\vec{A} \equiv \vec{e}_x \frac{-0.4184 + 0.0130y}{5.8696} + \vec{e}_y \frac{0.1894 + 0.0130x}{5.8696} \quad (I-4)$$

[Since lattice matching to InP is of primary interest, $a \equiv a_{\text{InP}} = 5.8696 \text{ \AA}$ has been used in Eq. (I-4).] The vector \vec{A} , which is a function of x and y , can be approximated by a constant vector \vec{A}_0 which is defined as

$$\vec{A}_0 \equiv \vec{e}_x \frac{-0.4184}{5.8696} + \vec{e}_y \frac{0.1894}{5.8696} \quad (I-5)$$

Since the x and y values of general interest are $0 \leq x \leq 0.5$ and $0 \leq y \leq 1.0$, respectively, the deviations of \vec{A} from \vec{A}_0 are smaller than ~ 3 percent by comparing Eqs. (I-4) and (I-5). Another way of obtaining Eq. (I-3) and $\vec{A} \approx \vec{A}_0$ is illustrated in Fig. I-15, where the change of lattice parameter in the x -direction is almost independent of y , and vice versa.

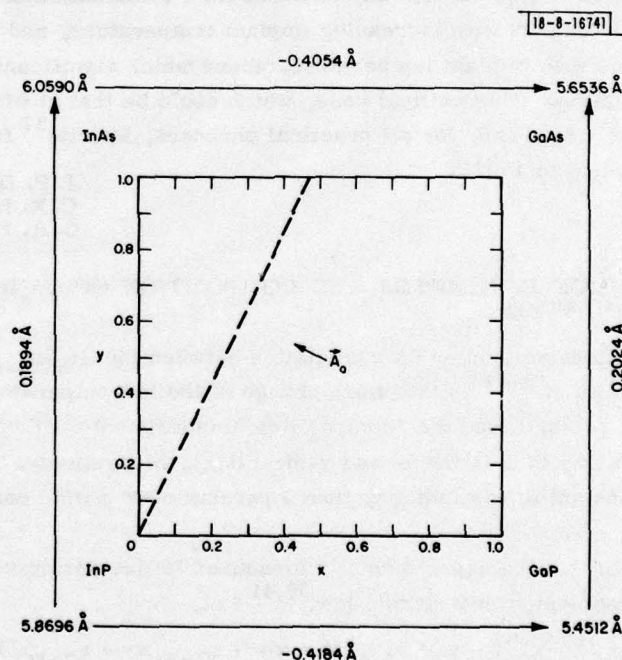


Fig. I-15. Diagram showing relation between room temperature lattice parameter and composition in $\text{Ga}_x\text{In}_{1-x}\text{As}_y\text{P}_{1-y}$ system. Dashed curve represents compositions for exact lattice match to InP. Vector \vec{A}_0 is that defined in Eq. (I-5).

Table I-2 shows the comparison of the present formulation with some experimental results. The compositions of the $\text{Ga}_x\text{In}_{1-x}\text{As}_y\text{P}_{1-y}$ layers were obtained by the electron microprobe

TABLE I-2 COMPARISON OF THE EXPERIMENTAL AND CALCULATED LATTICE-PARAMETER DIFFERENCES OF SOME $\text{Ga}_x\text{In}_{1-x}\text{As}_y\text{P}_{1-y}$ SAMPLES						
x	y	$(\Delta a/a)_{\text{exp}}$ (percent)	Δx	Δy	$(\Delta a/a)'_{\text{exp}}$ (percent)	$(\Delta a/a)_{\text{calculated}}$ (percent)
0.2597	0.5914	-0.1	0	0	0	0
0.186	0.363	-0.3	-0.0737	-0.2284	-0.2	-0.22
0.177	0.558	0.41	-0.0827	-0.0334	0.51	0.47
0.158	0.667	0.57	-0.1017	0.0756	0.67	0.95

technique. The lattice mismatch between the layers and the underlying InP substrates, $(\Delta a/a)_{\text{exp}}$ in Table I-2, were obtained by x-ray diffraction. For comparison with the present technique, one of the four samples is chosen as the reference point, from which the changes in composition, Δx and Δy , and the changes in lattice parameter, $(\Delta a/a)'_{\text{exp}}$, were measured. Using Eqs. (I-3) and (I-5) and Δx and Δy in Table I-2, the values of $(\Delta a/a)_{\text{calculated}}$ were obtained. There is a good agreement between $(\Delta a/a)_{\text{calculated}}$ and $(\Delta a/a)'_{\text{exp}}$ except for the largest $\Delta a/a$.

In conclusion, a vector formulation has been discussed in which the change of $\text{Ga}_x\text{In}_{1-x}\text{As}_y\text{P}_{1-y}$ lattice parameter is related to the change in composition in a simpler and clearer way. We believe that the present technique is potentially useful in the development of lattice-matched $\text{Ga}_x\text{In}_{1-x}\text{As}_y\text{P}_{1-y}/\text{InP}$ double-heterostructure lasers.

Z. L. Liao
J. J. Hsieh

REFERENCES

1. D. H. Auston, Appl. Phys. Lett. 26, 101 (1975).
2. R. Castagne, S. Laval, and R. Laval, Electron. Lett. 12, 438 (1976).
3. R. A. Lawton and A. Scavannec, Electron. Lett. 11, 74 (1975).
4. For example, see A. J. Low and J. E. Carroll, Solid-State Electron. Devices 2, 185 (1978).
5. A. M. Johnson and D. H. Auston, IEEE J. Quantum Electron. QE-11, 283 (1975).
6. E. S. Yang, P. G. McMullin, A. W. Smith, J. Blum, and K. K. Shih, Appl. Phys. Lett. 24, 324 (1974).
7. T. L. Paoli, IEEE J. Quantum Electron. QE-13, 351 (1977).
8. G. Arnold and K. Petermann, Opt. & Quantum Electron. 10, 311 (1978).
9. J. P. van der Ziel, J. L. Merz, and T. L. Paoli, J. Appl. Phys. 50, 4620 (1979).
10. R. W. Dixon and H. R. Beurier, Appl. Phys. Lett. 34, 560 (1979).
11. R. L. Hartman, R. A. Logan, L. A. Koszi, and W. T. Tsang, J. Appl. Phys. 50, 4616 (1979).
12. J. J. Hsieh, Appl. Phys. Lett. 28, 283 (1976), DDC AD-A025631/3.
13. J. J. Hsieh, J. A. Rossi, and J. P. Donnelly, Appl. Phys. Lett. 28, 709 (1976), DDC AD-A028550/2.
14. J. J. Hsieh, unpublished.
15. Solid State Research Report, Lincoln Laboratory, M.I.T. (1977:4), p. 1, DDC AD-A052463/7.
16. C. E. Hurwitz and J. J. Hsieh, Appl. Phys. Lett. 32, 487 (1978), DDC AD-A060752/3.
17. K. Nishida, K. Taguchi, and Y. Matsumoto, Appl. Phys. Lett. 35, 251 (1979).
18. K. Taguchi, Y. Matsumoto, and K. Nishida, Electron. Lett. 15, 453 (1979).
19. J. P. Donnelly and C. E. Hurwitz, Appl. Phys. Lett. 31, 418 (1977), DDC AD-A050856/4; also, Solid State Research Report, Lincoln Laboratory, M.I.T. (1977:3), p. 8, DDC AD-A050551/1.
20. D. E. Davies, J. P. Lorenzo, and T. G. Ryan, Solid-State Electron. 21, 981 (1978).
21. J. J. Berenz, F. G. Frank, and T. L. Hierl, Electron. Lett. 14, 683 (1978).
22. J. P. Donnelly and C. E. Hurwitz, Solid-State Electron. 21, 475 (1978), DDC AD-A053929/6.
23. W. T. Devlin, K. T. Ip, D. P. Leta, L. F. Eastman, and G. H. Morrison, in Gallium Arsenide and Related Compounds (St. Louis) 1978, C. M. Wolfe, Ed. (The Institute of Physics, London, Conf. Ser. 45, 1979), p. 510.
24. J. P. Donnelly and C. A. Armiento, Appl. Phys. Lett. 34, 96 (1979), DDC AD-A069910/8; also, Solid State Research Report, Lincoln Laboratory, M.I.T. (1978:4), p. 1, DDC AD-A068563/6.
25. C. A. Armiento, J. P. Donnelly, and S. H. Groves, Appl. Phys. Lett. 34, 229 (1979), DDC AD-A069937/1.
26. D. E. Davies, W. D. Potter, and J. P. Lorenzo, J. Electrochem. Soc. 125, 1845 (1978).
27. K. R. Gleason, H. B. Dietrick, R. L. Henry, E. D. Cohen, and M. L. Bark, Appl. Phys. Lett. 32, 578 (1978).
28. K. R. Gleason, H. B. Dietrick, M. L. Bark, and R. L. Henry, Electron. Lett. 14, 643 (1978).
29. D. E. Davies, J. J. Comer, J. P. Lorenzo, and T. G. Ryan, Appl. Phys. Lett. 35, 142 (1979).

30. J. P. Donnelly, C. A. Armiento, V. Diadiuk, and S. H. Groves, Appl. Phys. Lett. 35, 74 (1979), DDC AD-A076746.
31. L. J. van der Pauw, Philips Res. Rep. 13, 1 (1958).
32. J. P. Donnelly and C. E. Hurwitz, Solid-State Electron. 20, 727 (1977), DDC AD-A054406/4.
33. J. D. Sansbury and J. F. Gibbons, Radiat. Effect 6, 269 (1970).
34. W. J. Johnson and J. F. Gibbons, Projected Range Statistics of Semiconductors (Stanford University Bookstore, 1970); also J. F. Gibbons, W. T. Johnson, and S. W. Mybroie, Project Range Statistics (Halsted Press, New York, 1975).
35. J. Lindhard, M. Scharff, and H. Schiott, K. Dan. Vidensk. Selsk., Mat.-Fys. Medd. 33, 1 (1963).
36. R. Zolch, H. Ryssel, H. Kranz, H. Reichl, and I. Range, in Ion Implantation in Semiconductors and Other Materials, 1976, F. Chernow et al., Eds. (Plenum, New York, 1977), p. 593.
37. W. Rothmund and C. R. Fritzsche, J. Vac. Sci. Technol. 16, 968 (1979).
38. B. K. Shin, D. C. Look, Y. S. Park, and J. E. Ehret, J. Appl. Phys. 47, 1574 (1976).
39. R. L. Moon, G. A. Antypas, and L. W. James, J. Electron. Mater. 3, 635 (1974).
40. J. J. Hsieh, J. Electron. Mater. 7, 31 (1978), DDC AD-A054571/5.
41. R. E. Nahory, M. A. Pollack, W. D. Johnston, Jr., and R. L. Barns, Appl. Phys. Lett. 33, 659 (1978).

II. QUANTUM ELECTRONICS

A. REMOTE SENSING OF ATMOSPHERIC NO

In the previous Solid State Research Report,¹ a description was given of a differential-absorption LIDAR system which used a frequency-doubled CO₂-laser output as the coherent radiation source for the remote sensing of CO. Here, we report preliminary results of the use of this system for the remote detection of NO in the atmosphere. The detection of NO in the atmosphere using optical-absorption techniques is difficult because the fundamental 1-0 absorption band of NO occurs near 5.3 μm, a spectral region where the interference due to water-vapor absorption is quite severe. The only coincidence between a doubled mini-TEA CO₂-laser frequency and a well-populated NO absorption line which also lies in a region of relatively low atmospheric absorption is that between the doubled P(24) of the (10⁰)-(00⁰1) band and the R(1/2)_{1/2} absorption line of NO near 5.316 μm (Ref. 2). Nearby off-resonance lines with comparable atmospheric attenuation which can be used for differential absorption are the doubled P(26) and P(14) lines of the CO₂ laser. This may be seen in Fig. II-1, which shows a computer-generated atmospheric transmission spectrum³ along with the location of the doubled CO₂-laser frequencies; it is evident that both the P(26) and P(14) off-resonance lines and the on-resonance P(24) line are strongly attenuated by water vapor.

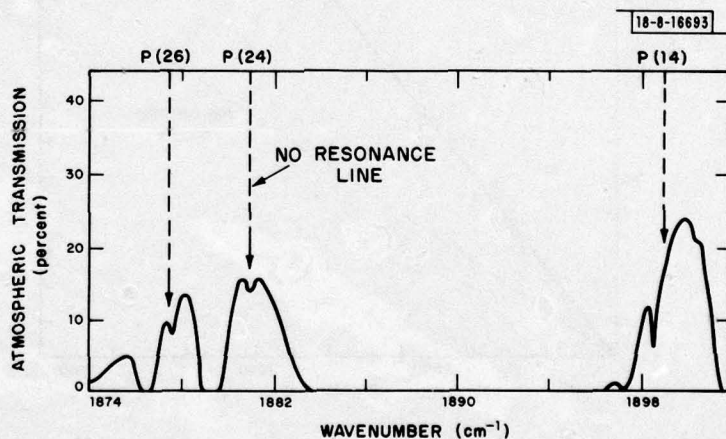


Fig. II-1. Computer-generated transmission curve for 3-km path at 296 K and 29-percent relative humidity (Ref. 3) showing positions of frequency-doubled CO₂-laser transitions used and R(1/2)_{1/2} absorption line of NO.

The differential-absorption LIDAR equation which relates the average atmospheric NO concentration N_a to the known concentration in a calibration cell N_c is given by

$$N_a = \frac{N_c L}{2R} \left[\frac{2(\beta' - \beta) R - \ln(P_a/P'_a)}{-\ln(P_c/P'_c)} \right] \quad (\text{II-1})$$

where P_a is the signal returned from a topographic target at a range R , P_c is the signal after passing once through a cell of length L , and β is the atmospheric attenuation (not including that due to NO), all at the on-resonance frequency. The off-resonance values are indicated by primes.

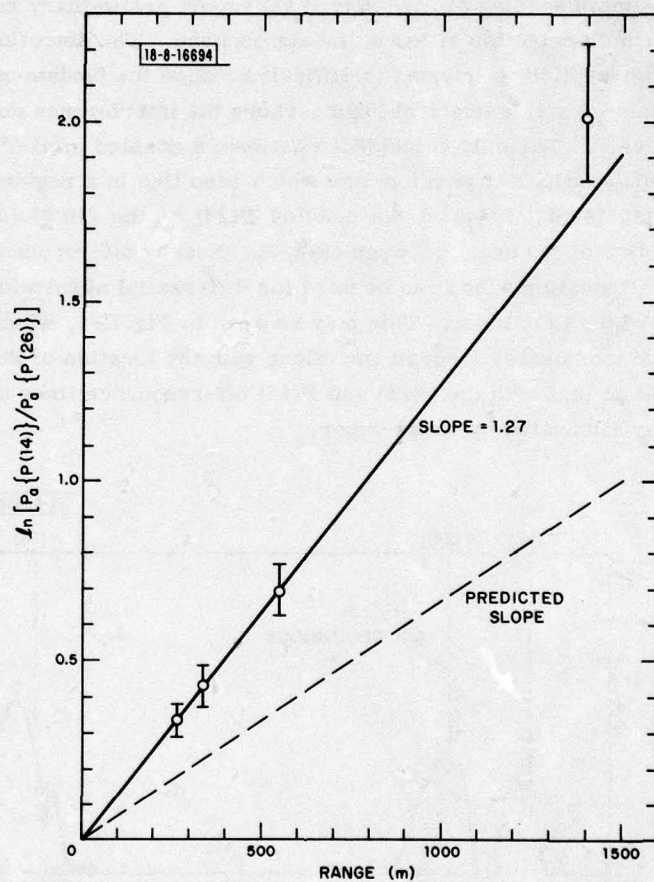


Fig. II-2. Logarithmic ratio of returned signals from off-resonance frequency-doubled P(14) and P(26) CO₂-laser radiation as a function of range. Dashed line corresponds to values predicted by AFGL tape.

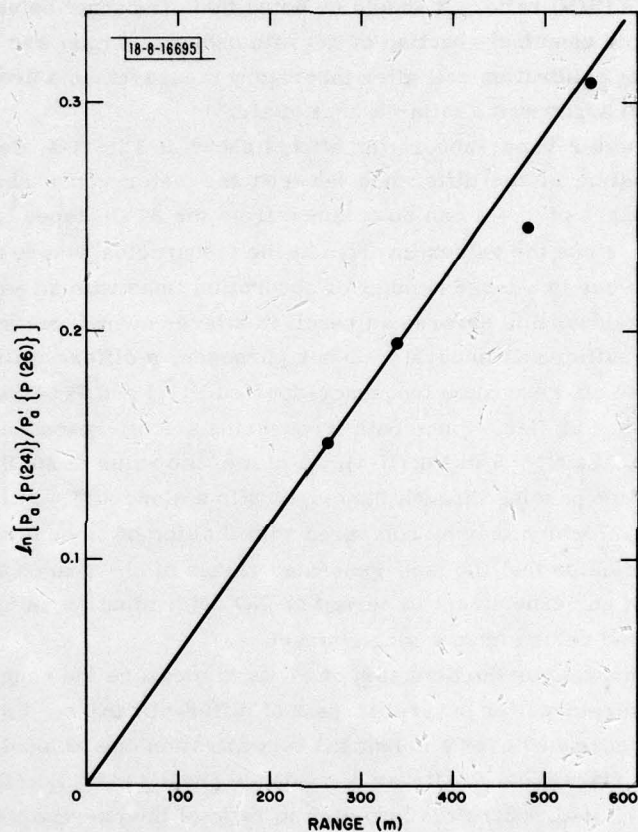


Fig. II-3. Logarithmic ratio of returned signals from on-resonance frequency-doubled P(24) and off-resonance frequency-doubled P(26) CO₂-laser radiation. Deviation of 480-m point from solid line corresponds to 90 ppb average NO concentration.

To establish the sensitivity with which we could measure NO in the atmosphere, a large argon-filled tank measuring 60.5 cm diam \times 104.5 cm length with Mylar windows was placed between the LIDAR system and a topographic target (foliage) located 550 m from the Laboratory. The decrease in the returned signal at the resonance frequency along this atmospheric path upon insertion of a known amount of NO into the tank agreed with laboratory measurements using a 50-cm absorption cell and indicated an NO detection sensitivity of 40 parts per billion (ppb) for a unity signal-to-noise (S/N) ratio. It should be noted that air cannot be used as the buffer gas with NO due to the rapid chemical reaction of NO with oxygen. Argon was used as the buffer gas in both the tank and the calibration cell after laboratory measurements determined that the pressure broadening due to argon was similar to that of air.

Given the strong water-vapor-absorption effects shown in Fig. II-1, detection of NO requires an accurate determination of the difference between the water-vapor absorption off- and on-resonance, $\beta' - \beta$. Values of $\beta' - \beta$ can be obtained from the AFGL tapes⁴ for known atmospheric conditions. However, since the values involved at the frequencies we are using are based on the theoretical attenuation due to a large number of absorption lines with an assumed Lorentzian line-shape, small individual line errors can result in a large overall discrepancy. To establish if the tape values are sufficiently accurate for our purposes, a differential-absorption comparison was made using the off-resonance frequency-doubled P(26) and P(14) lines. Our experimental results are shown in Fig. II-2. Since both frequencies are off-resonance and will not be absorbed by NO, we can take $N_a = 0$ in Eq. (II-1). A plot of the value of $\ln(P_a/P'_a)$ vs range will then lie on a straight line passing through the origin with a slope $2(\beta' - \beta)$. As seen in Fig. II-2, the deduced slope is 1.27 which may be compared with the line of slope 0.68 predicted from the AFGL tapes. This indicates that the tape-generated values of $\beta' - \beta$ are not sufficiently accurate under the conditions of our experiment to permit an NO determination using differential absorption of the backscattered return from a single target.

An alternative approach for the detection of NO is to measure the range dependence of the differential-absorption returns for several targets at different ranges. Using the arguments described above, the increases over ambient NO concentration due to localized NO emission should result in a departure from the linear dependence predicted by Eq. (II-1). Such measurements are shown in Fig. II-3, where the logarithmic ratio of the on-resonance P(24) and the off-resonance P(26) LIDAR return from several targets as a function of range is given. Since the ambient concentration of NO is negligibly small⁵ (~ 1 ppb) away from a source (e.g., vehicle exhaust), one obtains the slope $2(\beta' - \beta)$ from the line through the origin and the two inner data points in Fig. II-3, which were from targets removed from the roadway. The value so obtained was $\beta' - \beta = 0.285$. The presence of a localized concentration of NO along the path to the target at 480 m is clearly indicated by the departure of the point from the ambient extinction line. The beam to this target crossed a major roadway at a height of 3 m, and the point shown corresponds to an average NO concentration of 90 ppb over the path. Later measurements over this path, taken during a period of high traffic density, yielded average concentrations in excess of 200 ppb. The path to the 550-m range point crosses the same roadway, but at a height of 15 m. The slight departure from the line corresponds to an average concentration of 15 ppb, which is well within our experimental sensitivity. The rapid falloff of NO concentration between 3 and 15 m above the roadway is indicative of a strong localization of NO, and hence a high concentration in the immediate vicinity of the roadway.

These results, while preliminary, demonstrate the feasibility of using frequency-doubled CO₂-laser radiation for remote monitoring of NO in the atmosphere despite large water-vapor-absorption effects. This capability will be considerably enhanced by an improved data-processing system and by an accurate measurement of the water-vapor absorption at the doubled mini-TEA CO₂-laser frequencies; this will eliminate the need for multiple-target measurements and will permit differential-absorption measurements of atmospheric NO using backscattered return from a single target.

N. Menyuk
D. K. Killinger
W. E. DeFeo

B. LIMITATIONS ON THE FREQUENCY-DOUBLING EFFICIENCY IN CdGeAs₂

The ternary chalcopyrite compound CdGeAs₂ with a transmission range of 2.5 to 17.5 μm is one of the most useful infrared nonlinear materials. As an example, the highest frequency-doubling efficiency of 27 percent for CO₂-laser radiation was observed in this material.⁶

Here, we report the observation of a maximum second-harmonic output energy of 340 mJ at 5.3 μm at a 10-percent efficiency. This was achieved using a TEM₀₀ mode, CO₂ TEA oscillator-amplifier system with a maximum output energy of 3.5 J and a pulse duration of 70 nsec. The laser beam was weakly focused by a 4.7-m-radius mirror into the doubling crystal, which was inserted in the converging beam at a position where the beam spot size⁷ was 11.5 mm. The AR-coated doubling crystal was 11 mm long and had a 13- \times 21-mm² cross section. It was cooled to liquid nitrogen temperature in order to minimize absorption losses. The measured absorption constants at 80 K were 0.15 and 0.6 cm⁻¹ at 10.6 and 5.3 μm , respectively. Figure II-4 shows the dependence of the second-harmonic output energy on the input energy. The solid line corresponds to the expected square-law dependence when there are no limiting effects. There is evidence of saturation at the highest input energies. This agrees with previous observations that the second-harmonic conversion efficiency saturates at lower levels than expected from linear absorption measurements and pump depletion considerations. Experimentally, we have found that the maximum second-harmonic energy-conversion efficiency increases linearly with crystal length for lengths up to at least 15 mm, and the maximum conversion efficiency in percent is approximately two times the interaction length in millimeters for an AR-coated crystal. According to this simple rule, the maximum conversion efficiency in Fig. II-4 should have been about 22 percent. In contrast, the observed efficiency was 10 percent. This experiment, however, was designed to maximize the second-harmonic output energy under the constraints of saturation and laser-induced surface breakdown. A large spot size was therefore chosen and some of the incident CO₂-laser power missed the doubling crystal, thus reducing the doubling efficiency by about 50 percent in the small signal limit.

The exact mechanism leading to saturation in CdGeAs₂ has not yet been determined. In order to better characterize the saturation process, we have made measurements using 8-nsec pump pulses. This allows higher pump intensities on the sample before laser-induced breakdown than are obtainable with the approximately 100-nsec pulses available from a standard CO₂ TEA laser. The short pulses were generated using a short-pulse CO₂ oscillator-amplifier system.⁸ Figure II-5 shows the observed second-harmonic conversion efficiency for an 11-mm-long crystal using, respectively, 8- and 80-nsec pump pulses. The onset of saturation is determined by the pump power and not by the pump energy for a fixed spot size. The saturation process must therefore have a response time shorter than 8 nsec. The figure shows that the conversion

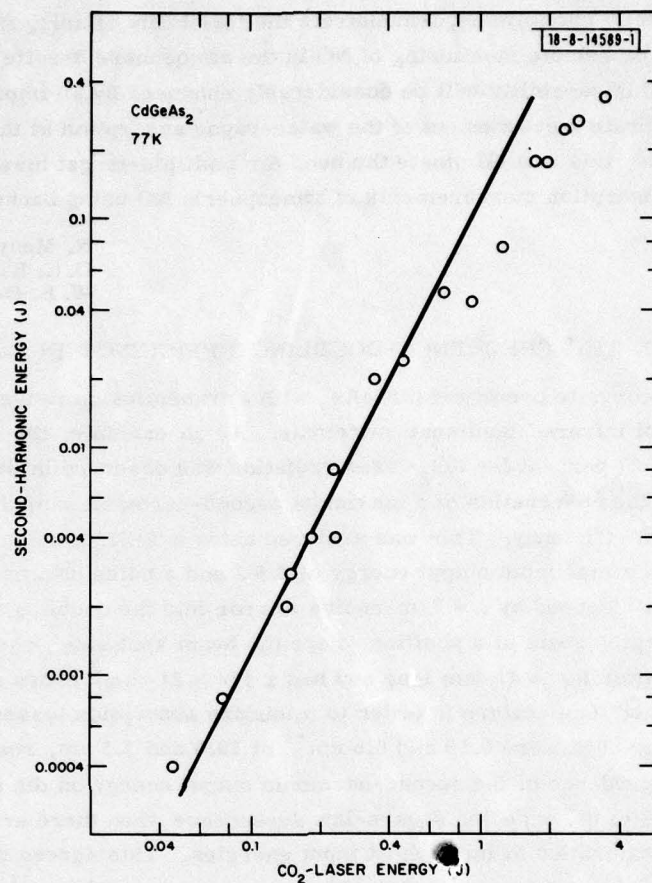


Fig. II-4. Second-harmonic output at 5.3 μm from an 11-mm-long, 13- \times 21-mm² cross section, AR-coated CdGeAs₂ crystal.

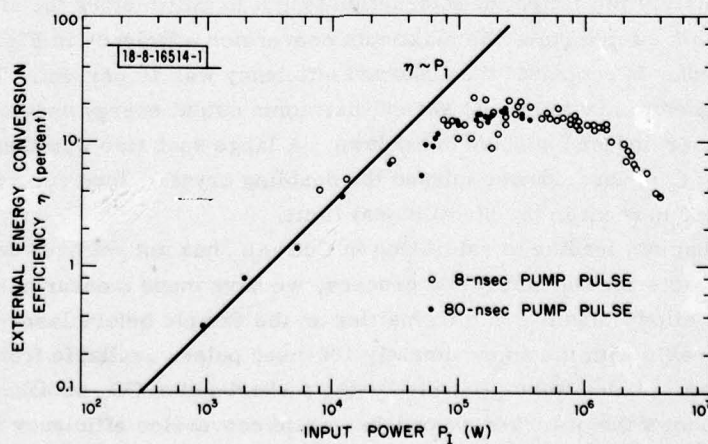


Fig. II-5. Second-harmonic conversion efficiency of 10.6- μm radiation in CdGeAs₂ for two different pump-pulse durations (11-mm-long AR-coated crystal, 650- μm spot size).

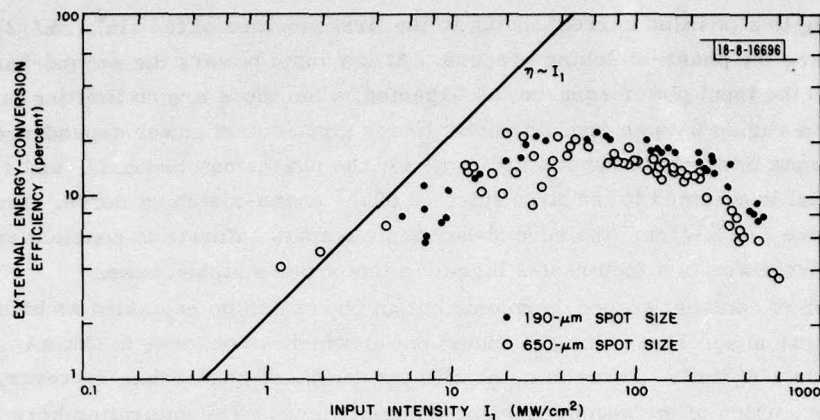


Fig. II-6. Second-harmonic conversion efficiency of 10.6- μm radiation in CdGeAs_2 for two different focusing conditions (11-mm-long AR-coated crystal, 8-nsec pump-pulse duration).

efficiency reaches a maximum and then decreases, with a further increase in input power. Figure II-6 depicts the measured conversion efficiency for two different spot sizes. It shows that the input intensity is the proper parameter for characterizing the saturation process.

In Figs. II-5 and II-6, the saturation behavior was examined with the doubling crystal oriented in its phase-matching position. Figure II-7 illustrates the effect of angle tuning the crystal from

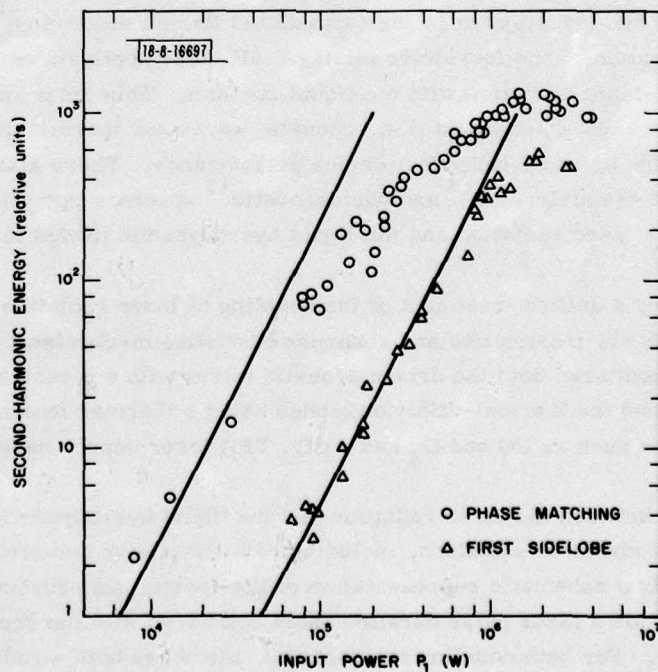


Fig. II-7. Second-harmonic output at 5.3 μm from CdGeAs_2 crystal oriented at its phase-matching position and at first sidelobe of its phase-matching curve (1-mm-long AR-coated crystal, 650- μm spot size, 8-nsec pump-pulse duration).

phase matching to a position corresponding to the first sidelobe of the $\sin^2 (\Delta k l / 2) / (\Delta k l / 2)^2$ curve describing the phase-matching process. At low input powers the second-harmonic output increases with the input power squared, as expected, when there are no limiting processes. This is followed by a region with an approximately linear input-output power dependence. The onset occurs at an input intensity of about 4 MW/cm² for the phase-matched case, and 150 MW/cm² when the crystal is oriented to the first sidelobe of the phase-matching curve. Finally, at input intensities above 220 MW/cm² the second-harmonic outputs saturate to constant values. The maximum output power is a factor-of-2 higher in the phase-matched case.

The region of constant second-harmonic output power can be explained as being due to a substantial nonlinear absorption of the CO₂ pump power which we observe in CdGeAs₂ at input intensities above 200 MW/cm². There is no significant nonlinear absorption, however, associated with the linear portion of the second-harmonic output curve. The saturation here is therefore probably related to the breaking of the phase-matching condition.

The nonlinear absorption and the breaking of the phase-matching condition may be due to the same process. Recently, nonlinear absorption of CO₂-laser radiation, producing a nonequilibrium electron-hole plasma, has been reported^{9,10} in Ge, InAs, InSb, and Hg_{1-x}Cd_xTe. The same process may also occur in CdGeAs₂. From our experiments, this would imply a free carrier lifetime of less than 8 nsec. The generated excess carriers would affect the phase-matching condition before significant absorption is observable.

H. Kildal

C. LASER-DRIVEN ACOUSTIC AND THERMAL-DIFFUSION MODES IN LIQUIDS

Interest in the use of liquid media for nonlinear optical devices has increased recently. Processes that have been investigated include stimulated Raman scattering,¹¹ Kerr switching,¹² third-harmonic generation,¹³ and four-wave mixing. All these applications involve the interaction of intense pulsed-laser radiation with the liquid medium. This laser radiation also couples to the hydrodynamic modes of the liquid (i.e., acoustic waves and thermal diffusion); the resulting density fluctuations, in turn, can affect device performance. There also has been a parallel development of both thermal-lensing¹⁴ and photoacoustic¹⁵ spectroscopy which utilize these interactions between the laser radiation and the liquid hydrodynamic modes to probe weak absorption bands in liquids.

We have developed a unified treatment of the coupling of laser radiation to the liquid hydrodynamic modes. Both electrostrictive and absorptive coupling mechanisms are included. Experimentally, we have monitored both the driven acoustic waves with a piezoelectric detector immersed in the liquid and the thermal-diffusion modes using a thermal-lensing technique. Simple cryogenic liquid media such as CO and O₂ and a CO₂ TEA laser source have been used for the measurements.

The interactions between the laser radiation and the liquid hydrodynamic modes are described by the linearized hydrodynamic equations, including both absorptive and electrostrictive coupling.¹⁶ Figure II-8 is a schematic representation of the density perturbations driven by the two coupling mechanisms for a laser pulse duration short compared with the acoustic transit time across the laser spot. For both coupling mechanisms, there are both a radially propagating acoustic wave and a slowly diffusing thermal excitation. However, the acoustic and thermal-diffusive components of the density variations driven by absorption are comparable in magnitude, while for electrostrictive coupling the thermal-diffusion component is smaller than the acoustic

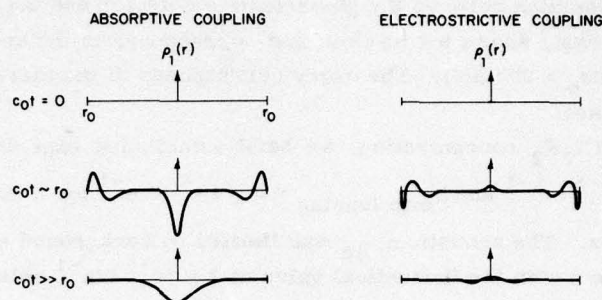


Fig. II-8. Schematic representation of density perturbations driven by both absorptive and electrostrictive coupling to liquid-acoustic and thermal-diffusion modes. Electrostrictive coupling to the thermal-diffusion mode is exaggerated for clarity.

component by a factor of $\lambda/(\rho_o c_p c_o w_o) \approx 10^{-6}$. Here λ is the thermal conductivity, c_p is the heat capacity, ρ_o is the density, c_o is the acoustic velocity, and w_o is the laser spot size. This parameter is essentially the ratio of the thermal-diffusion velocity to the acoustic velocity.

Electrostriction, which has only a weak spectral dependence, sets a limit on the absorptivity that may be measured by the thermal-lensing and photoacoustic techniques. A useful figure of merit is the absorptivity, α_{\min} , at which the absorptively and electrostrictively driven signals are equal. We find $\alpha_{\min \text{ acoustic}} = \gamma_e c_p / (2\beta c c_o w_o n)$ and $\alpha_{\min \text{ lensing}} = [\lambda(\gamma - 1) / (c_o c_p c_o w_o)] \alpha_{\min \text{ acoustic}}$, where $\gamma_e = (n^2 - 1)(n^2 + 2)/3$ is the electrostrictive coupling constant, with n the liquid refractive index, β the thermal expansivity, and c the vacuum speed of light. Since the electrostrictive coupling depends on the gradient of the laser intensity and is therefore larger for a tighter focus, both these expressions show an inverse dependence on laser spot size. However, note that the lensing experiment scales as $1/w_o^2$, while the acoustic experiment goes only as $1/w_o$.

In Fig. II-9 we show the experimentally measured acoustic and thermal-lensing signals for absorptive coupling in liquid CO doped with a small amount of CCl_2F_2 for an input laser energy

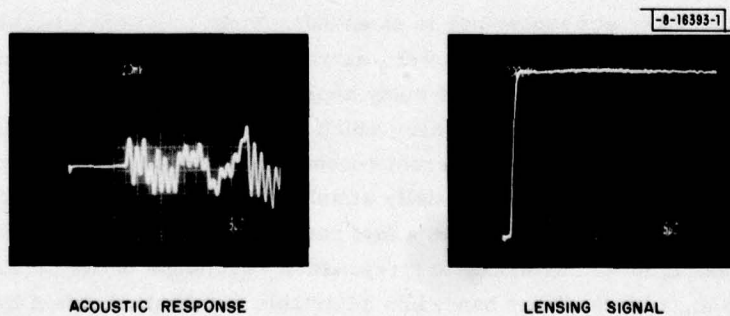


Fig. II-9. Comparison of acoustic and thermal-lensing monitors of absorption in liquid CO.

of 7.5 mJ in a 100-nsec-duration pulse. The acoustic signal shows a delay which corresponds to the propagation time from the laser spot to the acoustic detector. The ringing is due to the acoustic impedance mismatch between the piezoelectric detector and the liquid. The thermal-lensing signal, in contrast, shows a rise time that corresponds to the acoustic propagation across the laser spot ($w_0 = 200 \mu\text{m}$). The decay corresponds to the thermal-diffusion time and is approximately 40 msec.

By varying the CCl_2F_2 concentration, we have established experimental values of $\alpha_{\text{min acoustic}} = 4 \times 10^{-5} \text{ cm}^{-1}$ and $\alpha_{\text{min lensing}} = 6 \times 10^{-7} \text{ cm}^{-1}$ for a 200- μm spot-size focus in the cryogenic liquids. The acoustic α_{min} was limited by background electrostrictive coupling and is in good agreement with the theoretical value of $2 \times 10^{-5} \text{ cm}^{-1}$ obtained from the expression given above. The lensing α_{min} was limited by probe laser fluctuations and did not reach the calculated electrostrictively limited value of $\sim 2 \times 10^{-11} \text{ cm}^{-1}$ for this geometry. Thus, electrostriction places a less severe constraint on the measurement of weak absorptions in liquids by the thermal-lensing techniques than by the acoustic technique. It should be noted that the thermal-lensing technique is really measuring the variation of the refractive index due to perturbations of the liquid density. Interferometric techniques allow this measurement to be made at much lower absolute index variations and hence lower laser energies, but the limitations set by electrostriction remain unchanged.

In summary, we have carried out a theoretical and experimental investigation of the coupling of pulsed laser radiation to the hydrodynamic modes of liquids. The limitations posed by electrostrictive coupling on the minimum measurable absorptivity have been evaluated, and thermal lensing has been shown to be capable of measuring smaller absorptivities than photoacoustic experiments.

S. R. J. Brueck
H. Kildal
L. J. Belanger

D. APPLICATION OF PHOTODISSOCIATION LASERS TO CHEMICAL ANALYSIS

Incoherent resonance-line optical sources are widely used for detecting trace metal atom concentrations. They are routinely used, for example, in monitoring industrial chemical processes, in quantitative analysis, and in kinetics measurements.¹⁷ Dye-laser technology has made possible the development of coherent optical sources at the wavelengths of resonance lines. These laser sources have vastly superior spectral brightness in comparison with incoherent sources, thus increasing the S/N ratio for applications involving long optical paths, such as remote sensing in the upper atmosphere or in extended-sample chemical analysis. However, the technology required to obtain even low-power, narrow-band, frequency-locked dye lasers seems unavoidably complex and cumbersome for many applications.¹⁷

The UV-pumped photodissociation lasers which we have recently demonstrated¹⁸ provide an alternate approach for generating coherent resonance-line probes for many alkali and Group IIIa metals. The lasers are potentially simple and inexpensive to construct, involving only a heated, sealed-off, sample cell and a fast rare-gas monohalide flashlamp for a pump source. Each laser is locked naturally to a resonance wavelength of the particular metal used in the laser medium, with the laser bandwidth adjustable to a limited extent by varying the pump wavelength. To determine the utility of photodissociation lasers as sources for quantitative chemical analysis, we have carried out a series of measurements making use of these lasers

for analytical flame spectroscopy. The specific method chosen was laser-enhanced ionization (LEI).¹⁹

The apparatus consists of a modified Perkin-Elmer Model 370 premixed burner assembly, a photodissociation laser, and detection electronics. Details of the configuration have been published elsewhere.¹⁹ The analytical procedure involves aspirating a sample of the unknown into the flame in aqueous solution. The atomic impurity of interest is then detected as an increase in the flame conductivity following laser-assisted ionization via optical excitation of the neutral atom. The minimum concentration detection limits and dynamic range for Tl and Na analysis were determined for a system consisting of ArF-laser-pumped TlI and NaI resonance-line lasers, and a hydrogen compressed-air flame.

Both Tl and Na were detected over a useful dynamic range in concentration of 4 orders of magnitude. Detection limits, established at single-shot S/N ratios of 2, were 10 and 1 ppb (weight-percent), respectively. Detection of lower concentrations would be possible by reducing RFI noise pickup from the laser discharge and/or by using digital signal averaging. In addition it was found that two-step optical excitation, as is possible with a multiple-wavelength photodissociation laser, can markedly increase the sensitivity of the LEI technique. For example, a 100× improvement was found for the specific case using the NaI laser, which has a cascade, infrared-visible laser output. Results with the TlI laser also show that a multiple-wavelength photodissociation laser, involving a common upper level, may be useful as an accurate remote temperature probe.

In the course of these experiments, the Na content of laboratory "de-ionized" water was measured to be 15 ppb, i.e., 15 ng/ml.

D. J. Ehrlich G. C. Turk†
R. M. Osgood, Jr. J. C. Travis†

E. LASER-INDUCED MICROSCOPIC ETCHING OF GaAs AND InP

It has recently been shown that UV lasers may be used to produce localized photodeposition of metal films of microscopic dimensions.²⁰ In this report, we describe a closely related process in which a low-power UV-laser beam has been used to localize and control gas-phase photochemical etching on GaAs and InP surfaces. Such a process may have applications in the area of device fabrication for microelectronics and integrated optics.

The reactions involved utilize halogen atom reactants, Cl, Br, or I, which are liberated by UV-laser photolysis of halogenated methane gases. Similar heterogeneous etching reactions on Si and Ge have been studied by photolysis of Br₂ at visible wavelengths with a relatively high-power argon-ion laser.²¹ Laser photoetching of GaAs has been demonstrated using a liquid-phase etchant in a reaction which involved the photogeneration of carriers in the semiconductor.²² The particular objective of the study reported here is to demonstrate that low-power UV lasers can be used to initiate gas-phase photolysis reactions which lead to micrometer-scale etched features.

In the present experiments, the 514.5-nm output of a CW argon-ion laser was frequency-doubled in an ADP crystal to produce a 4-mW beam at 257.2 nm. The UV beam was focused into a gas cell and onto the surface of an enclosed semiconductor sample. The samples used were n-InP ($n = 10^{15} \text{ cm}^{-3}$) and n-GaAs ($3 \times 10^{18} \text{ cm}^{-3}$ Si), both oriented in a (100) plane. Surfaces were degreased in methanol and used without further preparation. Thin, amorphous GaAs films, used for the transmission experiments to be described below, were prepared by sputtering.

† Analytical Chemistry Division, National Bureau of Standards, Washington, D. C.



Fig. II-10. Optical micrograph of feature produced by laser-controlled etching of InP via photolysis (see text).

TABLE II-1 LASER-INDUCED ETCH RATES FOR InP AND GaAs USING A CW 257.2-nm LASER (SPOT SIZE 19 μm FWHM)		
Substrate	Etchant	Rate at 100 W/cm ² (Å/sec)
n-GaAs, (100)	CH ₃ Br 750 Torr	5.2
n-InP, (100)	CH ₃ Br 750 Torr	9.4
GaAs, Amorphous	CH ₃ Br 750 Torr	9.7
GaAs, Amorphous	CF ₃ I 25 Torr	9.9×10^{-2}
n-InP, (100)	CH ₃ Cl 1000 Torr	—

The thicknesses of films formed in this way were calibrated by absorption measurements at near-UV wavelengths. After the semiconductor samples were irradiated with UV-laser light, they were examined either by Nomarski microscopy or by a scanning electron microscope.

Exposure of both GaAs and InP samples in CH_3Br or CF_3I to UV power levels exceeding 100 W/cm^2 causes a rapid reaction which, on a time scale of several seconds, leads to a diffuse, weakly luminescent surface film and a visible etchmark. Figure II-10 shows the result of CH_3Br etching of InP with the laser focused to a point beyond the sample. The Fresnel-diffraction pattern, which is reproduced in the InP, is caused by slight aperturization of the beam at the focusing lens. The smallest scale diffraction rings, $1.5 \mu\text{m}$ wide, correspond to the highest spatial frequencies passed by the single-element $f/6$ lens. Physical comparison of the etched regions revealed similar results for all cases. Etching was uniform and well confined to the region illuminated. In particular, differential etching around crystal defects, a characteristic of some wet chemical processes,²³ was not observed. By contrast, the luminescent product-films were found to be nearly uniformly distributed over the entire cell surface. These films could be easily removed with a methanol rinse and did not noticeably interfere with the etching process for etching to depths of several micrometers.

Relief patterns similar to that shown in Fig. II-10 were made for the other substrate/etchant combinations and scanned by mechanical (DektakTM) stylus. Etch rates, estimated from the exposure required to produce depressions of $0.5 \mu\text{m}$, are listed in Table II-1. Relatively modest differences were found between CH_3Br etching of InP and GaAs. Photoactivated etching with CF_3I , at a pressure giving gas absorption at 257.2 nm comparable to that used in CH_3Br etching, is less rapid and was measured only for amorphous GaAs (see below). A separate experiment using unirradiated diatomic halogen etchants indicates that this difference is primarily a result of the difference in rates of the Br and I surface reactions subsequent to photoactivation.²⁴ Etching of InP by CH_3Cl is observable, yet much slower – a result expected because of the very weak absorption of CH_3Cl at 257.2 nm . As a point of comparison, an upper limit of 10^{-3} \AA/sec was established for the "dark" reaction rates by checking for weight loss on GaAs and InP samples exposed to unilluminated CH_3Br at a pressure of 750 Torr for 2 weeks.

In conclusion, a class of dry, laser-activated processes has been demonstrated for etching of the III-V semiconductors GaAs and InP. The laser-activated etching can be driven at rates much greater than that of the background, "dark" reaction with a low-power, 1-mW, UV laser. Localization of the reaction to $\sim 1 \mu\text{m}$ is possible with a tightly focused UV beam, and it is expected, by analogy with laser-photodeposition,²⁰ that it will also be possible to produce structures of $\sim 0.2\text{-}\mu\text{m}$ or finer periodicity interferometrically. While significant aspects of the surface chemistry are unclear at this time, both the rate and resolution of the process appear understandable in terms of a simple physical model which assumes efficient use of chemisorbed halogen atoms at the semiconductor surface. Applications may include trimming of semiconductor devices or discretionary disconnect of integrated-circuit metal conductors. Direct fabrication of gratings for distributed-feedback lasers and other integrated optics devices should also be possible.

We would like to acknowledge J. C. C. Fan's important contribution in providing the sputtered GaAs films.

D. J. Ehrlich
R. M. Osgood, Jr.
T. F. Deutsch

TABLE II-2 TYPICAL PARAMETERS FOR THE FORMATION OF OHMIC CONTACTS ON p-InP USING PULSED-LASER PHOTODEPOSITION	
Pressure	1 to 5 Torr $\text{Cd}(\text{CH}_3)_2$
Fluence (193 nm)	1 to 5 J/cm^2
Shots	25 to 100
Resistance \times Area	$2 \times 10^{-4} \text{ ohm-cm}^2$

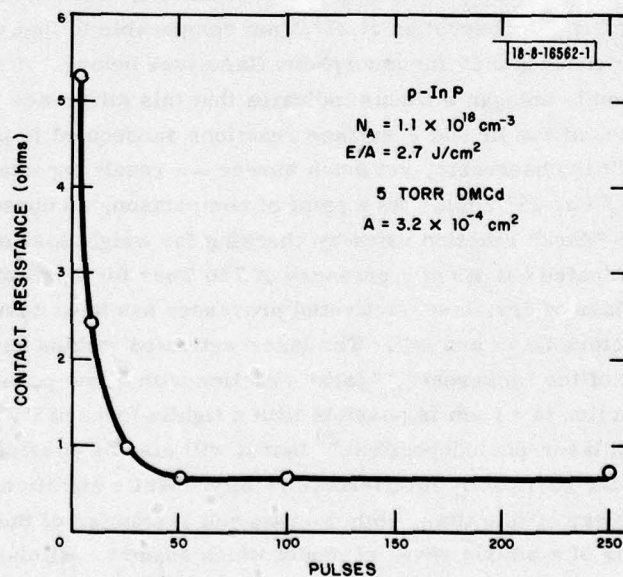


Fig. II-11. Resistance of photodeposited Cd contacts on p-InP vs number of 193-nm ArF-laser pulses.

F. FORMATION OF OHMIC CONTACTS ON p-InP BY UV-LASER PHOTODEPOSITION

We previously reported on the use of laser-initiated photolysis of metal alkyls to produce metallic deposits with micrometer-size features on insulating substrates.²⁰ We have now used a combination of photolysis and laser heating to produce ohmic contacts on p-type, zinc-doped (10^{18}-cm^{-3}) InP. Ohmic contacts to InP are of interest in the fabrication of GaInAsP/InP diode lasers. Conventional Au-Zn alloyed contacts are not completely satisfactory because the evaporation and alloying processes are not entirely controllable and reproducible. Recently, ohmic contacts on InP have been fabricated using laser Zn^+ or Cd^+ implantation and subsequent laser annealing.²⁵ The present technique is of interest since it is a simple one-step process for making contacts that avoids overall heating of the substrate.

In our experiments, a pulsed ArF laser operating at 193 nm is used to produce Cd or Zn deposits by the photolysis of $\text{Cd}(\text{CH}_3)_2$ and to locally heat the substrate to near the melting point, producing a highly doped surface layer. The output of the ArF laser is used to illuminate a 100- to 500- μm pinhole, which is then imaged onto an InP substrate mounted in a stainless cell. Typical deposition conditions are given in Table II-2. Subsequent to laser irradiation, samples are examined by Nomarski microscopy and their I-V characteristics are measured. In addition, the morphology of some contacts was evaluated using a DektakTM stylus. Auger electron spectroscopy was used to examine compositional changes.

Ohmic contacts were obtained under a variety of conditions. The best contacts obtained to date have a resistance-area product of $2 \times 10^{-4}\text{ ohm-cm}^2$; this compares with $3 \times 10^{-4}\text{ ohm-cm}^2$ for conventional Au-Zn alloy contacts on similar InP substrates. Results using either Zn or Cd depositions were essentially identical. Figure II-11 shows a typical variation of contact resistance with number of shots at a 193-nm fluence of 2.7 J/cm^2 . Fluence values were obtained using the area of the region of altered surface morphology and the flux incident on the substrate. The pressure dependence of the contact resistance was also examined. Ohmic contacts were not obtained for $\text{Cd}(\text{CH}_3)_2$ pressures of 0.5 Torr or less, while at pressures in excess of 5 Torr the gas became optically thick and deposition on the front window of the cell interfered with the formation of contacts. The usable range of energy fluences is limited by the occurrence of surface damage at the high-energy end and by increasing contact resistance at the low-energy end.

Contacts as small as 35 μm in diameter have been obtained. In most cases, good ohmic contacts have shown some surface damage extending to a few micrometers beneath the surface. This damage is due to heating of the InP to near the melting point, with subsequent phosphorous vaporization. Techniques to minimize this damage are being examined. Auger electron spectroscopy confirms the loss of phosphorus from the irradiated region.

The results appear consistent with a mechanism in which Cd produced by photolysis deposits on the InP in the region of the laser focal spot and is alloyed with InP that has been heated to the melting point by the laser. This is the first demonstration on UV-laser photolysis to produce ohmic contacts by a single-step process.

T. F. Deutsch R. M. Osgood, Jr.
D. J. Ehrlich Z. L. Liao

G. SUBMILLIMETER MIXERS AT CRYOGENIC TEMPERATURES

Considerable reduction in system noise temperature can be obtained by cooling millimeter and submillimeter wave mixers.^{26,27} In practice, however, this requires the mixer to be

designed to withstand the relative thermal contraction effects of cooling from room temperature. The mixer must also be able to accommodate repeated temperature cycling from room temperature to the cryogenic operating temperature with no degradation in performance. The cooling system must be constructed to cool the mixer in an optimal geometry with negligible optical loss.

A new system has been developed that utilizes a closed-cycle helium refrigerator and permits a short-focal-length focusing mirror and a diode mixer to be mounted within the vacuum chamber. Operationally, the diode mixer and focusing mirror are initially aligned and optimized at room temperature and the total system noise temperature is measured. The vacuum chamber is then closed and evacuated, the mixer is cooled, and the system noise temperature is remeasured.

Presently, small optical losses are introduced when the diode is mounted in the evacuated chamber of the helium refrigerator, as compared with an open configuration where all alignment adjustments are readily accessible. Consequently, the system noise temperature T_s with the diode mounted in the refrigerator, but uncooled, is slightly higher than T_s obtained in an open configuration. Nevertheless, upon cooling to 60 K, we obtain our best T_s to date — namely 3,800 K (DSB) at 432 μ .

The mixers used in the above experiments have employed newly developed corner reflectors with 2λ antennas. This design was obtained by parametric computer studies of radiation patterns and has also resulted in improved room-temperature sensitivities of 19,000 K at 185 μ m and 30,000 K at 120 μ m.

Work is in progress now to optimize the optics for the cryogenic system and to simultaneously cool the IF amplifier. The plan is to extend operation of these cooled mixer-IF amplifier combinations over the 3- to 0.1-mm-wavelength range.

H. R. Fetterman	C. D. Parker
B. J. Clifton	P. E. Tannenwald
P. F. Goldsmith†	

REFERENCES

1. Solid State Research, Lincoln Laboratory, M.I.T. (1979:3), pp. 9-13.
2. *Ibid.* (1979:2), pp. 17-21, DDC AD-A078676.
3. R. J. Nordstron, J. H. Shaw, W. R. Skinner, J. G. Clavert, W. H. Chan, and W. M. Uselman, "Application of Fourier Transform Spectroscopy to Air Pollution Problems," Report EPA-600/3-77-026 (1977).
4. R. A. McClatchey, W. S. Benedict, S. A. Clough, D. E. Burch, R. F. Calfree, K. Fox, L. S. Rothman, and J. S. Garing, "AFCRL Atmospheric Absorption Line Parameters Compilation," Report AFCRL-TR-73-0096, Environmental Research Paper No. 434 (1973).
5. J. H. Steinfeld, *Air Pollution* (McGraw-Hill, New York, 1975).
6. G. W. Iseler, H. Kildal, and N. Menyuk, in *Ternary Compounds 1977*, G. D. Holah, Ed. (The Institute of Physics, London, 1977), pp. 73-88, DDC AD-A054566/5.

† University of Massachusetts, Amherst.

7. H. Kogelnik and T. Li, *Appl. Opt.* 5, 1550 (1966).
8. H. Kildal and S. R. J. Brueck, Final Technical Report for the Period 1 March 1977 - 28 February 1979, prepared for DOE Under Contract No. ES-77-S-02-4251.
9. S. Y. Yuen, R. L. Aggarwal, N. Lee, and B. Lax, *Opt. Commun.* 28, 237 (1979).
10. S. A. Jamison and A. V. Nurmikko, *Phys. Rev. B* 19, 5185 (1979).
11. A. Z. Grasiuk and I. G. Zubarev, *Appl. Phys.* 17, 211 (1978).
12. Solid State Research Report, Lincoln Laboratory, M.I.T. (1979:2), p. 29, DDC AD-A078676.
13. S. R. J. Brueck and H. Kildal, *Opt. Lett.* 2, 33 (1978), DDC AD-A054569/9.
14. R. L. Swofford and J. A. Morrell, *J. Appl. Phys.* 49, 3667 (1979).
15. A. C. Tam, C. K. N. Patel, and R. J. Kerl, *Opt. Lett.* 4, 81 (1979).
16. W. Kaiser and M. Maier, in *Laser Handbook*, Vol. II, F. T. Arecchi and E. O. Schulz-Dubois, Eds. (North-Holland, Amsterdam, 1972), p. 1113.
17. R. Green, J. Travis, and R. Keller, *Anal. Chem.* 48, 1954 (1976).
18. D. J. Ehrlich, J. Maya, and R. M. Osgood, Jr., *Appl. Phys. Lett.* 33, 931 (1978), DDC AD-A069320/0; D. J. Ehrlich and R. M. Osgood, Jr., *Appl. Phys. Lett.* 34, 655 (1979), DDC AD-A073882; T. F. Deutsch, D. J. Ehrlich, and R. M. Osgood, Jr., *Opt. Lett.* 4, 378 (1979).
19. G. C. Turk, J. C. Travis, J. R. DeVoe, and T. C. O'Haver, *Anal. Chem.* 50, 817 (1978).
20. T. F. Deutsch, D. J. Ehrlich, and R. M. Osgood, Jr., *Appl. Phys. Lett.* 35, 175 (1979), DDC AD-A076463.
21. L. L. Sveshnikova, V. I. Donin, and S. M. Repinskii, *Sov. Tech. Phys. Lett.* 3, 223 (1977); J. M. Beterov, C. P. Chebotaev, N. I. Yurshina, and B. Ya. Yurshin, *Sov. J. Quantum. Electron.* 8, 1310 (1978).
22. F. Kuhn-Kuhnenfeld, *J. Electrochem. Soc.* 119, 1063 (1972); Zh. I. Alferov, D. N. Goryachev, S. A. Gurevich, M. N. Mizerov, E. L. Portnoi, and B. S. Ryvkin, *Sov. Phys. Tech. Phys.* 21, 857 (1976).
23. For InP see, for example, R. C. Clarke, D. S. Robertson, and A. W. Vere, *J. Mater. Sci.* 8, 1349 (1973).
24. D. J. Ehrlich, T. F. Deutsch, and R. M. Osgood, Jr., unpublished experiment.
25. Z. L. Liao, N. L. DeMeo, J. P. Donnelly, D. E. Mull, R. Bradbury, and J. P. Lorenzo, Materials Research Society Symposium A, Cambridge, Massachusetts, 27-30 November 1979 (Proceedings to be published by Academic Press).
26. G. C. Messenger, *IRE Trans. Microwave Theory Tech.* MTT-5, 62 (1957).
27. S. Weinreb and A. R. Kerr, *IEEE J. Solid-State Circuits* SC-8, 58 (1973).

III. MATERIALS RESEARCH

A. DIFFUSION OF Zn AND Cd IN InP

The elements Zn and Cd are the acceptor impurities commonly used for diffusion from the vapor phase in the fabrication of electrooptical devices employing InP and GaInAsP alloys. Thus, high-performance GaInAsP/InP devices such as diode lasers and avalanche photodiodes have been fabricated using Zn and Cd diffusion, respectively. At a given temperature Zn diffuses much faster than Cd, and Zn diffusion can lead to the formation of irregular diffusion fronts, so that it has been suggested that Cd should be preferred to Zn as the acceptor diffusant for device fabrication. In order to make a comparative evaluation of the two elements for this purpose, we have carried out a series of experiments on their diffusion in InP. In these experiments, single-crystal n-InP substrates with carrier concentrations of 10^{16} to 10^{18} cm⁻³ were partially masked with SiO₂, Si₃N₄, or phosphosilicate glass (PSG), sealed in evacuated fused-silica ampoules with weighed amounts of ZnP₂ or CdP₂, and heated in a resistance furnace. The depth of the p-n junction formed by diffusion was then determined by cleaving and etching. For Cd-diffusion experiments at temperatures above about 550°C, it was necessary to place a small amount of red P in the ampoule to prevent thermal etching of the substrate due to P evaporation. Additional P was not required in the Zn-diffusion experiments even at 650°C.

When Zn was diffused at 650°C to form a p-n junction several micrometers deep, the diffusion front was found to be quite flat over most of the sample, but a few defects were observed at the junction. One such defect is seen in Fig. III-1, which is an optical micrograph of a cleaved cross section showing a junction about 4.5 μm deep produced by Zn diffusion at 650°C for 5 min. into a Sn-doped substrate with background carrier concentration of about 10^{18} cm⁻³. Defects of this type were formed much more often in substrates with such high carrier concentrations than in those with low carrier concentrations ($\sim 10^{16}$ cm⁻³). No defects were observed for diffusions performed at 500°C or below. The quantitative results of the experiments are shown in Fig. III-2, where the junction depth L is plotted against the square root of time $t^{1/2}$ for Zn diffusions at 500° and 650°C into InP substrates with carrier concentration of $(1 \text{ to } 2) \times 10^{16}$, 3×10^{17} , and $(1 \text{ to } 2) \times 10^{18}$ cm⁻³. The data are consistent with a linear dependence of L on $t^{1/2}$. For a given diffusion time and temperature, L is not very sensitive to the substrate carrier concentration.

The diffusion of Cd in InP at 500°C is so slow that no junction was detected even after heating for 40 min. at this temperature. Diffusion at 600°C for about 100 min. yielded a junction depth of about 2 μm, provided that no excess P was added to the ampoule, but in this case the exposed InP surface was severely attacked due to P evaporation. Adding P to prevent thermal etching caused a marked reduction in the rate of diffusion, as reported by Tien and Miller.¹ The diffusion rate reached a limiting value for P/CdP₂ weight ratios of 5 or higher. For such ratios the junction depth was reduced by almost an order of magnitude, so that it would be necessary to employ diffusion temperatures significantly above 600°C in order to obtain useful junction depths in a reasonable time. Severe cracking of passivating coatings occurs at such high temperatures, however, making it impossible to carry out the selective-area diffusion required for device fabrication.

To compare the performance of InP diodes prepared by Zn and Cd diffusion, the dark current under reverse bias has been measured for devices 100 μm in diameter with a p-n junction

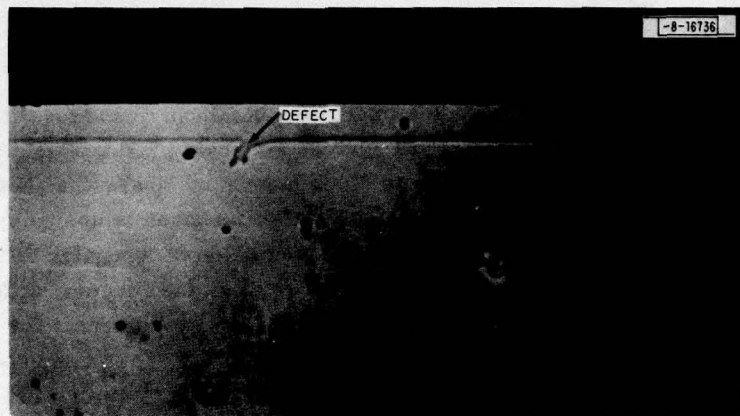


Fig. III-1. Cleaved cross section through InP sample, showing p-n junction formed at depth of $4.5\text{ }\mu\text{m}$ by Zn diffusion at 650°C for 5 min. from ZnP_2 source.

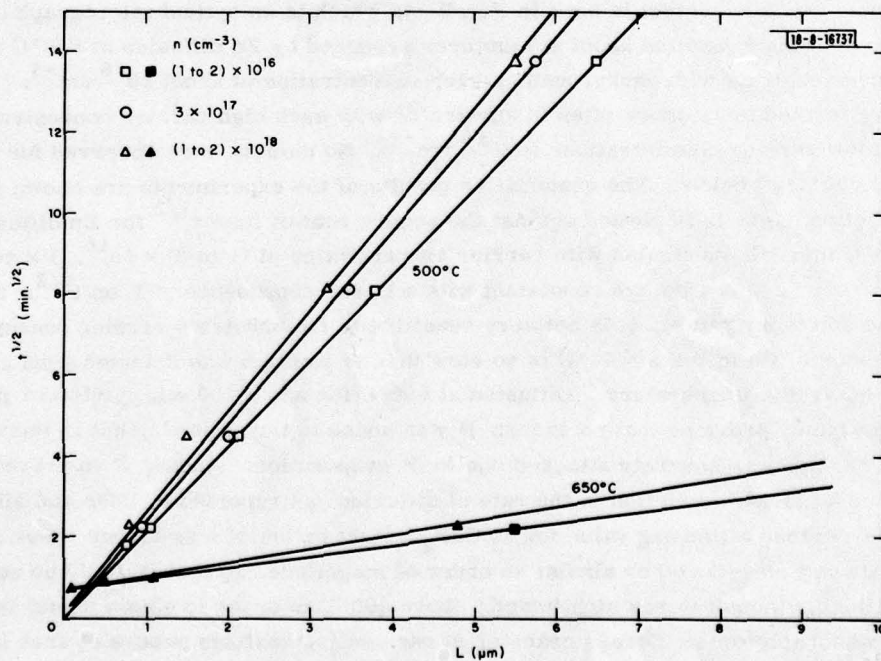


Fig. III-2. P-n junction depth L as a function of square root of diffusion time $t^{1/2}$ for Zn diffusion into n-InP at 500° and 650°C using ZnP_2 source.

depth of about 2 μm obtained by diffusion of Zn (20 min. at 500°C) or Cd (100 min. at 600°C, without excess P) into nominally undoped n-InP layers (carrier concentration about 10^{17} cm^{-3}) grown by liquid-phase epitaxy on (100)-oriented substrates. Both types of diodes have the same breakdown voltage ($V_B = 23 \text{ V}$ at 1 μA) and similar leakage currents (2 to 10 nA at 0.5 V_B). The leakage actually depends more strongly on the type of passivating layer than on the acceptor diffusant, with the lowest leakage being obtained for devices from which the passivating layer was removed after diffusion. Since the Zn- and Cd-diffused diodes have comparable characteristics, and Zn diffusion can be readily controlled at temperatures of 500°C or less, making it possible to avoid the difficulties associated with Cd diffusion because of the high temperatures required to obtain practical junction depths, it is advantageous to use Zn rather than Cd as the acceptor diffusant for the fabrication of InP devices.

J. J. Hsieh

B. SCANNED LASER CRYSTALLIZATION OF AMORPHOUS Ge FILMS

We recently reported² the formulation of a theoretical model for the scanned laser crystallization of amorphous semiconductor films. By means of calculations based on this model, we were able to account for a number of unusual phenomena that we observed in an investigation of the laser crystallization of amorphous Ge (a-Ge) films. We have now extended this investigation by making detailed observations of the microstructure of laser-crystallized Ge films as a function of the substrate temperature maintained before irradiation. Regions of well-aligned grains with lateral dimensions up to 2 to 3 \times 100 μm have been obtained, and we believe that, by optimizing the experimental parameters, it may be possible to prepare even larger grained or perhaps single-crystal semiconductor sheets by scanning amorphous films with energy beams of high aspect ratio.

The present investigation, which extends our earlier studies of the laser crystallization of amorphous Si (Ref. 3) and GaAs (Ref. 4), was motivated by our recent development of shallow-homojunction solar cells with conversion efficiencies exceeding 20 percent at AM1 that are prepared by chemical vapor deposition of GaAs active layers on single-crystal Ge substrates.⁵ Our objective is to use laser crystallization to obtain large-grained Ge sheets that can provide low-cost substrates for efficient GaAs cells.

Our crystallization system⁴ utilizes a CW Nd:YAG laser beam focused to a slit image with power density that is uniform to ± 3 percent over a central area about 50 μm by 1.5 mm. The samples are placed in an Ar/H₂ atmosphere on a resistively heated platform that permits them to be scanned under the laser beam in the focal plane and normal to the long axis of the slit image. The a-Ge films were deposited by either electron-beam evaporation, RF sputtering, or ion-beam sputtering on Mo, graphite, or fused-silica substrates.

In initial experiments on Ge films 2 to 4 μm thick on Mo and graphite substrates, the platform was heated to maintain the temperature of the film before laser irradiation (T_b) at 400° to 500°C. Once crystallization was initiated by momentary irradiation at a single point, the transformation was found to be self-sustaining, with the crystallization front rapidly propagating radially outward from the irradiated spot. Films as large as 2.5 \times 2.5 cm were entirely crystallized in this manner. (Self-sustaining transformation of a-Ge, initiated by means other than laser irradiation, had been reported previously.⁶) At lower values of T_b , self-sustaining crystallization did not occur, but laser scanning yielded areas of elongated, well-aligned grains. The surface of the scanned films remained smooth, regardless of T_b . The maximum temperature reached by the film during scanning, as estimated from its color, was about 700°C – far below the melting point of Ge (937°C).

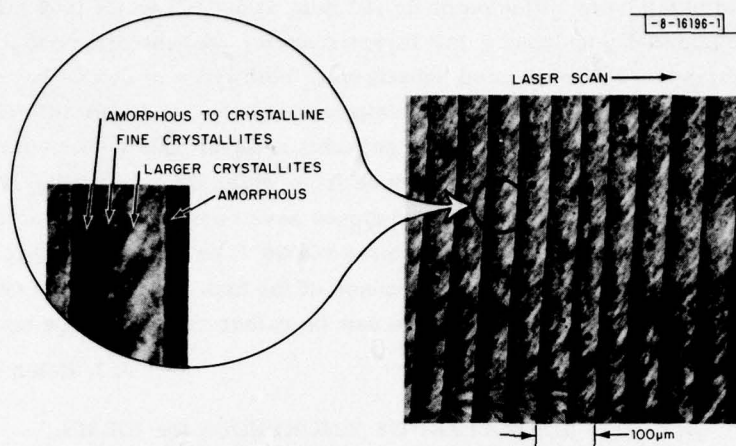


Fig. III-3. Optical transmission micrograph of laser-crystallized Ge film showing periodic structural features. Inset: expanded view illustrating four different microstructure regions.

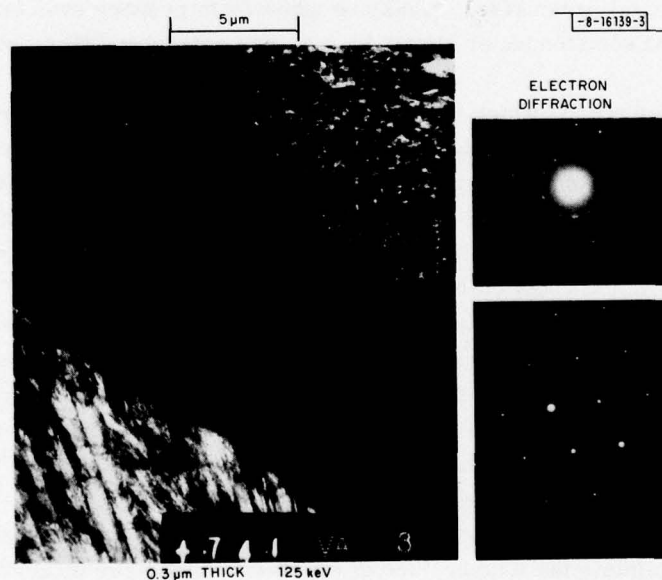


Fig. III-4. Left: bright-field transmission electron micrograph of laser-crystallized Ge film, illustrating four different microstructure regions. Right: transmission electron-diffraction patterns for fine- and large-grained regions (upper and lower, respectively).

We then performed a series of experiments on films about $0.3\text{ }\mu\text{m}$ thick deposited by electron-beam evaporation on 1-mm-thick fused-silica substrates. (Films deposited by RF sputtering or ion-beam sputtering have been found to exhibit similar crystallization characteristics.) The power density of the central area of the laser image was kept at about 5 kW/cm^2 , and the scan rate at 0.5 cm/sec . The background temperature T_b was varied from room temperature to 500°C . For T_b equal to room temperature, the films exhibit periodic structural features after laser scanning. Within each film the spatial period initially increases, but after several periods it reaches a steady-state value of about $50\text{ }\mu\text{m}$. The right side of Fig. III-3 shows an optical transmission micrograph of one such film, obtained with visible radiation from a xenon lamp, illustrating the steady-state periodic features. The dark areas in the micrograph are regions of untransformed a-Ge, which for the film thickness used is almost opaque to visible and near-infrared radiation, while the bright areas are regions of crystalline Ge, which has significant transmission in the red and near-infrared. Each periodic feature consists of four different regions, as shown on the left side of Fig. III-3: first a narrow amorphous region, then another region containing a mixture of amorphous material and fine grains, next a broad region of fine crystallites, and finally another broad region of much larger, elongated crystallites (with dimensions of about $1\text{ to }2 \times 20\text{ }\mu\text{m}$), aligned parallel to each other but at an angle of about 55° to the laser scan direction. In the films that we have examined in detail, the large crystallites within each periodic feature form a roughly chevron-like pattern, with the two halves of the pattern symmetrical about an axis that is parallel to the scan direction and located near the center of the laser slit image. Thus, the angles between the long axes of the crystallites and the scan direction are similar in magnitude but of opposite sense for the two halves of the pattern. (For the periodic features shown in Fig. III-3, the symmetry axis lies close to or just below the bottom of the micrograph, so that only half the chevron pattern can be seen.)

The optical microscopy results have been confirmed by transmission electron microscopy (TEM) using 125-keV electrons. The TEM samples were removed from their substrates by using hydrofluoric acid to partially dissolve the fused silica. The left side of Fig. III-4 is the TEM bright-field micrograph of a portion of a film that was laser-scanned with T_b equal to room temperature, like the film of Fig. III-3. The micrograph shows the same sequence of regions found by optical microscopy: amorphous (the dark area), amorphous-plus-crystalline, fine-grained, and large-grained. The fine-grained region yields transmission electron-diffraction patterns like the one shown at the upper right of Fig. III-4, with the rings typical of polycrystalline material. Within this region, the grain size gradually increases until it reaches about $0.3\text{ }\mu\text{m}$, the thickness of the film, then increases abruptly to give the large, well-aligned crystallites of the final region, which are clearly visible as ribbon-like structures in the lower left corner of the micrograph (which shows the end of the preceding periodic feature). It has been demonstrated by bright- and dark-field TEM that each of these structures is a single grain, and they yield characteristic single-crystal transmission electron diffraction patterns, as illustrated at the lower right of Fig. III-4. These patterns indicate that the crystallites are oriented with the normal to the plane of the substrate in a $\langle 110 \rangle$ direction, their long axis in a $\langle 001 \rangle$ direction, and a $\langle 112 \rangle$ direction parallel to the long axis of the laser slit image. These orientations are clearly characteristic of the solid-phase growth process studied in this investigation, since they are the same for the large crystallites throughout the film, even though these crystallites in successive periodic features are separated by regions of amorphous and randomly oriented, fine-grained material.

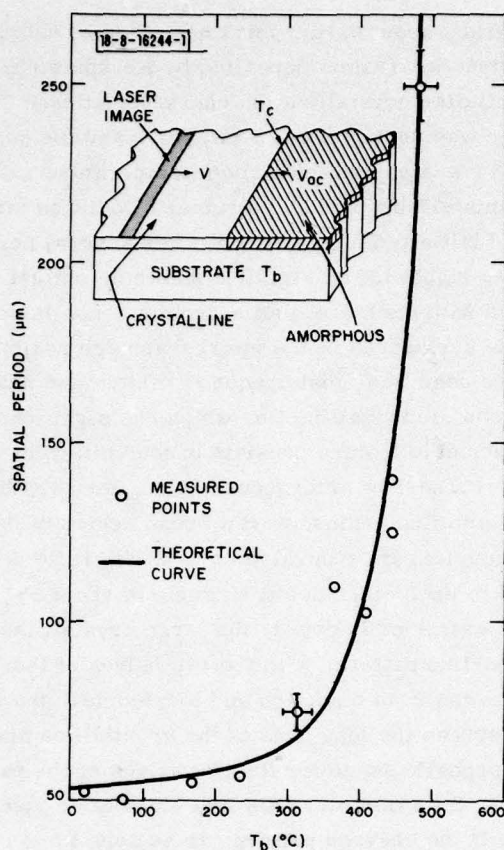


Fig. III-5. Experimental points and theoretical curve for spatial period of periodic structural features of laser-crystallized Ge films as a function of background temperature T_b . Inset: schematic diagram of scanned laser crystallization of amorphous film.

When the experiments were repeated using values of background temperature T_b that were above room temperature but not high enough to result in self-sustaining crystallization, the scanned films exhibited periodic structural features like those described above. As shown by the experimental points plotted in Fig. III-5, with increasing T_b the spatial period of these features increases — slowly at first but quite abruptly beginning at $T_b \sim 350^\circ\text{C}$. For $T_b = 475^\circ\text{C}$, not far below the value (T_r) required for runaway motion of the crystallization front, the spatial period is $250\text{ }\mu\text{m}$. The increase in spatial period is accompanied by a marked increase in the size of the large, aligned crystallites, which reached 2 to $3 \times 100\text{ }\mu\text{m}$ for $T_b = 475^\circ\text{C}$.

The periodic structural features formed as a result of laser scanning, the dependence of their spatial period on T_b , and the occurrence of self-sustaining crystallization at values of T_b greater than the runaway temperature T_r can all be explained by means of the theoretical treatment we reported previously.² The inset of Fig. III-5 is a schematic diagram showing the geometry considered. The film is deposited on a thick substrate of poor thermal conductivity that is heated to T_b , and the laser image is scanned from left to right at velocity v . The approximation is made that the amorphous-crystalline (a-c) transformation occurs instantaneously when the film reaches a critical temperature T_c . The a-c boundary (crystallization front) therefore coincides with a T_c isotherm, and the motion of the boundary can be found by calculating the motion of this isotherm. The calculations are accomplished by numerical solution of an integral equation derived from the model, which takes account of the fact that the solid-phase transformation of the film from the metastable amorphous form to the stable crystalline

form is accompanied by the liberation of latent heat. If T_b is less than T_r , according to the calculations the a-c boundary moves in a series of rapid jumps between rest positions even though the laser image is scanned at constant velocity. The periodic structural features of the laser-scanned films are due to this periodic motion of the boundary, and the spatial period of these features is the distance between successive rest positions. If T_b exceeds T_r , the continuing release of latent heat is sufficient to maintain the propagation of the T_c isotherm indefinitely, resulting in self-sustaining crystallization.

To test the model, we have calculated the distance between successive boundary rest positions as a function of T_b . The results are shown by the theoretical curve in Fig. III-5, which is in good agreement with the experimental data for the spatial period in the films. In carrying out the calculations, the values of the parameters T_r , T_c , and effective latent heat fL supplied to the film (where L is the actual latent heat) were adjusted to give the best fit to the data. The optimized values are $T_r = 530^\circ\text{C}$, $T_c = 685^\circ\text{C}$, and $fL = 14 \text{ cal/g}$.

In conclusion, large-grained Ge films containing well-aligned crystallites with lateral dimensions up to 2 to $3 \times 100 \mu\text{m}$ have been obtained by scanning amorphous films on fused-silica substrates (without surface-relief structures⁷) with the slit image of a CW Nd:YAG laser. Both the formation of periodic structural features and self-sustaining crystallization have been explained in terms of a theoretical model that takes account of the liberation of latent heat, although the detailed microstructure of the scanned films, particularly the presence of untransformed regions, has not yet been explained. Based on our observations and the theoretical model, we believe that there is a good possibility of preparing even larger-grained or perhaps single-crystal semiconductor sheets by scanning amorphous films with laser or other energy beams of high aspect ratio in a manner that achieves continuous, controlled motion of the crystallization front, rather than either periodic or runaway motion.

J. C. C. Fan R. P. Gale
H. J. Zeiger R. L. Chapman

C. PREPARATION OF GaAs SOLAR CELLS BY MOLECULAR-BEAM EPITAXY

Solar cells prepared from GaAs are the subject of strong current interest because of their high conversion efficiencies^{8,9} and resistance to space radiation.^{10,11} All such cells reported so far have utilized GaAs layers grown by either chemical vapor deposition (CVD) or liquid-phase epitaxy (LPE). We have now used molecular-beam epitaxy (MBE) to obtain GaAs solar cells with conversion efficiencies up to 16 percent at AM1. These are the first efficient MBE solar cells of any type to be reported.

MBE can be expected to offer a number of advantages as a technique for the preparation of solar cells, particularly thin-film cells on low-cost substrates. The deposition temperatures required to obtain high-quality layers are lower for MBE than for CVD or LPE, and the use of lower temperatures can reduce detrimental diffusion effects. Since MBE is a vacuum-deposition technique, there is generally less interaction between the deposition species and the substrate than in the case of CVD or LPE. Furthermore, MBE is especially suited to the preparation of thin-film cells because layer thicknesses and doping profiles can be accurately reproduced from run-to-run. In addition, unlike CVD and LPE, MBE permits *in situ* metallization, a process which may prove useful in solar-cell fabrication. In view of these potential advantages, we have initiated the application of MBE to the preparation of solar cells by using this technique to obtain efficient cells on single-crystal GaAs substrates.

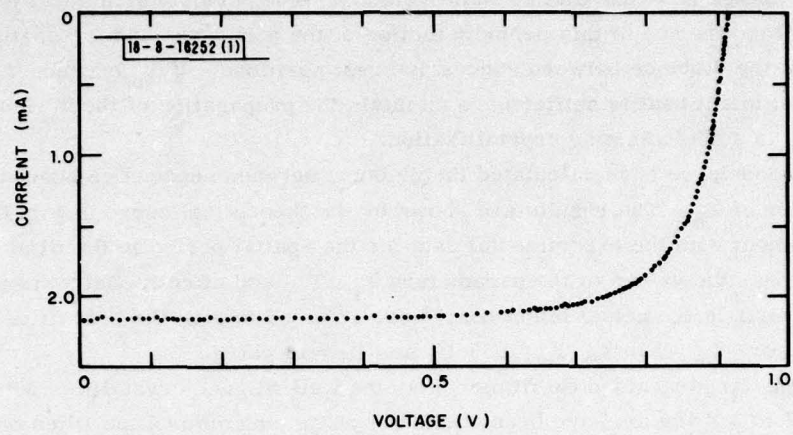


Fig. III-6. Photocurrent as a function of voltage for an MBE GaAs cell with 16-percent conversion efficiency at AM1.

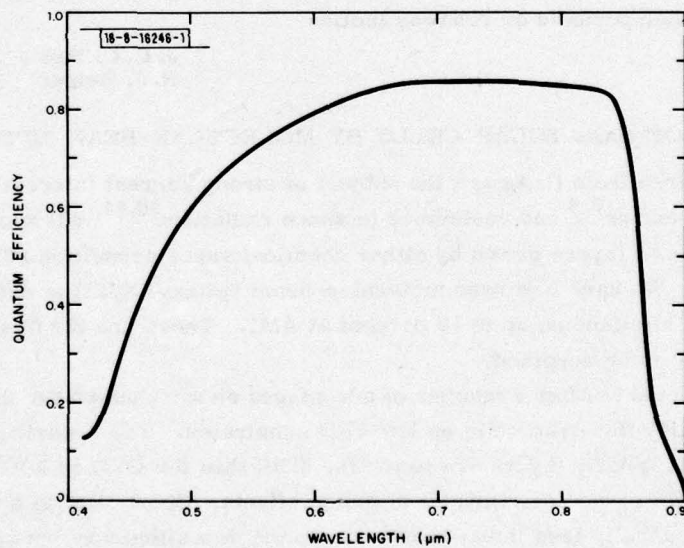


Fig. III-7. Quantum efficiency as a function of wavelength for cell of Fig. III-6.

We previously developed GaAs shallow-homojunction solar cells, with conversion efficiencies as high as 20 percent at AM1, that incorporate GaAs layers grown by CVD on either GaAs (Ref. 9) or Ge (Ref. 5) single-crystal substrates. These devices employ an $n^+/p/p^+$ structure, without a GaAlAs window, in which surface recombination losses are reduced because the n^+ -layer is so thin that most of the photogenerated carriers are created in the p -layer below the junction. The new cells use the same shallow-homojunction $n^+/p/p^+$ structure, but the n^+ , p^- , and p^+ -layers are grown by MBE.

In preparing the solar cells, an MBE system similar to those described in the literature^{12,13} was used to deposit the three successive GaAs layers (p^+ : Be-doped, $1 \times 10^{18} \text{ cm}^{-3}$, $1.5 \mu\text{m}$ thick; p : Be-doped, $1 \times 10^{17} \text{ cm}^{-3}$, $4.5 \mu\text{m}$ thick; n^+ : Sn-doped, $5 \times 10^{18} \text{ cm}^{-3}$, $0.15 \mu\text{m}$ thick) on p^+ GaAs substrates (Zn-doped, $1 \times 10^{18} \text{ cm}^{-3}$) oriented 2° off (100) toward (110). The substrates were ground and then chem-mechanically polished on a polyurethane felt pad with a solution prepared by dissolving 40 g Na_2CO_3 in one liter of 1:1 Clorox and H_2O . Just prior to mounting in the system, they were etched for 2 min. in a 5:1:1 solution of H_2SO_4 , H_2O_2 , and H_2O at 25°C and quickly rinsed in high-purity H_2O . Immediately before exposure to the molecular beam from the deposition sources, the substrates were heated to 600°C for 1 min. to remove surface oxides. The temperature was then reduced and maintained at 580°C during growth. The deposition sources were high-purity Ga, As, Be, and Sn contained in resistance-heated pyrolytic boron nitride furnaces. The source temperatures were adjusted to give an As_4/Ga concentration ratio of 5 in the molecular beam, and a GaAs growth rate of $1 \mu\text{m}/\text{h}$. During deposition, the system was backfilled with H_2 at a partial pressure of 10^{-6} Torr (N_2 equivalent) in order to reduce oxygen contamination of the growing layers.¹⁴

The fabrication techniques used for the MBE cells were similar to those used for CVD cells.^{5,9} No vacuum-processing procedures were employed. The back contact to the p^+ -substrate was electroplated Au, and the front contact bar and fingers (defined by photolithography) were electroplated Sn. The thickness of the n^+ -layer was reduced from its initial value of about 1500 \AA to about 700 \AA by alternating anodic oxidation and etching steps. The last of these steps was an anodization that formed an oxide layer about 850 \AA thick to serve as an antireflection coating. The cell area was defined by conventional mesa techniques. Ten cells were made which ranged in surface area from 0.45 to 9.5 mm^2 .

In making conversion efficiency measurements, a high-pressure Xe lamp with a water filter was used as a simulated AM1 source. Using a NASA-measured GaAs solar cell as a reference, the source was adjusted to provide an incident intensity of $100 \text{ mW}/\text{cm}^2$. The measurements were made at an ambient temperature of 25°C . Figure III-6 shows the current-voltage curve for the most efficient cell, which also has the largest area. The open-circuit voltage V_{oc} is 0.92 V , the short-circuit current density J_{sc} is $23 \text{ mA}/\text{cm}^2$ (not corrected for the contact finger area, which was less than 5 percent of the total), and the fill factor is 0.76, giving a measured efficiency of about 16 percent. Five other cells have efficiencies ranging from 8 to 15 percent, while four have efficiencies lower than 8 percent.

The quantum efficiency of the best cell is plotted as a function of wavelength in Fig. III-7. The quantum efficiency values are only about 10-percent lower than those of our best CVD cells. Figure III-8 shows the dependence of J_{sc} (corrected for the contact finger area) on V_{oc} for the best cell, as obtained by a series of measurements at different illumination levels up to about 10 suns. The whole series was taken in about 10 sec to minimize heating at the high illuminations,

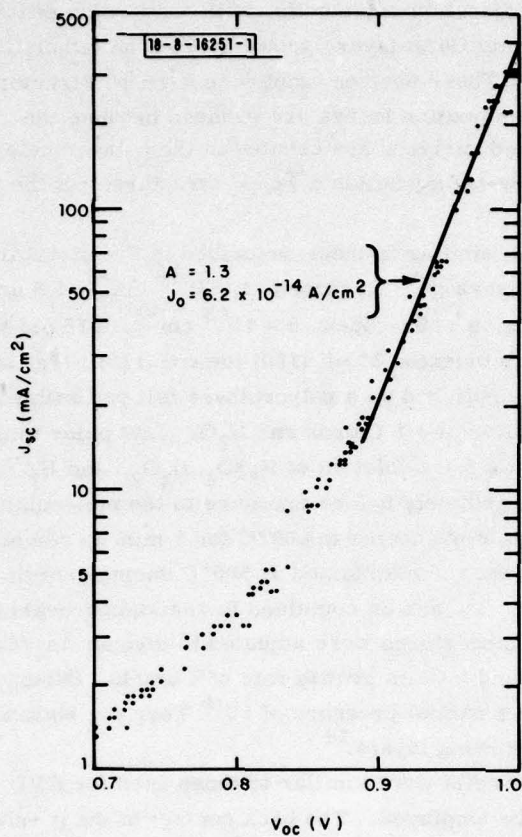


Fig. III-8. Short-circuit current density J_{sc} as a function of open-circuit voltage V_{oc} at different illumination levels for cell of Fig. III-6.

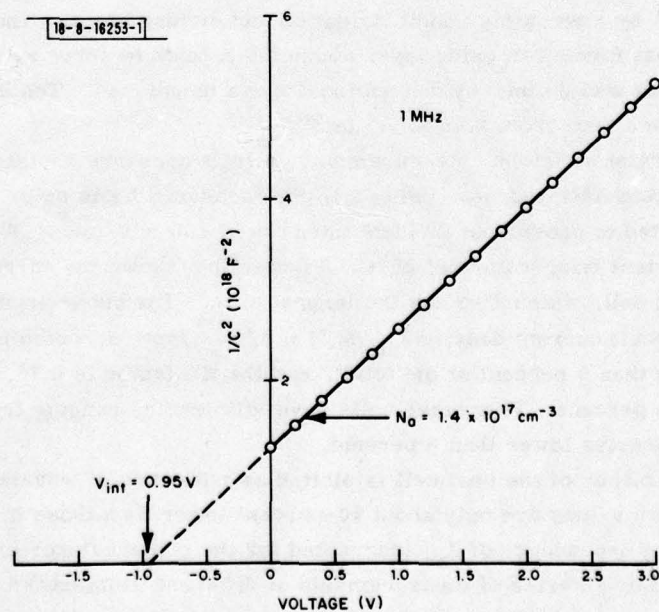


Fig. III-9. Plot of $1/C^2$ (where C is dark capacitance) as a function of reverse-biased voltage (V) for cell of Fig. III-6.

with the cell mounted on a copper block thermoelectrically controlled at 25°C. From the relationship¹⁵ $V_{oc} = A(kT/q) \ln [(J_{sc}/J_0) + 1]$, where k is Boltzmann's constant, T is the absolute temperature, and q is the electron charge, the diode factor A is 1.3 and the saturation current density J_0 is 6.2×10^{-14} A/cm². Although these values indicate good material quality, they are higher than those for our best CVD cells,¹⁶ resulting in the slightly lower V_{oc} and fill factor of the MBE cell.

A plot of $1/C^2$ (where C is the dark capacitance) vs voltage for the best cell at room temperature is shown in Fig. III-9. The straight line obtained indicates that the p-n junction is very abrupt, a characteristic feature of MBE growth. Since the intercept voltage V_{int} is ~0.95 V and the barrier voltage $V_b \approx (V_{int} + 2kT/q)$, V_b is ~1.0 V. The carrier concentration determined from the slope of the straight line is 1.4×10^{17} cm⁻³, which corresponds well with the Be concentration in the p-GaAs layer calculated from the deposition conditions.

Since the MBE GaAs solar cells described here are at an early stage of development, optimizing the MBE growth process should lead to a significant improvement in performance. Because MBE growth permits the precise control of layer thickness and carrier concentration, it should be possible to develop MBE GaAs solar cells with conversion efficiencies approaching the theoretical limits.

J. C. C. Fan R. L. Chapman
A. R. Calawa G. W. Turner

REFERENCES

1. P.K. Tien and B.I. Miller, Appl. Phys. Lett. 34, 701 (1979).
2. Solid State Research Report, Lincoln Laboratory, M.I.T. (1979:2), pp. 41-45, DDC AD-A078676.
3. J. C. C. Fan and H. J. Zeiger, Appl. Phys. Lett. 27, 224 (1975), DDC AD-A016696/7.
4. J. C. C. Fan, H. J. Zeiger, and P. M. Zavracky, Proc. Natl. Workshop on Low-Cost Polycrystalline Silicon Solar Cells, Dallas, Texas, 18-19 May 1976, p. 89.
5. C. O. Bozler, J. C. C. Fan, and R. W. McClelland, Chapter 5 in Gallium Arsenide and Related Compounds (St. Louis) 1978 (The Institute of Physics, London, 1979), p. 429, DDC AD-A072370.
6. T. Takamori, R. Messier, and R. Roy. Appl. Phys. Lett. 20, 201 (1972); A. Mineo, A. Matsuda, T. Kurosu, and M. Kikuchi, Solid State Commun. 13, 1307 (1973).
7. M. W. Geis, D. C. Flanders, and H. I. Smith, Appl. Phys. Lett. 35, 71 (1979), DDC AD-A076745.
8. J. M. Woodall and H. J. Hovel, Appl. Phys. Lett. 30, 492 (1977).
9. J. C. C. Fan, C. O. Bozler, and R. L. Chapman, Appl. Phys. Lett. 32, 390 (1978), DDC AD-A058281/7.
10. G. H. Waler, C. E. Byvik, E. J. Conway, J. H. Heinbockel, and M. J. Doviak, J. Electrochem. Soc. 125, 2034 (1978).
11. J. C. C. Fan, R. L. Chapman, C. O. Bozler, and P. J. Drevinsky, Appl. Phys. Lett. (to be published).
12. A. Y. Cho and J. R. Arthur, in Progress in Solid State Chemistry, edited by G. A. Somorjai and J. O. McCaldin (Pergamon Press, Oxford, 1975), Vol. 10, p. 157.
13. L. L. Chang and R. Ludeke, in Epitaxial Growth, Part A, edited by J. W. Matthews (Academic Press, New York, 1975), p. 37.
14. A. R. Calawa, Appl. Phys. Lett. 33, 1020 (1978), DDC AD-A069916/5.
15. M. P. Godleski, C. R. Baraona, and H. W. Brandhorst, Jr., in Tenth IEEE Photovoltaic Specialists Conference - 1973 (IEEE, New York, 1973), p. 40.
16. J. C. C. Fan and C. O. Bozler, in Thirteenth IEEE Photovoltaic Specialists Conference - 1978 (IEEE, New York, 1978), p. 953.

IV. MICROELECTRONICS

A. FABRICATION AND MICROWAVE PERFORMANCE OF THE PERMEABLE BASE TRANSISTOR

The recently reported¹ permeable base transistor (PBT) has the potential for delivering gain at frequencies above those achieved by any other three-terminal device. The performance of the device has been evaluated by means of a theoretical model as well as through actual fabrication, and a maximum oscillation frequency of 17 GHz has been achieved. The fabrication of the devices combines two emerging technologies – x-ray lithography and crystal overgrowth of metal structures.

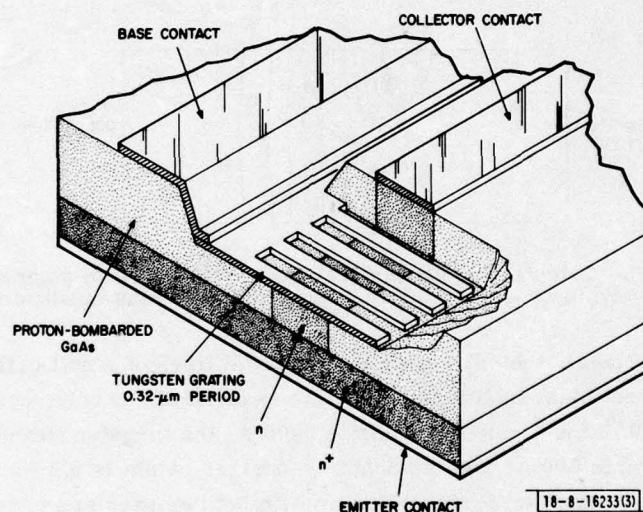


Fig. IV-1. Permeable base transistor. Grating, which is made from film of tungsten, is embedded in single crystal of GaAs. Electrons flow from emitter to collector through slits in metal layer.

Figure IV-1 is a three-dimensional drawing of the PBT, giving a cutaway view. The device consists of a 4-layer sandwich: the n^+ substrate, the n -type emitter layer, a patterned tungsten film which is the permeable metal base, and the n -type collector layer. Electrons flowing from the emitter region are constrained by the proton-bombarded GaAs to flow through the tungsten grating into the collector region. The metal-base contact is brought to the top surface adjacent to the collector contact. The tungsten layer forms a Schottky barrier with the GaAs, and the carrier concentration is adjusted so that the zero-bias depletion width of this barrier is about twice the width of the slits in the metal film.

1. Theory

Because the active portion of the device is periodic in one dimension and uniform in a second direction, the properties of the device can be obtained by analyzing the unit cell shown in cross section in Fig. IV-2(a-c). A two-dimensional computer simulation of the cell can be obtained by simultaneously solving Poisson's equation and the continuity equation with the proper boundary

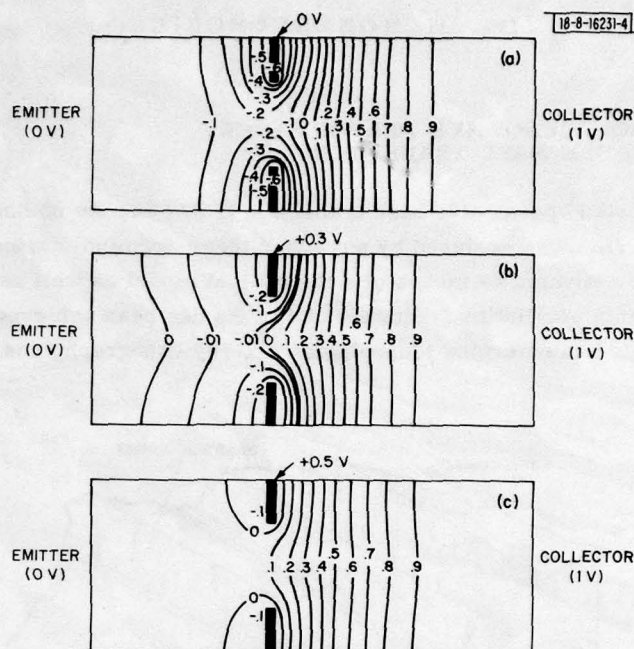


Fig. IV-2(a-c). Calculated equipotential lines in unit cell of permeable base transistor shown in cross section for three different bias conditions.

conditions. In Fig. IV-2(a-c), the calculated equipotential lines of a unit cell are given in cross section for three different bias conditions. For this example the carrier concentration of the semiconductor is $1 \times 10^{16} \text{ cm}^{-3}$, the slit width is 2000 \AA , the tungsten linewidth is 2000 \AA , the thickness of the tungsten is 200 \AA , and the Schottky-barrier height is 0.8 V .

In Fig. IV-2(a), 1 V is applied to the collector with both emitter and base at 0 V . As an electron travels from emitter to collector, it must move into a negative potential region which means that it must pass over an energy barrier. The barrier is lowest ($\sim 0.25 \text{ V}$) in the center of the opening between metal regions, and highest (0.6 V) at the metal semiconductor interface. The large barrier causes the current density at the collector contact to be small, approximately 5 A/cm^2 . If, however, the base is forward-biased to 0.3 V as in Fig. IV-2(b), the barrier is lowered and a current of 900 A/cm^2 flows at the collector contact. The model also shows that the current in the emitter can be visualized as having two opposing components as in a bipolar transistor, a drift and a diffusion current. The two components are very nearly equal as long as the barrier is large, resulting in net collector current which is very small. However, as the barrier is reduced by applying increasing forward bias to the base, both collector current and transconductance increase exponentially with applied bias. With even larger base bias as in Fig. IV-2(c), the barrier in the middle of the opening vanishes, and carrier accumulation develops, with the current beginning to be space-charge-limited. The common base current gain α remains greater than 0.99 for all base bias levels below 0.4 V because of the Schottky-barrier potential. When the base voltage reaches 0.5 V , α is reduced to 0.96 ; for higher base voltages, α decreases rapidly.

2. Fabrication and Performance

A tungsten grating having uniform lines and spaces (uniformity is required for good device performance) is fabricated on a single-crystal GaAs substrate using x-ray lithography and lift-off.²⁻⁴ A scanning electron micrograph of the tungsten metallization is shown in Fig. IV-3. The lines are joined together over the top third of their area by a continuous horizontal strip of tungsten. The regions of the metal lines not covered by the strip can be embedded in single-crystal GaAs using vapor phase epitaxial overgrowth. Nucleation and growth occur only on the GaAs and not on the tungsten, so that the single crystal grows laterally to cover the lines. Because of the size of the horizontal contact strip, epitaxial overgrowth cannot completely cover it.

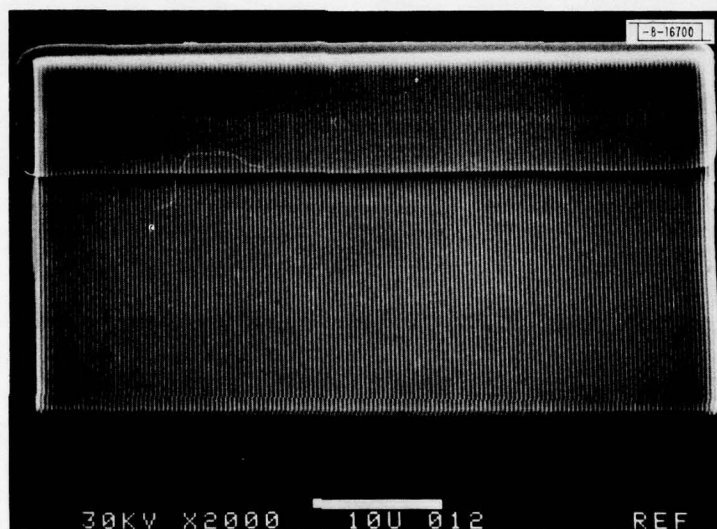


Fig. IV-3. Base metallization for single transistor with 152 slits in 300-Å tungsten film. Lines and spaces are both 1600 Å.

The collector ohmic contact is formed over the grating area using alloyed gold germanium, and the contact thickness is increased to 2.5 μm with plated gold to serve as the proton-bombardment mask. After proton bombardment, base and collector bonding pads are added, and the emitter contact, which was previously alloyed on the back of the substrate, is plated with gold. No critical alignments are required in the fabrication of the PBT.

The base-to-emitter characteristics of a completed PBT are identical to the base-to-collector characteristics. The common emitter characteristics from one device are given in Fig. IV-4. Both positive and negative bias were applied to the base, the fourth curve from the top being zero bias. Since the measured base capacitance is 5 times larger than was estimated from calculations, we believe that the carrier concentration in the device is higher than expected because of difficulties in control of the epitaxial growth. The large capacitance combined with a transconductance (obtained from Fig. IV-4), which is a factor of 5 lower than predicted by the computer model, limited the high-frequency performance of these devices. We believe that improvements in crystal-growth techniques and better wafer cleaning prior to overgrowth of the tungsten grating will lead to better control of the carrier concentration, which will result in lower capacitance and higher transconductance.

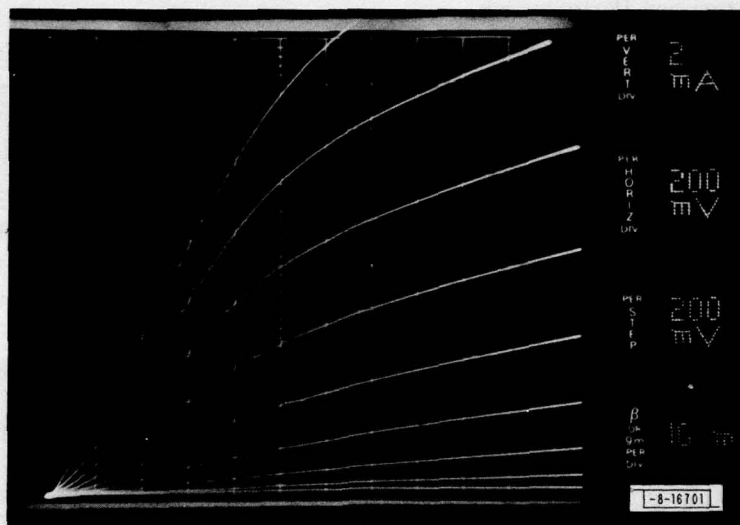


Fig. IV-4. Common emitter characteristics of permeable base transistor with both forward and reverse bias on base; zero-bias voltage curve is fourth from top.

The maximum frequency of oscillation for these devices was measured to be 17 GHz, and the maximum gain at 4 GHz was 13 dB. The noise figure at 4 GHz was 3.5 dB, with an associated gain of 9 dB. The design of these devices was not optimized for high-frequency performance, but was chosen as the simplest structure to prove the concept of the new transistor. There are, therefore, a number of parasitics limiting the performance which could be reduced (e.g., the base resistance which was measured to be 25 Ω but could be lowered to 5 Ω). The simulation of an optimized device assuming the same grating as used in these devices predicts a maximum frequency of oscillation of approximately 300 GHz. A numerical study of the effects of dimensional variations indicates that appropriate scaling to smaller dimensions should result in a maximum frequency of oscillation approaching 1000 GHz.

C. O. Bozler D. C. Flanders
G. D. Alley W. T. Lindley
R. A. Murphy

B. CHARGE-COUPLED DEVICES: IMAGERS

The CCD imager under development for the GEODSS (Ground Electro-Optical Deep Space Surveillance) Program is a 100- \times 400-element device for use in a ground-based satellite-surveillance system. The low-light-level performance of CCDs is of prime concern in this application, and the devices must be capable of low-noise operation. A noise-equivalent signal of less than 10 electrons has been obtained in the output circuitry of these imagers⁵ at a 400-kHz data rate. Another major noise source is dark current, and the goal is to reduce this noise below the output-circuit noise. We find that at chip temperatures of -60°C, the thermally generated charge is reduced below 10 electrons per well for an integration time of 0.25 sec.

Although dark current contains a temporal noise (shot noise), it is the spatial variation which is usually more significant in a device where charge is transferred by different paths to the output. The diagram of the imager (Fig. IV-5) shows how the photoelectrons are transferred

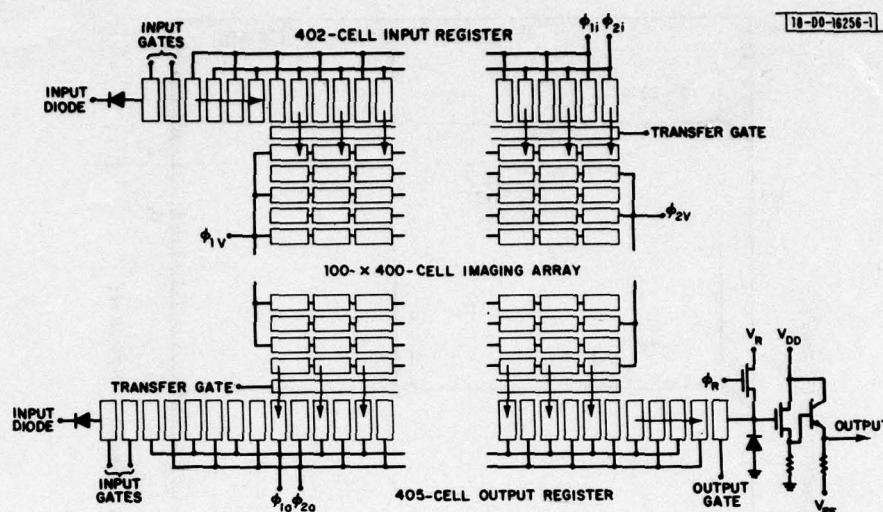


Fig. IV-5. Schematic of 100- x 400-cell CCD image sensor. Input register and electrical input to output register are used to evaluate transfer efficiency and were biased off for dark-current measurements.

down the 100 stages of each of the 400 columns to the serial output register. Since the device is a TDI (Time Delay and Integrate) device, the imaging array is clocked continuously, and the variation in average dark current of the 400 columns gives rise to the spatial noise. An integration time of 0.25 sec (time required for the 100 vertical transfers) and a maximum allowable dark charge per column of 10 electrons require the dark-current density to be $8 \times 10^{-13} \text{ A/cm}^2$ or less.

Measurements of the spatial variation of dark current were performed with devices mounted in a liquid nitrogen cooled chamber similar to one described in a previous report.⁶ The chamber had to be carefully shielded from ambient illumination to prevent erroneous measurements, especially for the long integration times at low temperatures. The device temperature is monitored by measuring the voltage drop across a forward-biased p-n junction at one edge of the chip.

The common method of measuring dark current in a CCD is to allow charge to build up to a measurable level in the wells and then to clock the charge to the output. However, the dark current has been observed to decrease as charge accumulates in a well, and this method would therefore underestimate the dark current. In the method chosen for our measurements, the device is clocked at its usual rate with the exception of the transfer gate at the bottom of the imaging cell array. In normal operation, this gate would be turned on once each period of the imaging array clocks to allow charge to be transferred to the output register. In the dark-current measurement this gate is kept off for N clock cycles, causing the charge to accumulate in the storage wells of the bottom row of ϕ_{2V} cells (see Fig. IV-5). After N periods of ϕ_{1V} and ϕ_{2V} , the charge in these cells will be N times the average charge for each column. Thus, with this method the dark charge in each cell is the same as it would be under normal clocking conditions for all except the bottom row of storage wells.

Dark-current data for an imager chip at three temperatures are shown in Fig. IV-6. The number of integration periods N of the vertical transport clocks was varied from 10 at 23°C to

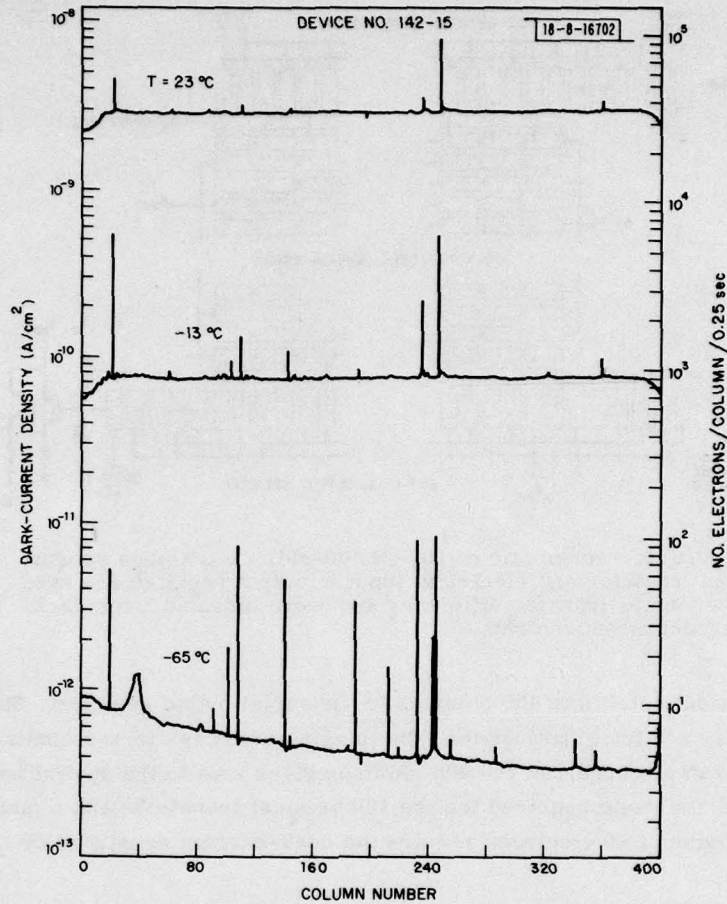


Fig. IV-6. Measurements of dark current per column at three temperatures.

10,000 at -65°C . The data are plotted both as the average dark-current density per column and as the number of dark-current electrons generated per column for a 0.25-sec integration time. The dark-current results can, in general, be described as spatially uniform or slowly varying except for "spikes" of excessive current generation. For some spikes the generation rate is so much in excess of the uniform background that, during the integration period, the dark current from that column overflows the transfer gate. The data for that column are then understated because of this "clipping" effect, and this is the case for some of the tallest spikes in Fig. IV-6. At the lowest temperature (-65°C), the background level has dropped below the target of 10 electrons per 0.25 sec. However, several spikes exceed this level. In the system application for these imagers such defects can be tolerated because of a redundant array of multiple chips on the focal plane, and because the data processing will be performed by a computer which will ignore the spikes.

The variation of dark-current density J_D (excluding the spikes) vs temperature is plotted in Fig. IV-7 for the device of Fig. IV-6 and an additional chip. For both devices, the room-temperature dark currents (1.4 and 2.9 nA/cm², respectively) are quite low and indicate excellent gettering of deep-level impurities. The theoretical expression which has been fitted to the

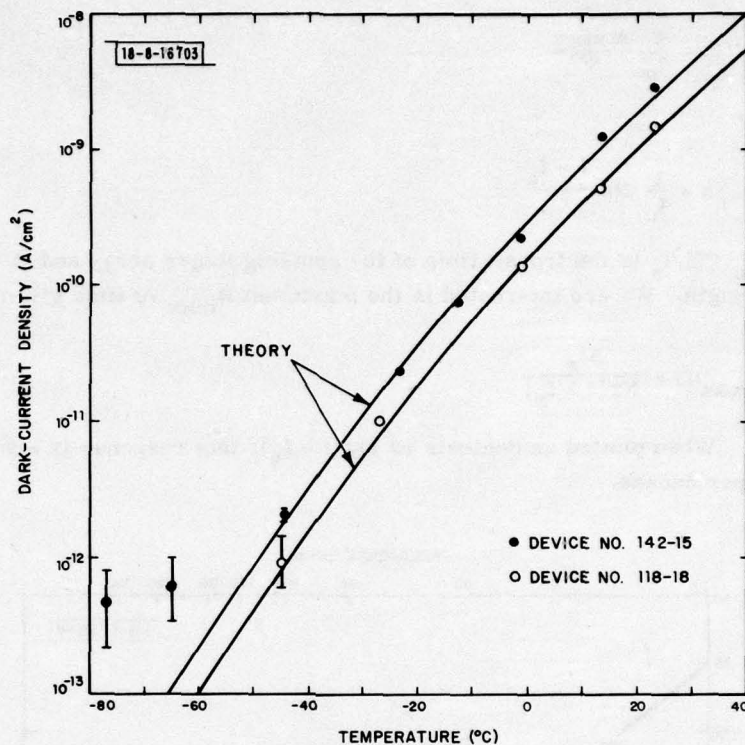


Fig. IV-7. Measured dark-current density excluding spikes vs temperature for device of Fig. IV-6 and additional device. Solid lines are based on theoretical expression which has been fitted to each set of data.

data predicts a temperature dependence of the depletion-layer generation current of the form $J_D \propto T^{3/2} \exp[-E_g(T)/2kT]$, where $E_g(T)$ is the energy gap.⁷ The fit between data and theory is good except for temperatures below about -50°C , at which point the dark current decreases at a slower rate than expected and appears to level off. The reason for this discrepancy is not presently understood.

B. E. Burke

C. CHARGE-COUPLED DEVICES: CCD PROGRAMMABLE SAW MATCHED FILTER

A silicon CCD has been integrated with a SAW delay line to produce a CCD programmable analog matched filter in which the filter function is controlled by the charge pattern clocked into the CCD.⁸ A spurious response at the output of this device has been identified and modeled. The response arises from the transducer-like detection of the SAW signal by the coupling finger array on the silicon chip, and experimental measurement of this nonprogrammable response as a function of frequency is in good agreement with the prediction of the model.

The magnitude of this detection was evaluated by exciting the SAW with a long tone-burst whose frequency f could be varied. The response to this input can be calculated by treating the coupling fingers as if they form a transducer with $N = 300$ periods. The output in time is the convolution of this tone burst with the impulse response of the coupling finger array, which is a tone burst at frequency f_s , the synchronous frequency of the array. The envelope of this convolution $R(f, t)$ oscillates sinusoidally in time and is given by

$$R(f, t) = \frac{t}{t_0} \frac{A \sin x}{x} \quad (\text{IV-1})$$

where

$$x = \frac{t}{t_0} N\pi \frac{f - f_s}{f_s} \quad (\text{IV-2})$$

for $t < t_0$, where $t_0 = N/f_s$ is the transit time of the coupling finger array and A is a measure of the coupling strength. We are interested in the maximum R_{\max} vs time given by

$$R_{\max}(f) = \frac{A f_s}{N\pi |f - f_s|} \quad (\text{IV-3})$$

for $|f - f_s| > f_s/N$. When plotted as decibels vs $\log(f - f_s)$, this response is a straight line with a slope of -20 dB per decade.

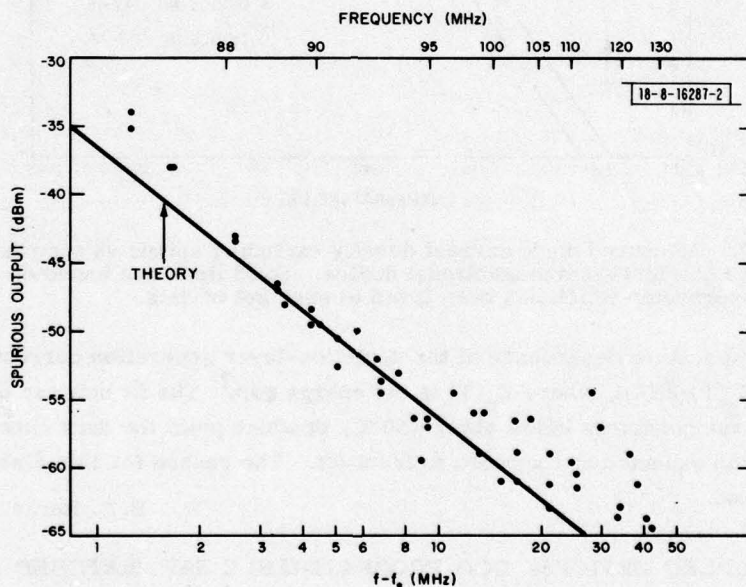


Fig. IV-8. Maximum spurious response of programmable matched filter. Input signal is 3.5- μ sec tone burst at indicated frequency with peak power of 27 dBm.

In Fig. IV-8, such a straight line is compared with our experimental results. The scatter in the measured response for $|f - f_s| > 5$ MHz is the result of interference between the transducer response and bulk waves (Ref. 8). This interference causes the net response to vary rapidly with frequency as the two spurious responses reinforce or cancel each other. This non-programmable transducer-like effect can be avoided by operating the filter at a frequency well away from f_s so that $|f - f_s|$ is greater than 5 MHz.

D. L. Smythe
R. W. Ralston
R. C. Williamson

D. CHARGE-COUPLED DEVICES: PROGRAMMABLE TRANSVERSAL FILTER

The structure developed by Lincoln Laboratory for high-speed, CCD programmable transversal filters (PTFs)⁹ uses a parallel-in, serial-out format in which the signal is introduced simultaneously at the inputs. The dynamic range of devices using this structure is limited by the variation in threshold voltage among the input gates, which results in different amounts of charge entering the device at the different inputs. This phenomenon is called fixed-pattern noise. A simple theoretical model has been developed for calculating the variation of threshold voltage of a CCD with either surface- or buried-channel input structures. The model emphasizes the sensitivities of threshold voltage to inhomogeneities in substrate doping or implant dosage for the surface- and buried-channel cases, respectively, and predicts a lower variation in threshold voltage for surface-channel inputs for our current PTF processing. Experimental results from the two types of devices processed in the same run are consistent with this model, showing a factor-of-6 reduction in threshold-voltage variation for surface-channel inputs compared with buried-channel inputs.

A one-dimensional model for a buried-channel CCD is shown in Fig. IV-9(a-b). The potentials in the various regions can be found from Poisson's equation. The position of electron potential energy minimum x_m corresponds to the potential $\phi(x_m)$, which is termed the channel potential. The channel potential is not only a function of the gate voltage V_g , but is dependent on the distribution of implanted donor atoms for the buried-channel case [$N_D(x)$], the substrate doping (N_A), and the gate oxide thickness (t_o).

A commonly used CCD input method is shown in Fig. IV-10. A reference voltage is applied to one of the input gates (G_1) and a corresponding reference channel potential $\phi_1(x_m)$ is set under G_1 . The threshold voltage of this device is the signal voltage which, when applied to G_2 , will cause the channel potential under the two gates to be equal [i.e., $\phi_1(x_m) = \phi_2(x_m)$]. For a CCD with a parallel input format, such as high-speed transversal filters, the parallel CCD channels have a signal applied in common to the G_2 gates and a common reference voltage applied to gates G_1 . For simplicity, let us consider the case when all the $\phi_1(x_m)$ are the same. The threshold variation of this device is the difference in signal voltages at which the potential equilibration $\phi_1(x_m) = \phi_2(x'_m)$ takes place for each of the parallel channel inputs.

For buried-channel inputs the calculated threshold variation ΔV_T due to 1-percent implant dose variation (i.e., $\Delta N_{Di} = 0.01 N_{Di}$) is shown in Fig. IV-11. The calculation is done for a p-type substrate with $N_A = 1 \times 10^{15} \text{ cm}^{-3}$. The effect due to the substrate variation is much smaller than that due to the implant dosage variation. The present PTF device uses a $1.5 \times 10^{12} \text{ cm}^{-2}$ phosphorous implant to form the n-type region. One can see from Fig. IV-11 that a $\Delta V_T = 120 \text{ mV}$ is anticipated for the 1-percent implant dose variation.

For a surface-channel device with a uniform substrate, the calculated threshold variation due to 1-percent nonuniformity in the substrate material is shown in Fig. IV-12. In the present PTF process for a surface-channel input, a boron offset implant results in a p-type substrate doping under the second input gate of about $1.6 \times 10^{16} \text{ cm}^{-3}$. Using the uniform substrate model as an approximation, one can see that a $\Delta V_T = 20 \text{ mV}$ is expected due to 1-percent inhomogeneity in the implant dosage.

Programmable transversal filters with 32 parallel CCD delay lines were used to evaluate experimentally threshold variations for surface- and buried-channel inputs. The results are shown in Fig. IV-13(a) and (b). In Fig. IV-13(a), the histogram of threshold variation for two

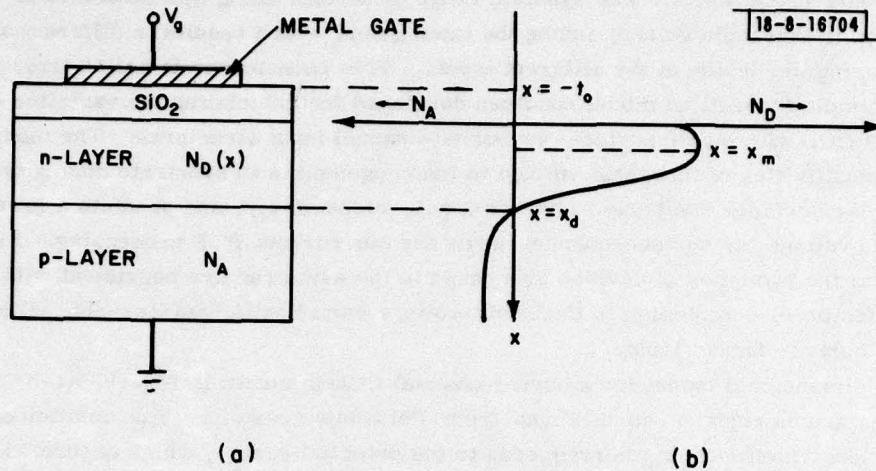


Fig. IV-9. (a) One-dimensional profile of buried-channel CCD (BCCD); (b) net donor and net acceptor concentration for BCCD.

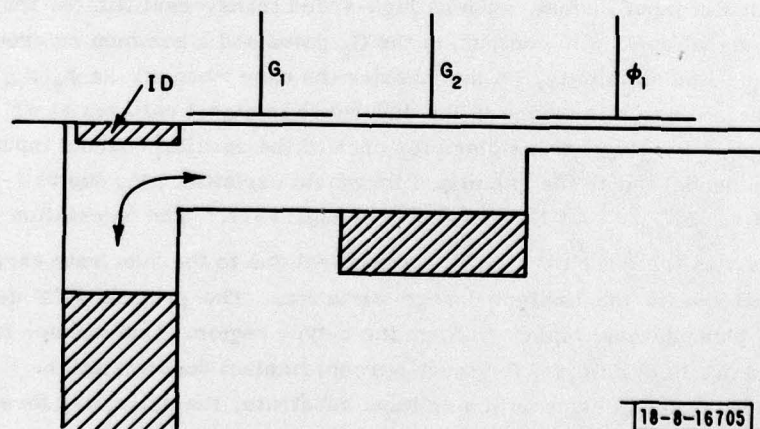


Fig. IV-10. A "fill and spill" CCD input.

Fig. IV-11. Threshold variation of buried-channel input CCD as a function of implanted donor density assuming a 1-percent non-uniformity in implant dosage.

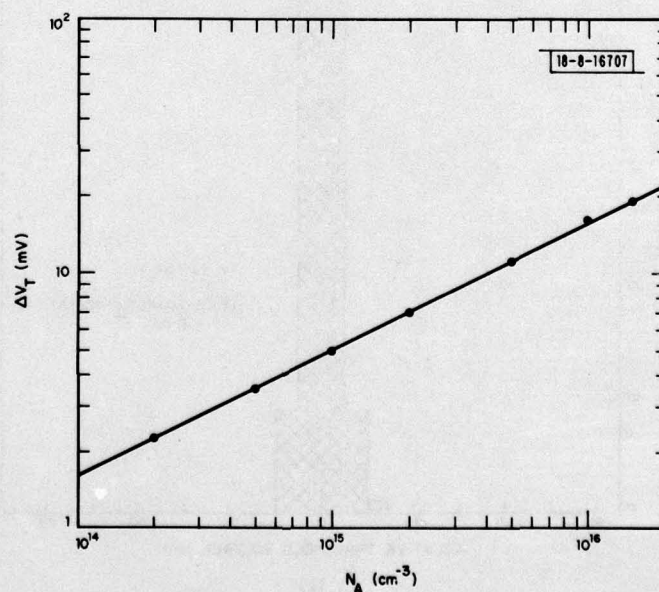
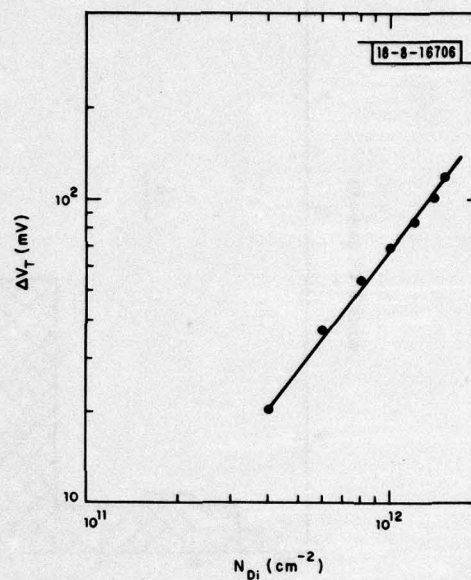
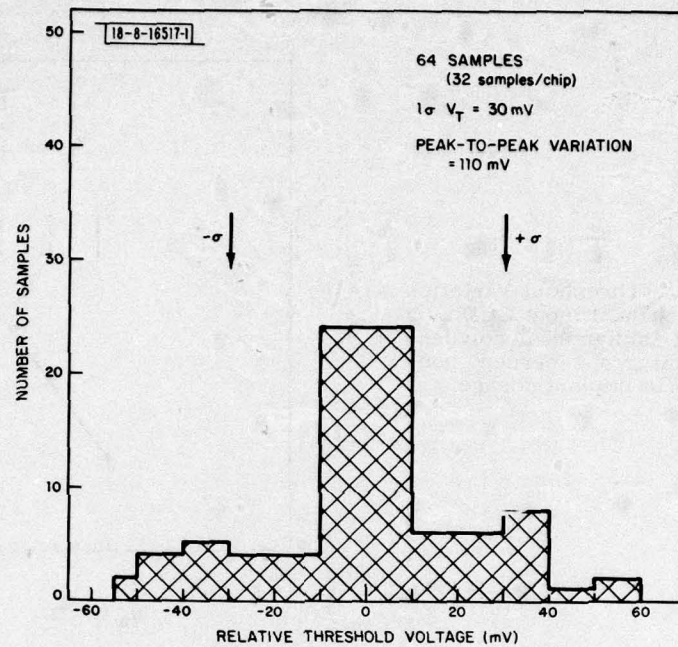
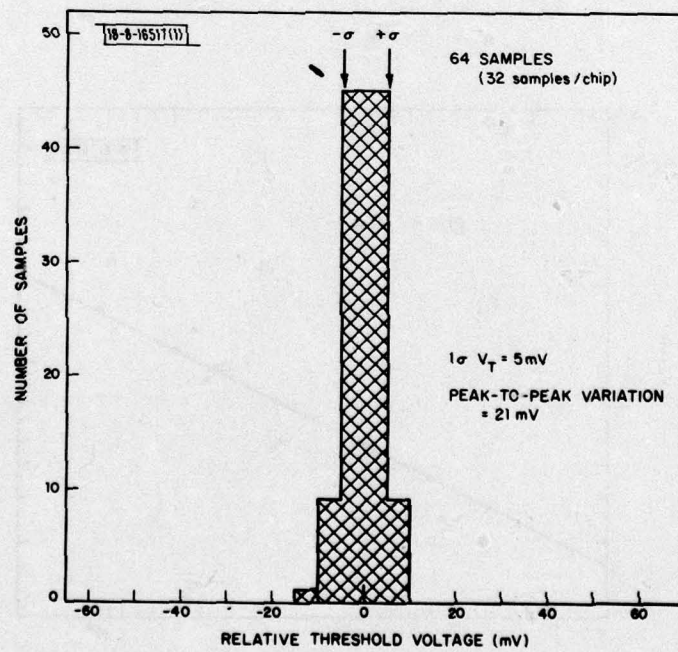


Fig. IV-12. Threshold variation of surface-channel input CCD as a function of substrate doping assuming a 1-percent non-uniformity in substrate doping.



(a)



(b)

Fig. IV-13. Distribution of threshold voltage for (a) BCCD and (b) SCCD.

devices with buried-channel inputs is plotted. A 1σ value of 30 mV and peak-to-peak variation of 110 mV has been achieved. In Fig. IV-13(b), the similar result for two devices with surface-channel inputs is plotted showing 1σ variation of 5 mV and peak-to-peak variation of 21 mV. All these data are consistent with the predictions of our model.

Based on Fig. IV-12, a surface-channel input CCD on a high-resistivity substrate material should further minimize the threshold variation. A new fabrication run without a boron offset implant at the input gate has been started, and the resulting devices will be used to determine if the threshold variation can be further reduced.

A. M. Chiang
B. E. Burke

E. MONOLITHIC GaAs FET AMPLIFIER

A monolithic millimeter-wave (34 GHz) transceiver module is currently under development. This module (illustrated in Fig. IV-14) will have in its receiver section a field-effect-transistor (FET) amplifier integrated with a balanced mixer. Here, we describe the fabrication and performance of a prototype monolithically integrated FET amplifier (shown in Fig. IV-15) which is fabricated on a 0.105×0.105 -in. chip. The distributed input matching network consists of a low impedance microstrip line cascaded with a 0.210-in.-long high-impedance line. The matching network is electroplated with gold to reduce the input series resistance.

The active device is fabricated on an epitaxially grown n-type layer. The ohmic contacts for the drain and source contacts are formed with a Au-Ge system. The contact resistance is typically 1 ohm/mm of source and drain width, and the contact resistance ranges from 2×10^{-6} to 3×10^{-6} ohm-cm². A detailed view of the gate area is shown in Fig. IV-16. The gate is formed by means of a lift-off process, and the dimensions are 1 by 500 μ m.

Figure IV-17 shows the drain characteristic of the FET measured on one-half of the gate length (250 μ m) by probing on one source pad only. The DC parameters of the full 500- μ m device are a transconductance g_m of 60 mmho, a saturated source-to-drain current I_{dss} of 50 mA, and a pinch-off voltage V_p of 1.3 V.

Figure IV-18 illustrates the gain of the amplifier vs frequency. The gain is in excess of 10 dB from 2 to 2.6 GHz without matching at the output of the amplifier, and the output mismatch loss is estimated to be 2.4 dB. With output matching, the amplifier has a noise figure of 4 dB with an associated gain of 11 dB at 2.5 GHz. By inserting an external tuner the input noise match is improved, and a minimum noise figure of 3 dB is obtained.

The next step in the fabrication of the monolithic transceiver is the integration of this FET amplifier with a balanced mixer. High-performance balanced-mixer circuits have been fabricated in monolithic form,¹⁰ and we recently fabricated discrete FETs and discrete mixer diodes on the same wafer using a process that successfully integrates the differing materials requirements of FETs (n on semi-insulating GaAs) and mixer diodes (n on n⁺-GaAs). Current efforts are aimed at extending this latter work to achieve a monolithic receiver.

In summary, we have fabricated a prototype integrated GaAs FET amplifier with gain in excess of 10 dB over a 0.6-GHz bandwidth. The noise figure of 4 dB at 2.5 GHz is attributed partly to noise mismatch at the input and partly to losses in the input matching network. Future versions of the amplifier will be designed with a better noise match, and these improved amplifiers will be integrated into a monolithic receiver.

A. Chu
W. E. Courtney
(Group 33)

G. A. Lincoln
L. J. Mahoney

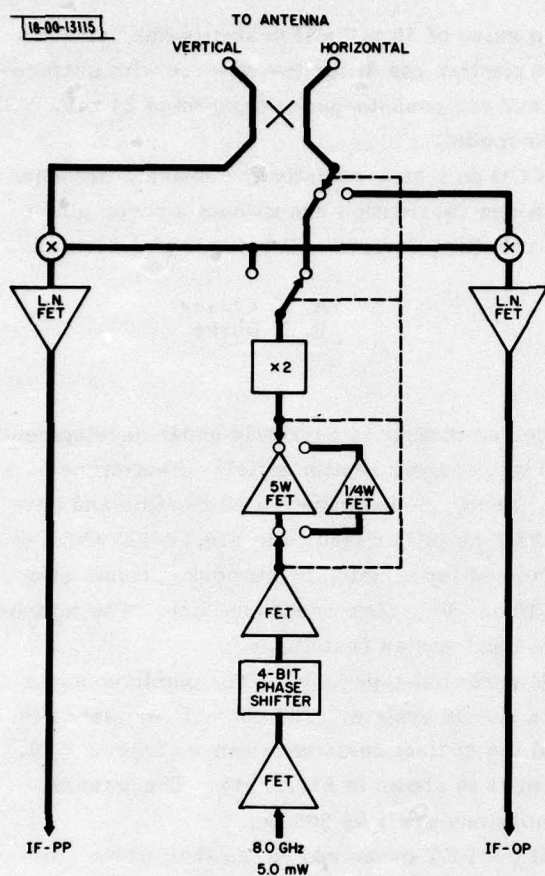
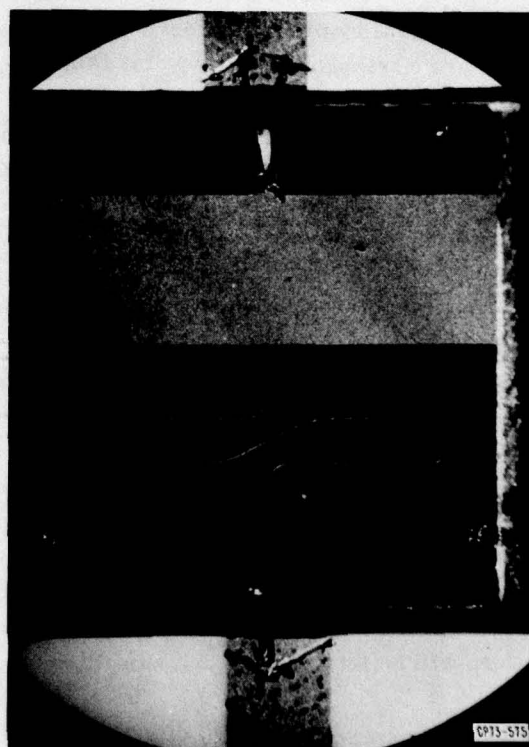


Fig. IV-14. Millimeter-wave transceiver design.

Fig. IV-15. Monolithic GaAs FET amplifier showing input (top), matching (center), and FET (bottom).



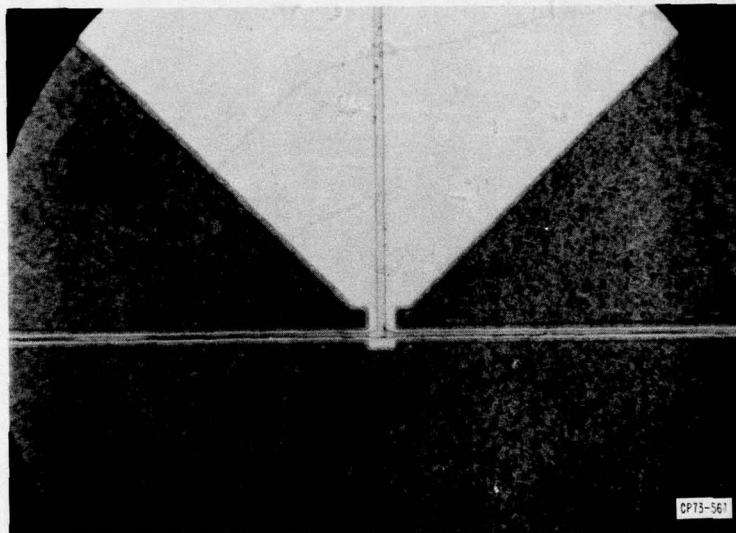


Fig. IV-16. Details of gate area of FET shown in Fig. IV-15. Source pads are top left and right, gate is shown in center, and drain pad is on bottom.

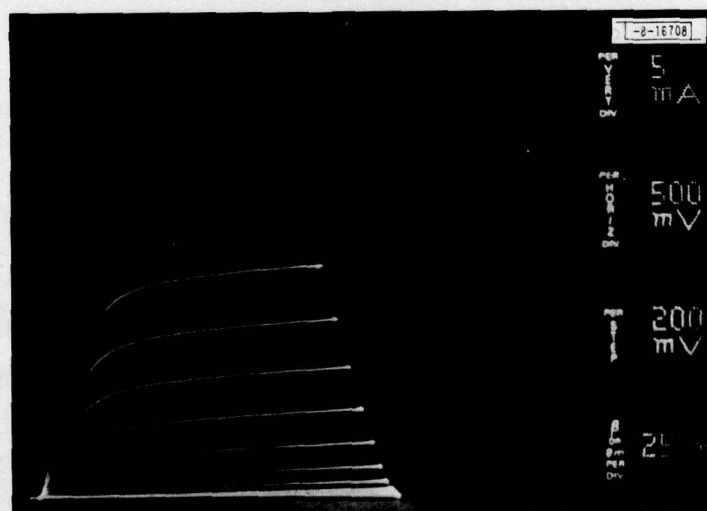


Fig. IV-17. Drain characteristics of one-half FET (250 μm of gate length) using one source pad shown in Fig. IV-16.

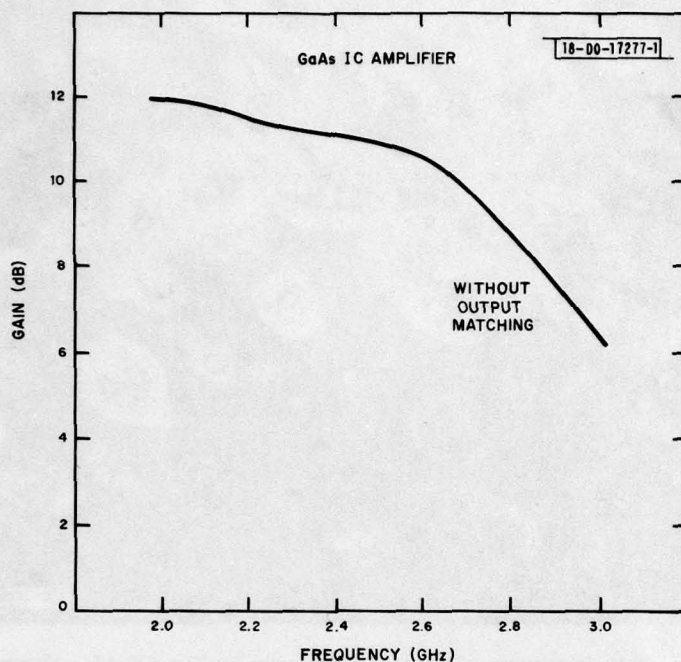


Fig. IV-18. FET amplifier gain vs frequency.

REFERENCES

1. C. O. Bozler, G. D. Alley, R. A. Murphy, D. C. Flanders, and W. T. Lindley, Seventh Biennial Cornell Electrical Engineering Conf., Ithaca, New York, 14-16 August 1979.
2. D. C. Flanders and H. I. Smith, J. Vac. Sci. Technol. **15**, 1001 (1978), DDC AD-A061211/9.
3. D. C. Flanders and H. I. Smith, J. Vac. Sci. Technol. **15**, 995 (1978), DDC AD-A061201/0.
4. D. C. Flanders, "Orientation of Crystalline Overlayers on Amorphous Substrates by Artificially Produced Surface Relief Structures," PhD. Thesis, Department of Electrical Engineering and Computer Science, M.I.T., 20 January 1978; reprinted as Technical Report 533, Lincoln Laboratory, M.I.T. (5 December 1978), DDC AD-A071168.
5. Solid State Research Report, Lincoln Laboratory, M.I.T. (1978:4), pp. 38-41, DDC AD-A068563/6.
6. *Ibid.* (1977:4), pp. 38-43, DDC AD-A052463/7.
7. S. N. Sze, Physics of Semiconductor Devices (Wiley, New York, 1969), pp. 24, 27, and 103.
8. Solid State Research Report, Lincoln Laboratory, M.I.T. (1979:2), pp. 51-54, DDC AD-A078676.
9. B. E. Burke and W. T. Lindley, Electron. Lett. **13**, 521 (1977), DDC AD-A054405/6.
10. R. W. Laton, W. E. Courtney, R. A. Murphy, C. O. Bozler, H. J. Stalzer, and G. B. Jones, "1978 Government Microcircuit Applications Conference Digest of Papers," J. Morreale, Ed., Monterey, California, 14-16 November 1978, p. 413.

V. ANALOG DEVICE TECHNOLOGY

A. A NEW CUT OF QUARTZ FOR A TEMPERATURE-COMPENSATED RAC

Surface-acoustic-wave (SAW) devices in the reflective-array-compressor (RAC) configuration¹ are usually fabricated on LiNbO_3 , which is known to be very temperature-sensitive. A temperature-stable RAC imposes the unique requirement of zero temperature coefficient of delay (TCD) in two perpendicular directions.² The search for an appropriate substrate material and cut focused on quartz, because there are several known temperature-compensated propagation directions.³ Specifically, the family of rotated Y cuts was examined in order to find an appropriate cut and propagation direction.

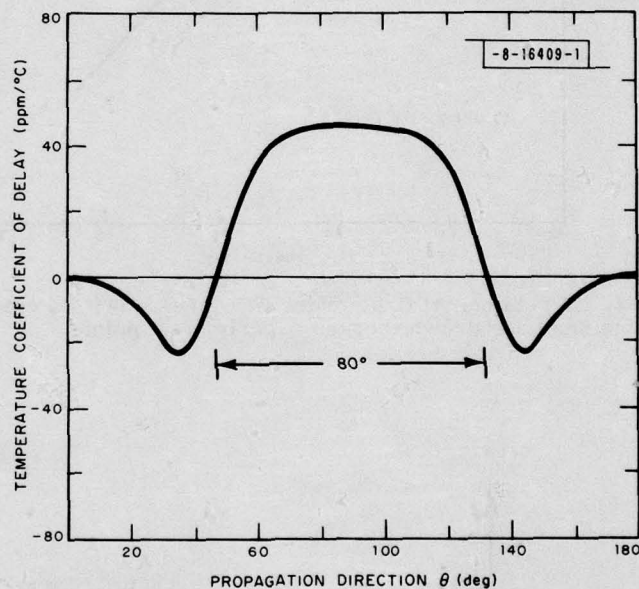


Fig.V-1. Calculated TCD of ST quartz vs propagation direction relative to X-axis.⁴ Angle between directions with zero TCD is indicated.

Theoretical calculations of the first-order TCD for rotated Y cuts of quartz^{3,4} were examined to determine the possible existence of an appropriate cut. The general shape of the curve for ST quartz shown in Fig.V-1 is typical of the results for the other rotated Y cuts. These curves have two significant features in common: (1) All are symmetric about the X-axis, and (2) the TCD passes through zero when the SAW propagation direction θ is near $\pm 45^\circ$ to the X-axis. In Y-cut quartz, θ for zero TCD is less than 45° ; in ST quartz, θ for zero TCD is greater than 45° . Since the angle between propagation directions with zero TCD is a monotonic function of cut angle, it becomes apparent that there exists a rotated Y-cut of quartz which has two temperature-compensated propagation directions which are orthogonal to each other. Because of the uncertainties in the values of the material constants which are used in the calculations, the exact value of the rotation angle of the new cut must be determined by experiment.

In order to find the exact cut angle, the TCD was measured on a series of rotated Y-cut quartz substrates. On each substrate, delay lines were fabricated with propagation direction

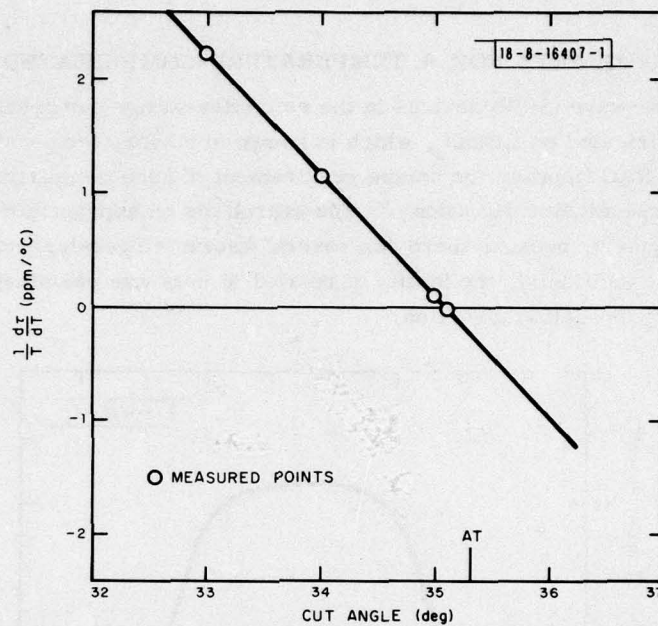


Fig. V-2. Experimental first-order TCD at $\theta = \pm 45^\circ$ vs cut angle. Solid line has been drawn through experimental points.

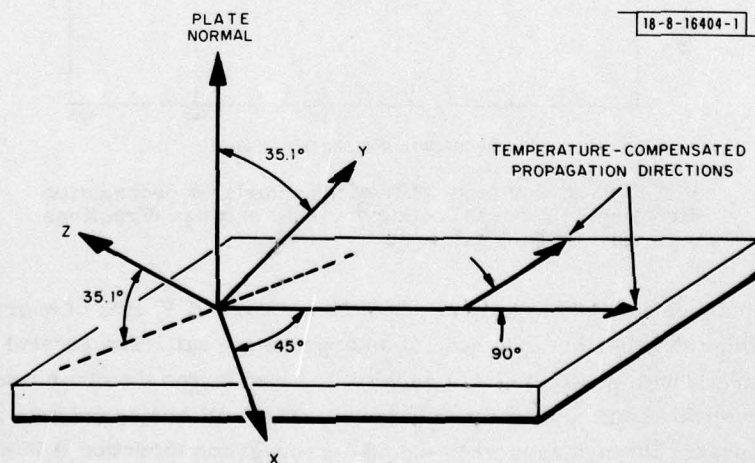


Fig. V-3. Angles for new cut of quartz.

at $\Theta = \pm 45^\circ$. The TCD was measured by the constant-phase-shift method. At a given reference temperature T_0 , the frequency of the surface wave propagating in the delay line was adjusted until the output phase of the delay line was equal to a constant reference phase ϕ_0 . When the temperature was changed, the frequency was adjusted so that $\phi(T)$ is again equal to ϕ_0 . Then,

$$\frac{\Delta f(T)}{f_0} = \frac{-\Delta \tau(T)}{\tau_0}$$

where $\Delta \tau/\tau_0$ is the fractional change in delay. Δf was measured for a series of temperatures and the data were fit to a quadratic curve. This procedure yields the first- and second-order TCD.

Figure V-2 plots the measured first-order TCD at $\Theta = \pm 45^\circ$ vs cut-rotation angle for four rotated Y-cut crystals. A straight line has been drawn through the data. As Fig. V-2 indicates, the 35.1° -rotated Y cut possesses zero first-order TCD at $\Theta = \pm 45^\circ$ referred to $T_0 = 22^\circ\text{C}$. The identified cut is diagrammed in Fig. V-3.

This cut and propagation direction does exhibit a small amount of beam steering. The power-flow angle was measured in the 35.0° -rotated cut. A laser surface probe was used to measure a power-flow angle of $3.4^\circ \pm 0.1^\circ$.

The second-order TCD is also of importance since its value determines the temperature range over which a device may be operated for a given change in delay. The measured second-order TCD of the new cut is smaller than the second-order TCD of ST-X quartz⁵ by about a factor of two, $1.5 \times 10^{-8}/(^{\circ}\text{C})^2$ compared with $3.2 \times 10^{-8}/(^{\circ}\text{C})^2$. This means that the new cut has greater stability than ST quartz.

Table V-1 summarizes the properties of the 35.1° -rotated cut. The properties of ST-X quartz are included for comparison. The two values of first- and second-order TCD correspond to the major and perpendicular directions of propagation, respectively.

D. E. Oates

TABLE V-1 COMPARISON OF ST-X AND 35.1° ROTATED CUTS		
	ST-X	35.1° Rotated Cut
First-Order TCD	0	0
	$47 \times 10^{-6}/^{\circ}\text{C}$	0
Second-Order TCD	$3.2 \times 10^{-8}/(^{\circ}\text{C})^2$	$1.5 \times 10^{-8}/(^{\circ}\text{C})^2$
	$7.3 \times 10^{-8}/(^{\circ}\text{C})^2$	$1.5 \times 10^{-8}/(^{\circ}\text{C})^2$
Beam-Steering Angle	0	3.4°
$\Delta v/v$	0.58×10^{-3}	0.51×10^{-3} (calculated ⁶)
Orientation Type	Singly rotated cut	Singly rotated cut

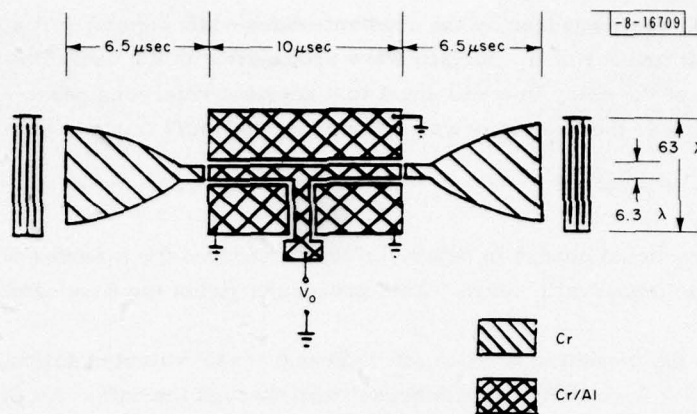


Fig.V-4. Parabolic-horn elastic convolver structure.

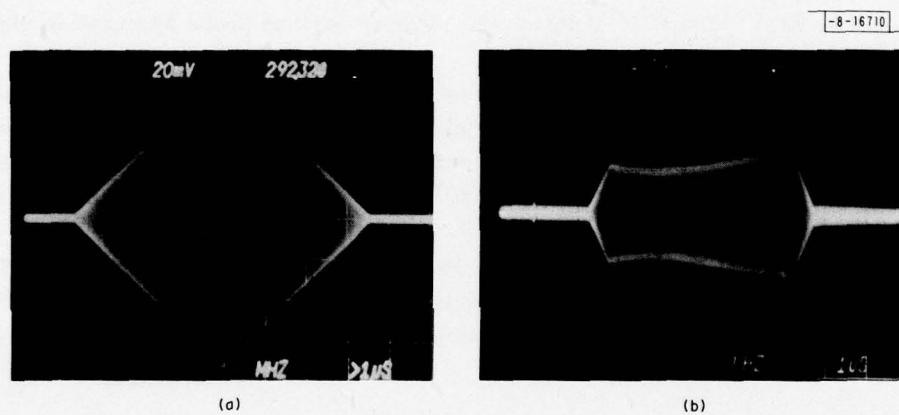


Fig.V-5. Tests of convolver operation. (a) Convolved output for 10-μsec input pulses; (b) uniformity scan obtained by convolving 1-μsec pulse with a 10-μsec pulse.

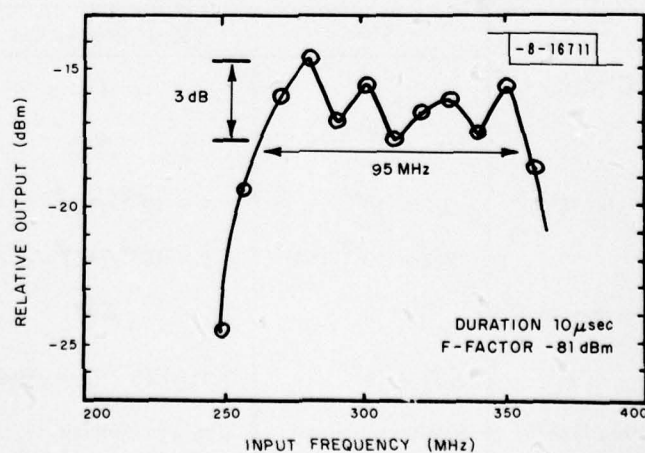


Fig.V-6. Frequency response of parabolic-horn elastic convolver.

B. WIDEBAND LiNbO_3 ELASTIC CONVOLVER WITH PARABOLIC HORNS

Recently there has been an interest in developing SAW convolvers which are less expensive to produce than gap-coupled convolvers. The elastic convolver which directly utilizes the acoustic nonlinearities of piezoelectric materials, like lithium niobate, satisfies this requirement. Work on elastic convolvers using multistrip beamwidth compressors (BWCs) to enhance the convolver efficiency has been reported.⁶ However, the fabrication tolerances on the multistrip BWC become quite stringent as the center frequency of the device is increased in order to achieve larger bandwidths. Parabolically tapered horns are an excellent replacement for the multistrip BWC. Such horns have been used in integrated optical devices to couple light from planar thin-film optical waveguides (one-dimensional confinement) to channel waveguides where the light is confined in two dimensions.⁷ This same method can be used to transform from a convenient, easily matched large-aperture SAW transducer to a narrower acoustic-channel guide, resulting in an increased power density and thus increasing the efficiency of an elastic convolver.⁸

The design goals for an elastic convolver were a 10- μsec interaction length, a 100-MHz bandwidth, and a dynamic range of 50 dB with +22-dBm inputs. The dynamic range and maximum input power determine the bilinear efficiency that must be achieved. The wideband transducer and matching networks are the same as those used for the 100-MHz-bandwidth Lincoln Laboratory gap-coupled acoustoelectric convolvers.⁹ The convolver demonstrated is shown in Fig. V-4. A parabolic-horn taper was chosen because it allows adiabatic transition in the shortest possible length. One can argue by ray tracing that the taper slope must be gentlest at the widest part of the horn, and steepest at the narrowest part of the horn. The horns are designed to compress by 10:1 the acoustic energy generated by a $63\text{-}\lambda$ -wide transducer at a 300-MHz center frequency. The 6.5- μsec -long tapered horns are formed with a layer of chrome only 200 Å thick in order to minimize mass loading. The coplanar arrangement of ground plates and output plate shown in Fig. V-4 was chosen because then only one side of the crystal needs to be metallized. The output plate which also forms the acoustic-channel guide is formed with 200 Å of Cr and 2000 Å of Al, as are the ground planes on each side of the plate. The convolver output is tapped at the center of the interaction region.

The convolver has been tested using both CW tones and a wideband pseudonoise (PN) sequence. Insertion-loss measurements were made with the horns and acoustic-channel guide in place, and were compared with the equivalent bare delay line. The horns and acoustic-channel guide appear to add about 3 dB to the 22-dB insertion loss of the bare delay line. Figure V-5(a) shows the convolver output for two 10- μsec tones. Note that the triangular sides are very linear and that there is no sign of compression at the peaks, thus indicating good uniformity. A scan of the interaction uniformity was produced by convolving a 10- μsec pulse with a 1- μsec pulse. Currently, there is a 2.5-dB variation over the convolver length, as shown in Fig. V-5(b). To measure device bandwidth, the frequency of the 10- μsec -long tones was scanned and a trace made of the convolver output. As shown in Fig. V-6, the convolved output remained within 3 dB of the peak output over a 95-MHz input bandwidth. The F-factor at center band was found to be -81 dBm. With +22-dBm inputs, an output 50 dB greater than the thermal-noise floor was achieved.

In order to more accurately assess the wideband performance of the convolver, a 93-Mchip/sec PN sequence was used for the convolver signal and reference. The convolved output demonstrated a +25-dB difference between the correlation spike and the rms value of the code sidelobes, which is approximately as expected.

R.A. Becker
D.H. Hurlburt

REFERENCES

1. R.C. Williamson, Proc. IEEE 64, 702 (1976), DDC AD-A028461/2.
2. D.E. Oates and R.C. Williamson, in 1979 Ultrasonics Symposium Proceedings (in press).
3. M.B. Schulz, B.J. Matsinger, and M.G. Holland, J. Appl. Phys. 41, 2755 (1970).
4. A.J. Slobodnik, Report No. AFCRL-72-0082, Air Force Cambridge Research Laboratories, Hanscom AFB, Massachusetts (1972).
5. J.F. Dias, H.E. Karrer, J.A. Kusters, J.H. Matsinger, and M.B. Schulz, IEEE Trans. Sonics Ultrason. SU-22, 46 (1975).
6. Ph. Defranould and C. Maerfeld, in 1972 Ultrasonics Symposium Proceedings (IEEE, New York, 1972), pp.224-227.
7. W.K. Burns, A.F. Milton, and A.B. Lee, Appl. Phys. Lett. 30, 28 (1977).
8. P.E. Lagasse, I.M. Mason, and E.A. Ash, IEEE Trans. Microwave Theory Tech. MTT-21, 225 (1973).
9. S.A. Reible, K.L. Wang, and V.S. Dolat, in 1978 Ultrasonics Symposium Proceedings (IEEE, New York, 1978), pp.48-53, DDC AD-A069929/8.

UNCLASSIFIED

SECURITY CLASSIFICATION OF THIS PAGE (When Data Entered)

19 REPORT DOCUMENTATION PAGE		READ INSTRUCTIONS BEFORE COMPLETING FORM
1. REPORT NUMBER 18 ESD TR-79-274	2. GOVT ACCESSION NO. AD A084271	3. RECIPIENT'S CATALOG NUMBER
4. TITLE (and Subtitle) 6 Solid State Research, 1979:4.		5. TYPE OF REPORT & PERIOD COVERED 9 Quarterly Technical Summary 1 Aug - 31 Oct 1979, rept.
7. AUTHOR(s) 10 Alan L. McWhorter		6. PERFORMING ORG. REPORT NUMBER 1979:4
9. PERFORMING ORGANIZATION NAME AND ADDRESS Lincoln Laboratory, M.I.T. P.O. Box 73 Lexington, MA 02173		8. CONTRACT OR GRANT NUMBER(s) 15 F19628-84-C-0002
11. CONTROLLING OFFICE NAME AND ADDRESS Air Force Systems Command, USAF Andrews AFB Washington, DC 20331		10. PROGRAM ELEMENT, PROJECT, TASK AREA & WORK UNIT NUMBERS Program Element No. 65705F Project No. 649L
14. MONITORING AGENCY NAME & ADDRESS (if different from Controlling Office) Electronic Systems Division Hanscom AFB Bedford, MA 01731		12. REPORT DATE 11 15 Nov 1979
16. DISTRIBUTION STATEMENT (of this Report) Approved for public release; distribution unlimited. 16 649L		13. NUMBER OF PAGES 94
17. DISTRIBUTION STATEMENT (of the abstract entered in Block 20, if different from Report) 12 92		15. SECURITY CLASS. (of this report) Unclassified
18. SUPPLEMENTARY NOTES None		15a. DECLASSIFICATION DOWNGRADING SCHEDULE
19. KEY WORDS (Continue on reverse side if necessary and identify by block number)		
solid state devices	photodiode devices	infrared imaging
quantum electronics	lasers	surface-wave transducers
materials research	laser spectroscopy	charge-coupled devices
microelectronics	imaging arrays	acoustoelectric devices
analog device technology	signal processing	
20. ABSTRACT (Continue on reverse side if necessary and identify by block number)		
<p>This report covers in detail the solid state research work of the Solid State Division at Lincoln Laboratory for the period 1 August through 31 October 1979. The topics covered are Solid State Device Research, Quantum Electronics, Materials Research, Microelectronics, and Analog Device Technology. Funding is primarily provided by the Air Force, with additional support provided by the Army, DARPA, Navy, NASA, NSF, and DOE.</p> <p>207650 <i>gmr</i></p>		

DD FORM 1473
1 JAN 73

EDITION OF 1 NOV 65 IS OBSOLETE

UNCLASSIFIED

SECURITY CLASSIFICATION OF THIS PAGE (When Data Entered)